SUPERCRITICAL FLOW IN COLLAPSIBLE TUBES

by

Michael E. McClurken

B.S., Drexel Institute of Technology
(1973)

S.M., Massachusetts Institute of Technology
(1976)

SUBMITTED IN PARTIAL FULFILLMENT
OF THE REQUIREMENTS FOR THE
DEGREE OF

DOCTOR OF PHILOSOPHY

at the

MASSACHUSETTS INSTITUTE OF TECHNOLOGY

February 1980

Signature of Author _____

Department of Mechanical Engineering
January 18, 1980

Certified by _____

Ascher H. Shapiro
Thesis Supervisor

Accepted by _____

Warren M. Rohsenow
Chairman, Departmental Graduate Committee

SUPERCRITICAL FLOW IN COLLAPSIBLE TUBES

by

Michael E. McClurken

Submitted to the Department of Mechanical Engineering
on January 18, 1980 in partial fulfillment of the
requirements for the Degree of Doctor of Philosophy.

ABSTRACT

When a thin-walled, compliant tube is partially collapsed due to a negative transmural pressure, the mechanics of the flow are closely coupled to the highly nonlinear structural mechanics of the tube. In many instances, it is not unusual for the mean fluid speed to exceed the phase velocity of long-wavelength, small-amplitude area waves, resulting in supercritical flow. Such flows are of broad interest in human physiology and with respect to certain medical devices.

A combined theoretical and experimental study was directed toward an improved fundamental understanding of supercritical flow phenomena, specifically: (i) standing waves of area that occur by reason of stiffness due to axial tension; and (ii) stationary shock-like transitions from subcritical to supercritical flow. An approximate theory of one-dimensional unsteady flow was developed that included the effects of fluid friction, axial tension and bending, a local tube law, and variations in elevation.

Theoretical results for wave dispersion and decay were obtained and shown to be in good agreement with experimental results. Shock-like transitions were successfully characterized both as diffusers, and as large-amplitude truncated waves.

Thesis Supervisor: Ascher H. Shapiro
Title: Institute Professor

ACKNOWLEDGEMENTS

There were many individuals whose knowledge, patience and understanding made this thesis possible.

Professor Ascher Shapiro, through his advice and assistance, has given me a new perspective on engineering research. Through his patient guidance I have learned to apply fundamentals with more confidence and determination, without losing the ability to exploit the obvious. I am also indebted to Professor Roger Kamm, whose Ph.D. research helped to provide a firm basis for my work. Roger's unswerving willingness to give his time and energy is deeply appreciated.

No acknowledgement for a thesis coming out of the Fluid Mechanics Laboratory would be complete without thanking our resident engineer-historian-technician-photographer -- Dick Fenner. Dick provided me with invaluable assistance in the design and construction of the apparatus, as well as helping to make the lab an enjoyable and interesting place to work. I am grateful to Marj Joss for her humor and her perserverence in typing one more collapsible-tube thesis.

Finally, I am indebted to the NIGMS Training Grant Program in Biomedical Engineering (Grant No. GM-02136), the NPSA Grant Program (Grant No. GM-07301-05), the National Heart, Lung and Blood Institute (HEW Grant No. HL17974) and the Fluid Mechanics Program of the National Science Foundation (Grant No. ENG76-08924) all of which provided financial support.

NOMENCLATURE

Symbol	Meaning
A	Cross-sectional area.
A_0	Cross-sectional area at zero transmural pressure.
A_c	Cross-sectional area of calibration section.
A_ℓ	Unoccluded cross-sectional area of the collapsible tube, sensed across a distance ℓ.
A_p	Cross-sectional area of the catheter
c	Phase velocity of finite wavelength area waves, Eq. (39).
c_∞	Phase velocity of infinite wavelength area waves, Eq. (1).
c_g	Group velocity, defined by Eq. (40).
c_t	Phase velocity due to axial tension.
c_b	Phase velocity due to axial bending.
C_p	Pressure recovery coefficient, Eq. (8).
C_{p_c}	Carnot pressure recovery coefficient, Eq. (14).
C_{p_o}	Oates pressure recovery coefficient, Eq. (15).
D_0	Inside diameter of tube at zero transmural pressure.
D_e	Hydraulic diameter, Eq. (48).
E	Young's modulus.
f	Skin friction coefficient, $f \equiv \tau_w / \frac{1}{2}\rho\bar{u}^2$
h	Tube wall thickness.
h_0	Tube wall thickness at zero transmural pressure.
i	$\sqrt{-1}$
K_p	Circumferential bending stiffness coefficient.
K_E	Extensional stiffness coefficient.

Symbol	Meaning
K_L	Loss coefficient, Eq. (9).
k	Complex wave number, $k = k_r + ik_i$
k_0	Inviscid real wave number, $k_0 \equiv \frac{2\pi}{\lambda}\Big\|_{f=0}$.
k_r	Real part of complex wave number.
k_i	Imaginary part of complex wave number.
L	Tube axial length after pre-strain, also length.
L_0	Initial tube length, unstrained.
ℓ	Separation distance of sensing electrode pair on catheter.
m	Dimensionless constant, Eq. (36).
p	Internal pressure.
p_e, p_{ext}	External pressure.
$\underline{P}$	Tube perimeter.
Q	Flow rate.
R	Resistance of a cylindrical conductor, $R = \left(\frac{\rho L}{A}\right)$.
R_0	Radius of collapsible tube at zero transmural pressure, $R_0 = D_0/2$.
R_e	Reynolds number, $R_e = \left(\frac{uD_e}{\nu}\right)$.
r	Dimensionless constant, Eq. (59).
S	Speed index, $S \equiv u/c_\infty$.
S_0	Inlet speed index, at beginning of standing waves.
S_1	Shock inlet speed index.
T	Axial tension per unit perimeter, $T = \varepsilon_x Eh$.
t	Time.
u	Mean fluid velocity in axial direction.

Symbol	Meaning
u_0	Mean fluid velocity through neutral area, $u_0 = (Q/A_0)$.
ΔV_ℓ	Voltage drop across catheter electrode pair.
ΔV_c	Voltage drop across calibration electrode pair.
x	Axial distance.
z	Tube elevation.

Greek

α	Area ratio, $\alpha \equiv A/A_0$.
α_0	Area ratio at inlet to standing waves.
α_1	Shock inlet area ratio.
β	Ratio of extensional stiffness to bending stiffness, $\beta \equiv K_E/K_p$.
$\hat{\hat{\alpha}}$	Local maximum amplitude of area wave, Eq. (65).
$\hat{\alpha}$	Local amplitude of area wave, Eq. (64).
ε_x	Axial strain, $\varepsilon_x = (L-L_0)/L_0$.
ν	Kinematic viscosity.
ρ	Fluid density; also electrical resistivity.
τ_w	Wall shear stress.
M	Property defined by Eq. (2).
η	Tube wall displacement defined by Eq. (18), Fig. 18
ϕ	Phase angle, (see Eq. (36)).
λ	Wavelength
θ	Angle of tilting table with the horizontal, see Fig. 3.
ξ	Non-dimensional distance, $\xi \equiv x/D_0$.
P	Non-dimensional transmural pressure, $P \equiv (p-p_e)/K_p$.

Subscripts	Meaning
$( )_{tr}$	Transmural, across the tube wall
$( )_{exp}$	Experimental
$( )_0$	Initial, just downstream of the sphincter

Superscripts	
$\bar{( )}$	Spatial mean
$( )'$	Spatial perturbation

TABLE OF CONTENTS

	Page
Abstract	2
Acknowledgements	3
Nomenclature	4
CHAPTER I. INTRODUCTION	11
Significance of the Problem	11
Previous Work	12
Organization of the Thesis	15
CHAPTER II. EXPERIMENTAL APPARATUS	17
Flow Circuit	17
Tube Mounting	17
Area Measurement by an Electrical Impedance Technique	18
Pressure Measurement	22
CHAPTER III. EXPERIMENTAL RESULTS	24
The Local Tube Law	24
Steady Supercritical Inlet Flows	29
Shock Wave Structures	34
CHAPTER IV. THEORY: EFFECTS DUE TO AXIAL TENSION AND BENDING	39
Flow Equations: Basic Assumptions	39
The Tube Model	40
The Tube Law	42
Axial Tension	43
Axial Bending	45
Governing Equations	47
Methods of Solution	48

Page

CHAPTER V. LINEAR ANALYSIS OF THE GOVERNING EQUATIONS 50

Linearization of the Governing Equations 50
Small Amplitude Travelling Waves 51
The Inviscid Dispersion Relation 53
Group Velocity 53
The Radiation Condition 54
Relative Importance of Axial Bending 54
Comparison with Experiments 56

CHAPTER VI. DECAY OF STANDING WAVES IN A STEADY FLOW 58

Consequences of a Constant Skin Friction Coefficient 58
Consequences of a Spatially Oscillatory Skin Friction Coefficient 65
Shock Scaling 70

CHAPTER VII. NUMERICAL INTEGRATIONS 75

Purpose 75
Governing Equations 75
Numerical Technique 77
Results of Forward Integrations - Waves 78
Backwards Integrations: Shock-like Transitions 81

CHAPTER VIII. SUMMARY AND CONCLUSIONS 83

Experimental 83
Theoretical 84
Linear Analysis - Inviscid 85
Linear Analysis - Viscous 86
Shock-like Transitions 89
Numerical Integrations 90
Conclusions 91

Page

REFERENCES 94

TABLES 98

LIST OF FIGURES 105

APPENDIX A. COMPUTER PROGRAM FOR NUMERICAL CALCULATIONS 149

CHAPTER I:

INTRODUCTION

Thin-walled, compliant tubes become partially collapsed when subjected to a negative transmural (internal minus external) pressure. If the collapse is uniform along the tube axis, the mechanism of collapse is dominated by circumferential bending stiffness rather than the hoop stresses that are dominant when a tube is inflated by a positive transmural pressure. In the region of partial collapse, before opposite walls come into contact, small changes in pressure result in large changes in area. Thus, the phase velocity of long wavelength, small-amplitude waves is much lower for a given tube if it is partially collapsed rather than inflated by a positive transmural pressure. As a consequence, supercritical flow is quite common for such tubes. "Supercritical" here signifies that the mean flow velocity exceeds the phase velocity of long waves.

The thesis deals for the most part with steady, supercritical flows. The thrust is toward two somewhat related topics: (i) standing waves of area that occur by reason of stiffness due to axial tension; and (ii) shock-like transitions from supercritical flow to subcritical flow.

Significance of the Problem. Flows in collapsible tubes are of interest mainly in physiology and with respect to certain medical devices. Shapiro[1] has performed an extensive review. Only a brief summary of the areas of interest is presented below.

Physiologic applications are to be found (i) in the circulatory system, primarily on the venous side; (ii) in the pulmonary system in both

the airways and the pulmonary circulation; (iii) in the urethra; (iv) possibly in the Eustachian tubes and in the drainage of aqueous humour from the eye; (v) relatedly, in the functioning of the vocal cords; (vi) possibly in so-called "autoregulation" of the blood flow to systemic organs; and (vii) to a variety of sounds heard in the cardiovascular and pulmonary systems.

Some of the clinical devices involving flow in collapsible tubes are (i) the occlusive method of blood pressure measurement; (ii) pressurizing cuffs for diagnosing occlusive disease and thrombi in the extremities; (iii) intermittently-pressurized boots below the knee as prophylaxis against deep vein thrombosis in surgical patients; (iv) counterpulsation techniques (the intra-aortic balloon as well as boots on both legs up to the groin) under electrocardiogram control as temporary but relatively non-invasive means of cardiac assist; and (v) certain forms of externally-worn prosthetic larynxes.

Previous Work. Almost all previous efforts on flow in collapsible tubes have been based on the assumption that a unique relationship exists between local cross-sectional area and transmural pressure. Such a relationship, $A = A(p-p_e)$, will be referred to as a "local tube law", since it implies that the area is a single-valued function of the transmural pressure and vice versa. However, this assumption is correct only when structural stiffness due to axial tension and bending is insignificant compared with the circumferential bending stiffness. This is the case when axial variations in area are of sufficiently long wavelength. Thus, the assumption of a "local tube law" is equivalent to the assumption of infinite wavelength in area variations.

For wave propagation in compliant vessels containing fluid, Weber[2] determined the infinite wavelength phase velocity, c_∞, to be:

$$c_\infty^2 = \frac{A}{\rho}\frac{d(p-p_e)}{dA} = \frac{K_p\alpha}{\rho}\frac{dP}{d\alpha} \qquad (1)$$

where ρ is the fluid density; A_0 is the rest value of A at zero transmural pressure; $\alpha \equiv A/A_0$; K_p is the circumferential bending stiffness, $K_p = (1/12)E(h/R_0)^3/(1-\nu^2)$; E is Young's modulus; ν is Poisson's ratio; h is the wall thickness; R_0 is the rest radius; and $P \equiv (p-p_e)/K_p$. Here P and α are the appropriate dimensionless transmural pressure and area.

Griffiths[3,4,5,6], Oates[7], and Shapiro[1,8] have performed theoretical analyses of steady one-dimensional flows obeying a local tube law. Such flows are analogous to one-dimensional gas dynamic and free-surface flows with $P(\alpha)$ playing the role of the equation of state in gas dynamics. The speed index, $S \equiv u/c_\infty$, where u = mean fluid speed, is analogous to the Mach number and the Froude number. The work of the above mentioned investigators has revealed that supercritical flows, $S > 1$, produce effects opposite in sign to those of subcritical flows, $S < 1$. For instance, when $S < 1$, friction causes the area and the pressure to decrease, while the opposite is so when $S > 1$. The sign of dS/dx depends not only upon the sign of (1-S), but also on whether the property of the local tube law defined by

$$M(\alpha) = 3 + \frac{\alpha\, d^2P/d\alpha^2}{dP/d\alpha} \qquad (2)$$

is positive (e.g., friction causes S to increase in subcritical flow) or negative (e.g., friction causes S to decrease in supercritical flow).

Olsen *et al.*[9], Oates[7], Shapiro[8], and Kamm *et al.*[10] have shown the possibility of shock waves forming due to nonlinear steepening of propagating finite-amplitude area waves. By several independent analyses it was shown that when $M(\alpha) > 0$, compression waves steepen, and when $M(\alpha) < 0$, rarefaction waves steepen.

Lambert[11], Beam[12], Rudinger[13], Anliker *et al.*[14], and Kivity *et al.*[15] have performed nonlinear analyses of unsteady flow in compliant tubes, revealing effects that suggest shock wave formation. These efforts were directed mainly toward inflated tubes (as in the arterial system) and thus do not involve the large area changes typical of shock-like structures when the tube is partially collapsed.

Griffiths[4] provided a photograph that clearly demonstrated a stationary shock-like transition with a large increase of area; upstream of the shock the tube was partially collapsed and the flow supercritical, downstream the tube was inflated. Oates[7] and Shapiro[1,8] have suggested overly simple analyses of such a shock.

The structure of stationary shocks was shown by Kececioglu *et al.*[16] to involve a train of stationary precursor waves ahead of the shock transition. Kececioglu[17] reported an extensive series of experiments and related theoretical calculations, showing that the precursor waves standing ahead of shock-like transitions are due to, and explainable by, the effects of axial tension. Experimental shock-like transitions from supercritical flow in a partially-collapsed tube were also described by Elliot *et al.*[18].

Flow in a compliant channel becomes unstable at high flow velocities, resulting in either collapse of flutter. To predict the stability limit for a partially collapsed compliant tube, investigators have modeled the unusual cross-sectional shape as a two-dimensional channel with compliant walls (Weaver and Paidoussis[19], Matsuzaki and Fung[20]) and as a bi-concave channel (Raman[21]). Their results exhibit instability limits and also wave speed dispersion caused by vessel stiffness to longitudinally non-uniform deformations. As a result of this dispersive character of waves in a compliant vessel, any steady flow with a speed greater than c_∞ may have standing waves superimposed upon a steady flow.

Organization of the Thesis. Since the phenomena that have been studied may be unfamiliar to most readers, the experimental aspects of the thesis are presented before discussing the development of related theories. In Chapter II the flow circuit and instrumentation techniques are described. A variety of experimental results are presented in uncorrelated form in Chapter III.

Chapter IV is devoted to the development of a theoretical model. In addition to the equations of continuity and momentum, an approximate constitutive relation for the tube structural mechanics is developed to account for effects due to axial tension and bending.

In Chapter V the governing equations are linearized for small perturbations in area, fluid velocity and skin friction coefficient about constant mean values, primarily to investigate wave propagation phenomena. The inviscid dispersion relation for travelling area waves of small amplitude and finite wavelength is obtained and compared with experimental results.

Viscous effects, as modelled by a skin friction coefficient composed of a mean quantity plus a perturbation, are introduced in Chapter VI. The consequences of both parts are investigated through their influence on both long wavelength, mean behavior and the decay of finite wavelength area waves. Solutions are derived from the linearized governing equations and compared with corresponding experimental results. In addition, the linearized theory is applied to shock-like transitions in order to gain some insight into the scaling of shock parameters.

Numerical integration of the full nonlinear governing equations is discussed in Chapter VII. Solutions are generated in the form of axial distributions of area ratio and other related parameters, largely to confirm the previous solutions to the linearized equations through small-amplitude numerical "experiments". The major findings of the thesis are summarized in Chapter VIII.

CHAPTER II:

EXPERIMENTAL APPARATUS

The goal of the experimental program was to measure cross-sectional area and internal pressure as a function of axial distance for a variety of steady flows with supercritical inlet conditions. An electrical impedance technique was developed to enable accurate shape-independent measurement of local tube cross-sectional area. By first determining the "local tube law" under no-flow conditions, it is possible to infer both mean fluid speed and speed index from the measurement of flow rate and area. The apparatus was designed to allow considerable variations in axial wall tension, inlet area ratio, and inlet speed index.

Flow Circuit. A schematic of the overall apparatus is shown in Figure 1. A tube of latex rubber (I.D. = 2.54 cm, wall thickness = 0.086 cm, length $\cong$ 110 cm) is typically mounted on two rigid cylindrical end supports that pass through the end caps of a flanged clear plexiglas test section (I.D. = 10.16 cm, length = 130 cm). A constant head tank provides the driving pressure for flow to the test section. A calibrated rotameter is used to measure the steady flow rate that can be adjusted by means of a metering valve. Discharge from the test section is through a valve, used to control shock position, to another constant head tank.

Tube Mounting. Figure 2 shows some further details of the test section. The latex tube is attached to rigid tubes tapered externally to a thin edge with O-rings. The rigid tubes (I.D. = 2.22 cm,

O.D. = 2.54 cm) are O-ring sealed in such manner as to allow for both twisting and axial adjustments. The twist is required to assure a uniform plane of collapse. The axial movement is necessary to apply varying degrees of axial strain to the mounted tube. Pre-strain is determined by measuring the change in distance between two lines drawn on the tube.

The test section can also be set up in a different manner, as shown in Figure 3. The tube is supported by a flat plate and the downstream end left free. Without the external liquid, a tilt of the test section at an angle θ yields an axial component of the gravitational body force per unit mass ($g \sin \theta$). As will be shown later, there are advantages to this configuration that arise both from the lack of a downstream rigid attachment and from the presence of gravitational force as a means of cancelling frictional effects.

A subcritical to supercritical transition is established by an adjustable sphincter (Figure 2, Section A-A) which collapses the tube symmetrically into its twin-lobed mode. The sphincter serves the same fucntion as a sluice gate in a free-surface flow or convergent-divergent nozzle in a gas-dynamic flow. The setting of the constriction also establishes the inlet area.

Area Measurement by an Electrical Impedance Technique.

In systems of rigid tubing, it is quite simple to determine the cross-sectional area at any section. Contrariwise, in order to perform the quantitative experiments reported here it was necessary to develop an instrumentation scheme capable of accurate shape-independent area measurement.

Principle. If the rate of change of area with respect to distance or time is sufficiently small, the resistance of a cylindrical conductor may be written as $R = \rho L/A$, where ρ is the resistivity of the medium in ohm-cm, L is the length of the conductor, and A is the cross-sectional area. The principle of area measurement by electrical impedance is based upon the use of a conductive salt solution as the fluid that flows in the collapsible tube. Since the impedance of high concentration salt solutions is primarily resistive, local cross-sectional area can be determined by measuring the electrical resistance of the internal fluid path over some small incremental axial distance.

As shown in Figure 4 three electrode pairs are used. The first pair provides an AC voltage excitation, and consequently a current flow, from an upstream electrode mounted on rigid tubing through the collapsible tube and downstream rigid tubing to ground. The second and third are sensing pairs direct coupled to high impedance, high CMRR differential amplifiers. A differential voltage ΔV_c is sensed across a calibration length L_c and area A_c. A differential voltage ΔV_ℓ is sensed by the electrode pair epoxy-bonded into a teflon cather across a length ℓ and the unknown area A_ℓ. If the conductivity of the external liquid is low enough relative to that of the salt solution inside and the latex tube itself, current leakage is small. The two sensing pairs then detect voltage drops across two resistors in series. Assuming that the current flux is quasi-one-dimentional in the collapsible tube, the unoccluded cross-sectional area A_ℓ can be expressed as:

$$A_\ell \cong \left(\frac{A_c \ell}{L_c}\right)\frac{\Delta V_c}{\Delta V_\ell} \qquad (3)$$

The actual cross-sectional area is obtained by adding to A_ℓ the area of the catheter $A_p \approx 0.054$ cm^2. Note that absolute calibration is obtained simply by moving the catheter electrode pair into one of the rigid tubes.

Instrumentation. An analog circuit was designed to implement Eq. (2) and provide a continuous output voltage proportional to the unoccluded area A_ℓ. As indicated in Figure 5, the two sensing electrode pairs are direct coupled to high quality differential amplifiers. Capacitive coupling at the input to reject DC electrode potentials is avoided to maintain a common mode rejection ratio (CMRR) of greater than 100 db. Instead, the DC offsets are amplified and rejected at the output. In order to provide DC signals that could be fed to the analog divider, the two AC signals are sampled and held once per cycle using synchronous pulses derived from the excitation voltage. The output of the divider is then directly proportional to the area A_ℓ, with the one constant of proportionality including the gains of the differential amplifiers as well as geometric constants.

Sources of Error. There are several aspects of the technique which, if not properly attended to, will result in unacceptably large errors. The most important of these arises from the non-ideal behavior of differential amplifiers. Since the voltage drop across the catheter electrode pair is often as low as several millivolts with a common mode voltage of up to 5 volts, the amplifier must have a high common mode rejection ratio (CMRR) of at least 100 db. If not, the voltage ΔV_ℓ will be substantially increased as some fraction of the common mode voltage appears at the output. Also, since CMRR decreases as frequency increases, the excitation frequency

must be kept as low as possible, typically around 200-500 Hz. Common mode errors are easily detected as falsely low area output when the probe is nearest the upstream excitation electrode.

In addition, if the external liquid is the same as the low resistivity salt solution, significant errors result midway between the rigid supports. Here, falsely high area output results from current leaking resistively through the latex tube and down the lower resistance external path. This situation was avoided by the use of a glycerine in water mixture density-matched to a 7% by weight solution of sodium chloride that was used as the internal liquid. The glycerine in water mixture had a specific gravity of approximately 1.050 with a resistivity of 7×10^4 ohm-cm; high enough relative to the resistivity of the salt solution (10 ohm-cm) to limit shunt leakage current to a tolerable level. Figure 6 gives a brief summary of the two main sources of error.

In order to verify that the technique is not unduly sensitive to large gradients in area or changes in shape, a converging-diverging section of 2.54 cm O.D. rigid plexiglas tubing was formed with a heat gun. The area determined by the impedance method agrees quite well with the area determined by a method based on the linear displacement of small volumetric excursions. As shown in Figure 7, the constriction produces a reduction in area to 38% of circular over a distance of approximately two diameters, and is appropriate for a steep shock. Another check on a rigid tube with a gradually tapering cylindrical insert verified that small changes in area on the order of 1% of the circular area can be easily resolved.

Pressure Measurement

No-Flow Conditions. When measuring pressure under no-flow conditions, as for a local tube law, simple single column manometers are used for the salt and glycerine solutions. The latex tube used for the experiments is highly compliant: collapse from a circular configuration to one with the opposite walls in contact occurs over a range in transmural pressure of less than 2 cm of water. Thus, heights of the liquid columns are read using a cathetometer with a resolution of ± 0.005 cm.

Steady Flow. The closed loop traversing catheter probe shown schematically in Figures 1 and 4 was used to measure both internal fluid pressure and cross-sectional area. The loop is formed by a length of hollow teflon tubing (I.D. = 0.180 cm, O.D. = 0.275 cm) and a section of fiber-reinforced plastic sprocket chain. A constant speed motor provides a stable drive for the loop. As shown in Figure 2, Section A-A, the cather is placed up against the wall of the rigid tube. This insures that when the tube is collapsed, interference by the catheter is delayed until an area ratio of about 0.15 is reached, well below line contact.

Internal pressure is sensed at a side tap hole in the catheter. Between the side tap and a physiologic pressure transducer mounted on a movable cart the teflon catheter is internally reinforced by stainless steel needle tubing. A Gould Statham P23 unbonded strain gauge type physiologic transducer coupled to the stainless steel needle tubing has a time constant less than 50 msec as determined by the bursting balloon test. This time response is adequate for a traversing speed of 5 cm/sec, but the full scale range of the transducer is too large to obtain

reasonably noise-free output. Signal to noise ratio is sacrificed for time response due to a lack of commercially available transducers with both low compliance and small full scale range (on the order of 10 cm of water). This situation is not serious since the area measurement provides the bulk of important data in steady flow.

CHAPTER III:

EXPERIMENTAL RESULTS

In this Chapter experimental results are described for both static (no-flow) and steady flow cases. Development of one-dimensional theories to explain these results will follow in Chapter IV.

The Local Tube Law

Experimental Technique. The pressure-area relationship for the latex tube is determined by mounting the tube under zero axial strain and measuring the cross-sectional area and transmural pressure as they change in response to slow volumetric withdrawals. Initially, the transmural pressure is maintained positive and the tube cross-section is circular. Repeated withdrawals of fluid cause the tube to collapse into a quasi-elliptical shape and eventually into a configuration of two-lobed collapse, with opposite walls in line contact. Throughout this procedure the catheter is positioned so that the sensing electrode pair is located midway between the rigid end supports. This insures that the cross-sectional area is measured at a point as far as possible from any end effects; in a region where axial area variations are very small.

The cross-sectional area at zero transmural pressure, A_0, is determined by interpolation of the raw pressure-area data. The experimentally obtained value, $A_0 = 4.985$ cm^2, is very close to the anticipated value for a tube with a nominal I.D. of 1.0 inch. All area data are normalized to this value: $\alpha \equiv A/A_0$. Transmural pressures are normalized to an

experimentally determined value for the bending stiffness coefficient, K_p. The manner in which K_p is measured is discussed in connection with the collapsed configuration of opposite walls in line contact.

Similarity Range. As collapse proceeds into the region of line contact the cross-sectional configurations assume self-similar shapes; that of two tear-shaped lobes. Flaherty *et al.*[22] performed an analysis of the post-buckling behavior of an initially circular thin-walled tube whose material is linearly elastic. For a tube that collapses under the constraint of constant perimeter they derived a relation that is valid for area ratios less than 0.21, the similarity range:

$$P = -0.995\ \alpha^{-3/2} \qquad (4)$$

Here $P \equiv (p-p_e)/K_p$, and K_p is the bending stiffness coefficient, $K_p = (1/12)E(h/R_0)^3/(1-\nu^2)$.

In theory, it should be possible to infer K_p from knowledge of the tube dimensions and the mechanical properties of latex. However, it is much more practical to determine it from a fit of the experimental data to the similarity law of Eq. (4) with the numerical constant assumed to be equal to 1.00. Experimental results for this range of area ratios are shown in Figure 8a on an expanded log-log plot of P versus α. For area ratios slightly greater than 0.21 touch contact has occurred but true line contact has not yet been established. Below an area ratio of 0.21 the data is well fit to Eq. (4) using a value for K_p of 304 dynes/cm^2. Below an area ratio of about 0.15 the tube becomes internally stiffened by the

onset of tube wall contact with the catheter that is positioned in one of the lobes.

Partial Collapse. A linear plot of P versus α is shown in Figure 8b, covering a range in area ratio of 0.15 to 1.0. The points of the P-α data are unsmoothed, indicating the practical resolution of the electrical impedance method for area measurement. The sharp change in slope at $\alpha \approx 0.27$ agrees very well with the prediction of Flaherty *et al.*[22] that initial point contact between opposite walls should occur at that area ratio. In the range of area ratios from 0.27 to 0.90 the P-α data indicates that the tube is highly compliant; i.e. small changes in P are accompanied by large changes in α.

The buckling pressure for an initially circular tube has been calculated by Tadsbakhsh and Odeh[23] to be $P_b = -3.0$. Examination of Figure 8b in the vicinity of $\alpha = 1.0$ reveals that this is a reasonable value. Note that the buckling here is a smooth, continuous transition and not a snap-through buckling phenomena.

The Inflated Tube. Using the kinetic theory of rubber elasticity, Treloar[24] derived an expression for a thin-walled circular tube inflated by a positive transmural pressure:

$$\Delta P_{tr} = K_E(1-\alpha^{-2}) \qquad (5a)$$

Here ΔP_{tr} is the transmural pressure, and K_E is the theoretical extensional stiffness of the tube, $K_E = Eh/[2R_0(1+\nu)]$. Figure 8c shows a linear plot of P versus $(1-\alpha^{-2})$ for $\alpha \geq 1.00$. As indicated by the dashed line in

Figure 8c the data is well fit to a semi-empirical expression similar to Eq. (5a):

$$P = \beta(1-\alpha^{-2}) - 6.0 \qquad (5b)$$

Here $\beta \equiv K_E/K_p$, the ratio of the tube's extensional stiffness to the tube's circumferential bending stiffness. From the slope of the dashed line in Figure 8c β is determined to be approximately equal to 870. The presence of the empirical constant -6.0 merely indicates that at $\alpha = 1.00$ the tube is not exactly circular.

In Figure 8c the range in area ratio represented is less than 0.120. The agreement with Eq. (5b) is remarkable considering the scale of the changes in area ratio. It is also important to note that the value of β indicates that the tube is nearly three orders of magnitude stiffer when inflated by a positive transmural pressure than when partially collapsed by a negative transmural pressure.

Derivation of $c_\infty(\alpha)$. From experimental P-α data it is possible to derive the infinite wavelength phase velocity c_∞ using Eq. (1). The P-α data was first smoothed graphically using a french curve. The smoothed data was then differentiated numerically using an algorithm that fits a fifth order polynomial to tabulated data. Differentiation noise was then graphically smoothed out. The resulting $c_\infty(\alpha)$ is shown as a solid line in Figure 8b. The localized maximum in c_∞ occurs in the region between touch contact ($\alpha \approx 0.27$) and true line contact ($\alpha \approx 0.21$). Note also that between the area ratios of 0.3 and 0.8 there is very little change in the value of c_∞, which remains at a level far below that corresponding to

either inflation or to opposite walls in contact. Table 1 presents the tabulated local tube law that is used for interpreting experimental results as well as for performing numerical simulations.

Effect of Axial Strain. The local tube law shown in Figure 8b was measured for the case of zero, or negligibly small axial strain. For the experimental results reported in this thesis, one tube is used, mounted under a range of axial strains. In order to use the zero strain local tube law two assumptions are made. First, it is assumed that the resting tube dimensions, h_0 and R_0, contract under axial strain in a linear manner. Secondly, it is assumed that the zero strain local tube law is still valid and that the effects of axial strain can be taken into account through changes in the normalizing parameters A_0 and K_p. The wall thickness at zero transmural pressure and axial strain ε_x is taken to be:

$$h_{0,\varepsilon_x} = (1-\nu\varepsilon_x)h_0 \tag{6}$$

where ν is Poisson's ratio (about 0.5 for latex) and h_0 is the wall thickness under zero transmural pressure and zero axial strain. Similarly the radius of the contracted circular tube at zero transmural pressure is taken to be:

$$R_{0,\varepsilon_x} = (1-\nu\,\varepsilon_x)R_0 \tag{7}$$

Since the ratio $(h_{0,\varepsilon_x}/R_{0,\varepsilon_x})$ remains constant for this approximation, no change in K_p is anticipated for small strains.

Effect of a Normal Hydrostatic Gradient. When the test section is set up in the manner of Figure 3 and the tube is supported by a flat plate, the local tube law of Figure 8 no longer applies. Due to the lack of a density-matched external liquid, the transmural pressure is no longer uniform around the perimeter and the tube shape loses one plane of symmetry.

Using the plane of the support as a datum level for pressure, a local tube law was experimentally measured for zero axial strain and no tilt. The previously described values of A_0 and K_p are used to normalize data, with the results for P and c_∞ shown in Figure 9. Disregarding the arbitrary nature of the zero pressure datum, comparison of Figures 8 and 9 reveals that the tube supported by a flat plate is more stiff in the region of the intermediate area ratios. The rather abrupt buckling in the vicinity of $\alpha = 1.0$ is no longer evident and the point of touch contact is delayed to a smaller area ratio of about 0.22. Though the details of this local tube law differ somewhat from the neutrally bouyant case, we do not expect any significant qualitative differences in flow behavior as a consequence.

Steady Supercritical Inlet Flows

In this Section data are presented for two different kinds of experiments; (i) gravity-friction flows, with the test section set up as shown in Figure 3 and employing the local tube law of Figure 9; and (ii) tension-friction flows, with the test section set up as shown in Figure 2 and employing the local tube law of Figure 8 and Table 1.

Gravity-Friction Flows. The experimental arrangement shown in Figure 3 is similar to that used by Griffiths[4] in his investigation of "hydraulic jumps" in collapsible tubes. There are two important consequences of the tube mounting. First, axial tension must be zero at the free end. The effect of fluid friction causes a small (less than 1%), variable axial strain that is maximum at the upstream end and decreases to zero at the free end. The presence of static friction between the tube and the flat plate acts to decrease somewhat the overall level of strain. Since the discussion of gravity-friction flows will be largely of a qualitative nature it is sufficient to note that axial strain is present, though small in magnitude and variable.

The second consequence of the tube mounting is that the lack of a rigid support at the downstream end allows the exit flow to be supercritical. Scrutiny of either Figure 8 or 9 indicates that as the tube approaches a circular shape the infinite wavelength phase velocity c_∞ rises rapidly. Since flow is very likely to be subcritical for such a c_∞, a transition to subcritical flow would have to occur somewhere before the rigid attachment.

Consider an analogous free-surface flow: for a given flow rate supercritical flow is created by a sluice gate (the sphincter) and flows down a constant-slope spillway (the flat plate). Depending on the degree of the slope, the opposing forces of gravity and fluid friction may (i) balance each other resulting in a supercritical flow of constant depth; or (ii) be dominated by gravity and the depth decrease until friction balances; or (iii) be dominated by friction causing the depth to increase to either a stable supercritical depth or to a larger subcritical

depth via the formation of a hydraulic jump. To complete the analogy, consider that in a free surface flow capillary waves due to surface tension may be created and propagate with a phase velocity greater than that of gravity waves.

Wave-less, Shock-less Supercritical Flow. Using the sphincter described in Chapter II, supercritical flows were obtained that were dominated by fluid wall friction. As shown in Figure 10 the area increases from the inlet to approach a constant value. The speed index is supercritical at the inlet and it decreases to a stable supercritical level. Comparison of experimental asymptotes with theoretical values will be done in Chapter VI. For now it is sufficient to demonstrate that by allowing gravity forces to balance frictional forces a constant area supercritical flow can be achieved.

Waves on a Uniform Stream. By appropriately adjusting the sphincter, at a given angle θ, the length required for an asymptotic approach to a constant area can be eliminated (Fig. 11). By carefully bringing a rod into slight contact with the tube near the downstream end, a small disturbance to the supercritical flow was created. As shown in Figure 11, several standing waves appear upstream of the disturbance, their amplitudes diminishing in the upstream direction.

Waves with Shocks. In the procedure just mentioned, more than a slight touch of the rod tended to produce a standing shock (Fig. 12). The shock itself now acts as a disturbance, and waves due to axial tension are able to move upstream against the mean supercritical flow.

The results shown in Figures 10 through 12 were obtained under conditions of small, variable, and unknown axial strain. They are presented primarily to demonstrate qualitatively both the existence and evolution of waves and shocks from a supercritical flow.

Tension-Friction Flows.

With the test section set up as shown in Figure 2 internal pressure and area were measured for a variety of flows. The presence of the density-matched external liquid removes any normal or axial component of gravity and the more refined local tube law of Table 1 applies. Tube axial strain was varied from 0.023 to 0.174 using the adjustable rigid supports, and the adjustable sphincter was used to achieve inlet speed indexes from 1.5 to 10.4.

Typical Data Record. Figure 13a shows the features of a typical traverse through a supercritical inlet flow. From left to right, the unoccluded area ($A-A_p$) trace includes successive segments for: the upstream rigid tube, a short section of inflated tube before the sphincter, a rapid decrease through the sphincter, stationary waves leading to a shock or last jump, a section of inflated tube, and the downstream rigid tubing. The internal pressure, p, is essentially in phase with the area waves throughout. The external pressure p_e is shown as a dashed line. As discussed in Chapter I, the one-dimensional theory predicts that friction causes the area to increase in the flow direction for supercritical flow. Fig. 13a confirms that the mean gradient ($\overline{dA/dx}$) is indeed positive, and also exhibits the maximum gradient $(dA/dx)_{max}$ through the shock.

The same features indicated in Figure 13a can be seen in two photographs of a typical tension-friction flow; Figures 13b and 13c. Figure 13b shows a front view, slightly elevated to accentuate the standing waves. In Figure 13c an angled close-up shot of the same flow reveals four distinct standing waves upstream of a shock-like transition. The lines on the tube are 5 cm apart.

Effect of Downstream Pressure. Once the desired pre-strain is achieved without flow, the rotameter valve is opened and the sphincter set for supercritical flow. Then the downstream valve and the external pressure are adjusted to obtain the longest possible length of supercritical flow. This initial state might be ① as indicated in Figure 14. The shock is then moved upstream to a succession of positions by gradually closing the downstream valve. The shock appears to steepen as it is moved upstream, while still radiating waves of similar wavelength. Even though the downstream valve is successively closed down, the flow rate remains unchanged, as it should for a supercritical inlet flow.

This procedure was repeated for various levels of axial strain, inlet area ratio, and inlet speed index. Although not shown in Figure 14, pressure recordings were also obtained. Through this procedure a large body of data on both standing waves and shocks was obtained.

Example Runs. The three main parameters can be taken to be inlet speed index, S_0, inlet area ratio α_0, and axial strain ε_x. The inlet area ratio was typically kept at a value of about 0.3. Therefore, by considering large and small values of S_0 and ε_x, four broad classes of

supercritical inlet flows can be described. Figure 15a shows the case of small speed index, small strain. The shock is weak and appears more like a large wave that is subcritical at its peak in area. Figure 15b is typical of large speed index, small strain. The wavelengths are small and the shock steep, reaching an inflated state downstream.

The large strain cases are shown in Figures 15c and 15d. It is easy to imagine that Figures 15a and 15b could be simply "stretched out" like coiled springs to yield the large strain cases c and d. Figure 15c indicates that for insufficiently large inlet speed index, the tube strain dominates all flow parameters to produce a linear rise in area from the sphincter to the exit rigid tube. The large strain, large speed index case shown in Figure 15d depicts longer wavelengths and a shock that is not as steep as its low strain counterpart.

In all, about 70 such cases were measured. The parameters, α_0, S_0, and ε_x of these cases are listed in Table 2. In addition, some calculated parameters pertaining to the shock are also presented in Table 2.

Shock Wave Structures

For the purposes of this thesis, a shock will be defined as that portion of the tube with a positive gradient in area, that extends from a local minimum in area (where the flow is supercritical) to a local maximum or plateau in area (where the flow is subcritical). Defined in such a manner, a shock standing in the laboratory frame may be viewed as a diffuser with an inlet area ratio, α_1, that is always partially collapsed and quasi-elliptical in shape, and an exit area ratio, α_2, that is usually circular with a value approximately equal to 1.0.

Such diffusers have no parallel in the literature. Their main feature is that the geometry of the constant-perimeter diffuser is dependent upon the details of the fluid mechanics and vice versa. At the shock inlet, wall curvature is large and dependent upon axial strain and flow parameters. Both the inlet velocity profile and the thickness of the boundary layer are likely to be influenced by the wall curvature. The tendancy for the flow to separate in the expanding region of a diffuser is known to be influenced by the inlet boundary layer thickness and wall curvature[25].

In view of the complex interaction between the fluid and structural mechanics, our first step will be to characterize standing shocks as diffusers; by measuring pressure recovery coefficients. Further on in Chapter VI the shock will be treated as a wave, and an effort will be made to relate such parameters as axial strain, shock steepness, shock inlet speed index and shock inlet area ratio.

Pressure Recovery Coefficient. The pressure recovery coefficient for a diffuser with inlet state 1 and exit state 2 is defined as:

$$C_p \equiv \frac{(p_2 - p_1)}{\frac{1}{2}\rho u_1^2} \tag{8}$$

The loss coefficient is defined as:

$$K_L \equiv \frac{\left(p_1 + \frac{1}{2}\rho u_1^2\right) - \left(p_2 + \frac{1}{2}\rho u_2^2\right)}{\frac{1}{2}\rho u_1^2} \tag{9}$$

But this can be expressed as

$$K_L = 1 - C_p - \left(\frac{\alpha_1}{\alpha_2}\right)^2 \tag{10}$$

In view of this, it is sufficient to discuss experimental and theoretical pressure recovery coefficients alone. An upper limit on C_p follows from Eq. (10) by assuming the flow to be loss-less, i.e. by setting $K_L = 0$:

$$C_{p_{max}} = 1 - \left(\frac{\alpha_1}{\alpha_2}\right)^2 \tag{11}$$

In order to establish a reasonable lower bound on C_p, some assumptions must be made on the nature of the loss mechanism. One limit based on the Carnot-Borda "sudden expansion" was suggested by Shapiro[8]. Figure 16 shows an idealized shock, stationary in the lab frame, with one-dimensional flow at the inlet and exit. The essential assumptions are (1) the jet separation is so sharp that the pressure acting on the area (A_2-A_1) is the inlet pressure p_1, and (2) there is no wall shear stress acting on the walls in the expanding region.

For the control volume shown, conservation of mass yields:

$$u_1 A_1 = u_2 A_2 \tag{12}$$

conservation of momentum yields:

$$A_2 (p_1-p_2) = \rho A_1 u_1 (u_2-u_1) \tag{13}$$

Combining Eqs. (8), (12), and (13) gives for the pressure recovery coefficient:

$$C_{p_c} \equiv 2 \frac{\alpha_1}{\alpha_2} \left(1 - \frac{\alpha_1}{\alpha_2}\right) \tag{14}$$

This will be referred to as the Carnot pressure recovery. It represents a lower bound for cases when the effect of wall shear within the expanding region is negligible.

Oates[7] has suggested that the assumption of complete jet separation is unrealistic and unnecessary. He chose instead to let the wall pressure in the rapidly expanding region be determined by a local tube law. In addition, he also neglected the effect of wall shear stress in the expanding region. Employing these assumptions we arrive at another expression for the pressure recovery coefficient:

$$C_{p_o} = C_{p_c} + \frac{K_p}{\left(\frac{1}{2}\rho c_{\infty_1}^2\right) S_1^2} \left\{ \frac{1}{\alpha_2} \int_2^1 P(\alpha) d\alpha - P(\alpha_1) \left[1 - \alpha_1/\alpha_2\right] \right\} \tag{15}$$

Using the local tube law of Table 1 and letting $\alpha_1 = 0.4$, $S_1 = 6.3$, and $\alpha_2 = 1.0$ Eq. (15) yields a small increase over the Carnot pressure recovery coefficient. The smallness of this change is a consequence of the shape of the P-α curve of the local tube law: the wall pressure doesn't begin to rise substantially with area until just before reaching the circular state. Even if the shape of the local tube law was substantially different, it is highly unlikely that it would apply in a region of rapidly changing area. The presence of even minimal axial strain, as well as axial bending effects, may interact strongly with the complex three-dimensional structural shape of the rapid expansion in area.

Experimental Pressure Recovery. Figure 17 shows a plot of experimental C_p versus inlet area ratio α_1. Three curves are also indicated for $C_{p_{max}}$, C_{p_c}, and C_{p_o}. The curve for C_{p_o} results from Eq. (15), letting $\alpha_1 = 0.4$, $S_1 = 6.3$, $\alpha_2 = 1.0$, and using the local tube law of Table 1. The results have been loosely categorized by the parameter $(1/\alpha_1)(d\alpha/d\xi)_{max}$; where $\xi \equiv x/D_0$, a non-dimensional axial distance. As evident in Figure 17, when this parameter is less than 0.30 the data fall below the Carnot pressure recovery. This simply indicates that such shocks are long and gradual enough in slope for wall friction losses to be important relative to pure expansion-type losses.

Johnston[26] has reviewed the literature on two-dimensional straight-walled diffusers. The steepest shocks we observe have approximate open angles of no greater than 15°, and our pressure recovery coefficients are consistent with those of a comparable two-dimensional straight-walled diffuser. In addition, it appears that an open angle of 15° is much too small to reach a regime of either full stall or jet flow. Qualitative observations on the degree of unsteadiness present in our shocks seem consistent with operation in the regime of no appreciable stall or, at worst, transitory stall with quasi-periodic unsteadiness.

CHAPTER IV:

THEORY: EFFECTS DUE TO AXIAL TENSION AND BENDING

Flows of the type discussed in Chapter III are extremely complex owing to the three-dimensionality of both the flow and tube geometry. As a result, such flows are difficult to model accurately. The primary difficulty arises not so much from the three-dimensional aspects of the flow, but rather from the three-dimensional aspects of the structural mechanics. Additionally, in the shock region, there are complex fluid-structural interactions.

Because of the difficult nature of the coupling between fluid and structural forces, rigorous solutions cannot readily be obtained. Even if such solutions were possible, the complexity of the detailed results would likely obscure the most important physical phenomena taking place. For these reasons, a relatively simple theoretical model has been developed and analyzed. Since the assumptions of the model impose certain limits on the generality of the solutions, each is thoroughly discussed below.

Flow Equations: Basic Assumptions. Though this thesis deals primarily with steady flows, the equations are formulated for unsteady flow, as a basis for the investigation of wave propagation in Chapters V and VI.

The flow is treated as one-dimensional in terms of a pressure $p(x,t)$ and velocity $u(x,t)$ which are assumed to be uniform over each cross-section of the tube. These conditions are satisfied if the longitudinal area gradients are small ($[D_0/A][dA/dx] \ll 1$) or equivalently, if the characteristic wavelength is long compared with the local tube diameter.

Flows of sufficiently high velocity to be supercritical are typically turbulent. Consequently the velocity profile is blunted (consistent with the one-dimensional assumption) and the fluid wall shear stress can be predicted using a skin friction coefficient defined as $f \equiv 2\tau_w/\rho u^2$ where τ_w is the wall shear stress, and ρ the fluid density. The one-dimensional assumption implies that all losses must be reflected through the wall shear stress by the skin friction coefficient. In subsequent analyses, f is assumed to have two components. The first, $\bar{f}$, is a constant and equal to the appropriate value for steady, fully developed turbulent flow in a tube of uniform cross-sectional area. The second part, f', is a general sinusoidal perturbation of smaller absolute value. The physical basis for the oscillatory component is discussed later in connection with the modelling of wave propagation and decay. A review of skin friction coefficients appropriate for cases other than fully developed turbulent flow (e.g. laminar, similarity region, etc.) can be found in the work of Kececioglu[17], or Kamm[27].

Implicit in the above discussion is the assumption that flow separation does not occur. Indeed, the results discussed in Chapter IV indicate that for the large majority of shocks, large-scale separation does not occur. In the interest of simplicity, we shall continue with the one-dimensonal assumption in an effort to define its limitations, particularly in regards to shocks.

The Tube Model. It is our intention to model the structural mechanics of the tube in such a way as to include both the local tube law and effects due to axial tension and bending. For axial variations in area of very

long wavelength, the transmural pressure can be considered a function of area ratio alone. Though the effect of circumferential bending stiffness is to produce an equilibrium cross-sectional configuration of considerable complexity, detailed knowledge of the radial wall displacement is not required.

However, in the presence of area variations of finite wavelength, axial tension and bending are capable of providing addition transmural stiffness. In order to model these effects rigorously, complete knowledge of the tube surface deformation is required. It is not our intention, however, to attempt to solve the enormously complicated three-dimensional structural problem. Instead, we seek a simple geometric configuration for the tube cross-section that will allow us to incorporate the effects of axial tension and bending in a two-dimensional manner.

Such a configuration is depicted in Figure 18. The separation distance between the two parallel surfaces and the diameter of the semi-circular regions are both 2η. It is assumed that, as the tube deforms due to changes in transmural pressure, η changes while both the perimeter and the geometric configuration remain unchanged. Thus, the cross-sectional area is given by the expression:

$$A = 2\pi\eta\left(R_0 - \frac{1}{2}\eta\right) \tag{16}$$

where R_0 is the radius of a circular tube having the same perimeter as the partially collapsed vessel. In dimensionless form this becomes:

$$\alpha \equiv \frac{A}{A_0} = \left(2 - \frac{\eta}{R_0}\right)\frac{\eta}{R_0} \tag{17}$$

or, solving for η:

$$\eta = R_0\left(1 - \sqrt{1-\alpha}\right) \tag{18}$$

This geometric model is intended to represent the tube in a partially collapsed state. We expect this model to be a reasonable one for several reasons. (1) The actual tube configurations resemble flattened ellipses in the range of partial collapse, (2) though the P-α relation is non-analytic in this region, c_∞ is nearly constant over a wide range of area ratios, and (3) as discussed in Chapter III, the region of partial collapse ($0.27 \lesssim \alpha \lesssim 0.80$) also exhibits the lowest values of c_∞, making supercritical flow most likely for such shapes. Using the model of Figure 18 and Eqs. (17) and (18) we now proceed to develop an approximate constitutive relationship between cross-sectional area and transmural pressure.

The Tube Law. The transmural pressure acting locally can now be thought of as being supported in part by circumferential bending stresses as reflected by the local tube law, and in part by stresses within the tube wall induced by longitudinal curvature. Following this line of reasoning, a modified tube law is sought in the general form:

$$(p - p_e) = \underbrace{K_p\, P(\alpha)}_{\substack{\text{for the} \\ \text{real tube}}} + \underbrace{\Delta p_t + \Delta p_b}_{\substack{\text{for the} \\ \text{assumed model}}} \tag{20}$$

where Δp_t and Δp_b represent the tendency of the tube to resist collapse due to the effects of axial tension and bending, respectively.

Axial Tension. To obtain an estimate of the influence of axial tension, consider one-dimensional deflections of a narrow axial strip of tube wall on either the top or bottom surface. If, at some point, the local radius of curvature in the axial direction is R, and in the circumferential direction is infinite, then membrane stresses are capable of supporting a pressure difference of:

$$\Delta p_t = - T/R \tag{21}$$

where $T = \epsilon_x Eh$ is the axial force per unit perimeter resulting from an axial strain ϵ_x. For small deflections R can be approximated by $(d^2\eta/dx^2)^{-1}$ for the model of Figure 18. This approximation is justified when $(d\eta/dx)^2 \sim (\Delta\eta/\lambda)^2 << 1$, where λ is the characteristic distance over which a variation of $\Delta\eta$ occurs. Using Eq. (18) to express the curvature in terms of the area ratio and substituting into Eq. (21) leads to:

$$\Delta p_t \cong - \frac{TR_0}{2} \left[\frac{1}{\sqrt{(1-\alpha)}} \frac{d^2\alpha}{dx^2} + \frac{1}{2\sqrt{(1-\alpha)^3}} \left(\frac{d\alpha}{dx}\right)^2 \right] \tag{22}$$

Several points need to be made in relation to Eq. (22). It is desirable, from an analysis point of view, to keep only the leading, linear term. The relative importance of the nonlinear term can be assessed by taking the ratio of the nonlinear term to the linear term, revealing that when $\Delta\alpha/[2(1-\alpha)] << 1$ the nonlinear term is negligible. Here $\Delta\alpha$ is the change in α that occurs over the characteristic distance λ.

For typical standing waves of area, as discussed in Chapter III ($\Delta\alpha \sim 0.05$, $\alpha \sim 0.40$) the ratio has an approximate value of 0.04, implying the nonlinear term is indeed negligible for small amplitude waves. However, in the region of the shock ($\Delta\alpha \sim 0.60$, $\alpha \sim 0.60$) the ratio is of order one, suggesting that the nonlinear term is important for large amplitude phenomena.

Were it not for the presence of the $\sqrt{1-\alpha}$ term in the denominator of *both* terms it might be reasonable to include the nonlinear term, at least when known to be significant. In fact, as the nonlinear term becomes important, typically in a rapid, shock-like transition with $\alpha \to 1.0$, the model as a whole begins to break down due to the singular behavior of the geometric configuration. In view of this increasing uncertainty, the nonlinear term is neglected entirely. As a result, we do not expect the modelling of axial tension to be as appropriate for shock-like transitions as for the case of small amplitude waves. Thus, Eq. (22) becomes:

$$\Delta p_t \simeq -\frac{TR_0}{2\sqrt{(1-\alpha)}}\frac{d^2\alpha}{dx^2} = -\frac{T}{\sqrt{4\pi(A_0-A)}}\frac{d^2A}{dx^2} \qquad (23)$$

Strictly, speaking, T is a function of axial distance. For a tube of initial length L_0, mounted between fixed rigid supports separated by a distance L the axial force per unit perimeter is:[28]

$$T(x) = Eh\left(\frac{L-L_0}{L_0}\right) + \frac{Eh}{L_0}\int_0^L \left[\sqrt{1+\left(\frac{d\eta}{dx}\right)^2} - 1\right] dx$$

$$+ \int_0^L \left(\frac{L-x}{L}\right)\sqrt{1+\left(\frac{d\eta}{dx}\right)^2}\,\tau_w(x)dx - \int_0^x \sqrt{1+\left(\frac{d\eta}{dx}\right)^2}\,\tau_w(x)dx \qquad (24)$$

The first term represents the pre-strain applied to the tube under no-flow conditions. The second is the increment in strain associated with stretching the tube under flow loading, and the third and fourth are due to wall shear stress. For the majority of experiments reported in Chapter III only the term representing pre-strain is significant. For the purposes of this thesis T will be assumed constant.

Axial Bending. Using similar reasoning, the effect of axial bending of the two parallel surfaces of the geometric configuration can be approximated by a fourth order term of the form:

$$\Delta p_b \approx EI \frac{d^4\eta}{dx^4} \tag{25}$$

where the bending moment I is equal to $h^3/[12(1-\nu^2)]$. Expressed in terms of the area or area ratio:

$$\Delta p_b \approx \frac{R_0^4 K_p}{2\sqrt{1-\alpha}} \frac{d^4\alpha}{dx^4} = \frac{R_0^3 K_p}{\sqrt{4\pi(A_0-A)}} \frac{d^4A}{dx^4} \tag{26}$$

Here four nonlinear terms have been neglected. In a manner similar to that just described for the case of axial tension, the nonlinear terms have been compared (details not shown) to the one linear term and shown to be negligible for the case of small amplitude waves. Not surprisingly, the nonlinear terms are very important relative to the linear term for the case of shock-like transitions. Again, the expression of Eq. (26) is not expected to be valid as the tube approaches the circular configuration, or for the case of large amplitude phenomena.

Combining Eqs. (23) and (26) with Eq. (20) leads to the following form for a modified tube law:

$$(p-p_e) = K_p \left[P(\alpha) + \frac{R_0^3}{\sqrt{4\pi(A_0-A)}} \frac{d^4A}{dx^4} \right] - \frac{T}{\sqrt{4\pi(A_0-A)}} \frac{d^2A}{dx^2} \qquad (27)$$

Implicit in Eq. (27) are several assumptions in addition to those already mentioned. First, it is assumed that circumferential bending and axial bending and tension act independently and, as a result, the effects can simply be superimposed. Although coupling is certainly important for large deformations (e.g. a corrugated sheet of paper is more resistant to bending than a flat sheet), if the deformations are small enough so that this linearized model is valid, then these effects should be minimal.

The second assumption, and perhaps the most difficult to justify, is that bending and tension stresses, as modelled on the upper and lower surfaces, are representative of those acting on the entire circumference.

Consider for example, axial tension which, as is shown shortly, generally dominates over axial bending forces. If, at the point of interest, the area reaches a local minimum the second derivative of area with respect to distance is positive and tension tends to pull the upper and lower walls further apart, thereby increasing the area. Over much of the side walls, however, tension pulls the surfaces inward, seeming to counteract the anticipated area increase. This is not the case, however, since both motions are consistent with an increase in area for a tube of fixed perimeter ... i.e. both forces tend to produce a more rounded shape. Thus the net effect of tension on the entire circumference is consistent with the model.

Swidler[29] modified the numerical procedure of Flaherty *et al.*[22] to include a circumferentially varying transmural pressure due to axial tension and curvature. Keeping the transmural pressure due to tension small compared to that due to circumferential bending stiffness, Swidler was able to estimate the error that results from the simple model of Eq. (27). For small variations ($\Delta\alpha \sim 0.05$) about area ratios in the range of 0.30 to 0.80 she found the simple model of Eq. (27) to be surprisingly good. Swidler showed that the circumferentially distributed model predicts an effective transmural pressure due to axial tension that is 10-30% less than that based on Eq. (27), with the error largely independent of area ratio. It seems likely that such a consistent and small error may be the result of differences in circumferential geometry between the two approaches. If this is the case, it might be possible in the future to use the method of Swidler to remove the singularity at $\alpha = 1.0$, that arises as a consequence of the $\sqrt{1-\alpha}$ term in the denominator. At present, however, the model of Eq. (27) must fail as $\alpha \to 1.0$.

To summarize, the modified tube law is expected to predict quantitatively correct behavior for small amplitude standing waves superimposed on mean area ratios of less than 0.80. For cases of larger area ratios and shock-like changes in area we can expect the modified tube law to predict qualitatively correct behavior at best.

Governing Equations. The continuity equation for an incompressible fluid, consistent with assumptions already given is:

$$\frac{\partial A}{\partial t} + \frac{\partial}{\partial x}(uA) = 0 \qquad (28)$$

where x is axial distance and t is time. For an unsteady flow with friction the momentum equation for a fluid element can be written as

$$\frac{\partial u}{\partial t} + u \frac{\partial u}{\partial x} + \frac{1}{\rho} \frac{\partial p}{\partial x} + g \frac{dz}{dx} + \frac{2u^2 f}{D_e} = 0 \qquad (29)$$

where D_e is the hydraulic diameter, g is the acceleration of gravity, and z is the elevation of the tube. The relationship between transmural pressure and cross-sectional area to be used in the subsequent analysis is of the form of the modified tube law, Eq. (27).

Methods of Solution. Solutions to the governing equations are sought by two different methods. An unsteady, linearized analysis is carried out primarily to gain some understanding of small amplitude wave propagation phenomena; including the finite wavelength dispersion relation and the influence of wall shear stress on wave amplitude decay. Solutions are sought for small perturbations in area and velocity about mean values. A similar form is also assumed for the skin fraction coefficient:

$$\begin{aligned} A &= \bar{A} + A'(x,t) \qquad A'/\bar{A} \ll 1 \\ u &= \bar{u} + u'(x,t) \qquad u'/\bar{u} \ll 1 \\ f &= \bar{f} + f'(x,t) \qquad f'/\bar{f} \ll 1 \end{aligned} \qquad (30)$$

Since the unsteady phenomena were manifested experimentally as waves stationary in the laboratory frame, the degree of applicability of the

linearized analyses is investigated by numerically integrating the full nonlinear governing equations for steady flow. The goal of the numerical analysis is to verify small amplitude behavior and study large amplitude effects through results in the form of axial distributions of area, velocity, speed index, and pressure. The details of the numerical analysis are presented in Chapter VII.

CHAPTER V:

LINEAR ANALYSIS OF THE GOVERNING EQUATIONS

Linearization of the Governing Equations. Here we seek a solution for A'(x,t), the fluctuating component of the area. Substituting the expressions of Eq. (30) into continuity, Eq. (28), gives a linearized continuity equation:

$$\frac{\partial A'}{\partial t} + \bar{u}\frac{\partial A'}{\partial x} + \bar{A}\frac{\partial u'}{\partial x} = 0 \qquad (31)$$

Here terms of the type (u')·(A') have been neglected.

Upon solving Eq. (31) for $\frac{\partial u'}{\partial x}$, it is apparent that derivatives of u' with respect to space or time can be expressed in terms of mean quantities and derivatives of A'. Substituting Eq. (30) into the momentum equation, (Eq. (29)), introducing the modified tube law of Eq. (27), assuming constant external pressure, and employing the definition of infinite wave length phase velocity (Eq. (1)), yields the following:

$$\frac{\partial u'}{\partial t} + \bar{u}\frac{\partial u'}{\partial x} + \frac{c_{\infty}^2}{\bar{A}}\frac{\partial A'}{\partial x} - \frac{T}{\pi\rho D_0}\left[1 - \bar{A}/A_0\right]^{-1/2}\frac{\partial^3 A'}{\partial x^3} +$$

$$\frac{K_p R_0^2}{2\pi\rho}\left[1 - \bar{A}/A_0\right]^{-1/2}\frac{\partial^5 A'}{\partial x^5} + g\frac{dz}{dx} + \frac{1}{2}\pi\frac{D_0\bar{f}\bar{u}^2}{\bar{A}}\left[1 + \frac{2u'}{\bar{u}} - \frac{A'}{\bar{A}} + \frac{f'}{\bar{f}}\right] = 0 \qquad (32)$$

To remain consistent with the assumed form of the area, that of small fluctuations about a constant mean value, it is necessary to eliminate the terms in Eq. (32) that don't involve fluctuating components. This is

accomplished mathematically just as it is done physically (Chapter III) by allowing the axial component of gravity to balance the mean friction term:

$$g \frac{dz}{dx} = - \frac{1}{2} \pi \frac{D_0 \bar{f} \bar{u}^2}{\bar{A}} \tag{33}$$

Now, differentiation of Eq. (32) with respect to x and replacement of terms in u' by equivalent expressions involving A' yields a linear sixth order partial differential equation for A'(x,t):

$$\frac{\partial^2 A'}{\partial t^2} + 2\bar{u} \frac{\partial^2 A'}{\partial x \partial t} + \left(\bar{u}^2 - c_\infty^2\right) \frac{\partial^2 A'}{\partial x^2} + \frac{T \bar{\alpha} D_0}{4\rho} \left[1 - \bar{A}/A_0\right]^{-1/2} \frac{\partial^4 A'}{x^4} -$$

$$\bar{\alpha} \frac{K_p R_0^4}{2\rho} \left[1 - \bar{A}/A_0\right]^{-1/2} \frac{\partial^6 A'}{\partial x^6} + \frac{1}{2} \pi \frac{D_0 \bar{f} \bar{u}^2}{\bar{A}} \left[\frac{2}{\bar{u}} \frac{\partial A'}{\partial t} + 3 \frac{\partial A'}{\partial x} - \frac{\bar{A}}{\bar{f}} \frac{\partial f'}{\partial x}\right] = 0 \tag{34}$$

Small Amplitude Travelling Waves. We seek a solution for A'(x,t), that has the general form of a sinusoidal small amplitude travelling wave, damped spatially but not temporally:

$$A'(x,t) = \hat{A} e^{i(\omega t - kx)} = \hat{A} e^{k_i x} e^{ik_r(ct-x)} \tag{35}$$

Equation (35) represents a wave solution for A'(x,t) in the conventional form of a complex exponential with amplitude $\hat{A}$, real frequency $\omega = ck_r$, and complex wave number $k = k_r + ik_i$. The real phase speed is represented by c, the real part of the wave number is $k_r = 2\pi/\lambda$, and the imaginary part of the wave number k_i provides spatially dependent wave

amplitude growth in the + x direction. It is to be understood that when employing the form of a complex exponential only the real part is of interest in the final analysis.

Typically, for such small amplitude waves, the real phase speed c is not strongly affected by viscous effects. Therefore, we assume c to be purely real and chose a complex wave number to examine the influence of viscous dissipation on wave amplitude.

Hsu and Kennedy[30] have shown that for turbulent flow through wavy-walled pipes, the oscillatory component of wall skin friction coefficient f' varies nearly sinusoidally with the same wavelength as the area variations but with a different phase. The phase shift is due mainly to convective or "history effects" in the boundary layer. Thus, we assume a form for f' that is sinusoidal with a phase angle relative to the area of ϕ:

$$f'(x,t) = \hat{f}\, k^m\, D_0^m\, e^{i(\omega t - kx + \phi)} \tag{36}$$

Here $\hat{f}$ is a small constant, and m is an arbitrary integer that may be used to evaluate various wave number dependencies for the amplitude of f'. Substituting Eqs. (36) and (35) into Eq. (34) leads to:

$$\left[\frac{K_p R_0^4 \bar{\alpha}}{2\rho\sqrt{1-\bar{\alpha}}}\right] k^6 + \left[\frac{T D_0 \bar{\alpha}}{4\rho\sqrt{1-\bar{\alpha}}}\right] k^4 + \left[c_\infty^2 - (\bar{u} - c)^2\right] k^2$$

$$+ \frac{2\bar{u}^2\bar{f}}{D_0\bar{\alpha}}\left[\frac{2c}{\bar{u}} - 3 + \frac{\bar{A}}{\hat{A}}\frac{\hat{f}}{\bar{f}}\left(D_0^m k^m\right) e^{i\phi}\right] ki = 0 \tag{37}$$

In the sections to follow various degenerate forms of this equation are solved, and the corresponding physical interpretations discussed.

The Inviscid Dispersion Relation. One of the most fundamental characteristics of a system exhibiting wave propagation is the inviscid dispersion relation or $c(\lambda)$. For small amplitude waves propagating in stagnant fluid without viscous losses, $\bar{u} = 0$ and $\bar{f} = 0$ in Eq. (37). Thus, equation (37) becomes:

$$\left(\frac{K_p R_0^4 \bar{\alpha}}{2\rho\sqrt{1-\bar{\alpha}}}\right) k^6 + \left(\frac{T D_0 \bar{\alpha}}{4\rho\sqrt{1-\bar{\alpha}}}\right) k^4 + \left(c_\infty^2 - c^2\right) k^2 = 0 \qquad (38)$$

Solving for c as a function of λ leads to:

$$c^2 = c_\infty^2 + \frac{\pi^2 T D_0 \bar{\alpha}}{\rho\lambda^2\sqrt{1-\bar{\alpha}}} + \frac{8\pi^4 R_0^4 K_p \bar{\alpha}}{\rho\lambda^4\sqrt{1-\bar{\alpha}}} \qquad (39)$$

For this case the wave number, $k = \frac{2\pi}{\lambda}$, is real with no imaginary part. In Eq. (39) the phase speed is composed of three parts: one is just the infinite wave length phase velocity that arises from the local tube law, the second is due to axial tension, and the third results from axial bending stiffness.

Group Velocity. For a dispersive system the group velocity, or velocity at which wave energy propagates will be[31]; using Eq. (39):

$$c_g \equiv c - \lambda \frac{dc}{d\lambda} = c\left[2 - \frac{c_\infty^2}{c^2}\right] \qquad (40)$$

From Eq. (39) it is evident that c is a single-valued function of λ and that for any $\lambda > 0$ the phase velocity c exceeds the infinite wavelength phase velocity c_∞. Since $c_\infty/c < 1$ it can be seen from Eq. (40) that the group velocity is always greater than the phase velocity c, or summarizing for our system:

$$c_g > c > c_\infty \tag{41}$$

The Radiation Condition. In order to have finite wavelength dispersive waves standing in a steady supercritical flow three criteria must be satisfied: (1) the flow must be supercritical, $u > c_\infty$; (2) the local phase velocity corresponding to a particular wavelength must be equal to the mean fluid speed, $u = c$; and (3) the group velocity must be greater than or equal to the corresponding phase velocity, $c_g \geq c$, if the disturbance is downstream and wave energy is to propagate upstream against the mean flow.

If the shock, as described in Chapter III, acts as the disturbance, Eq. (41) indicates that dispersive waves may propagate upstream ($c < 0$) and stand at a position where $-u = c$. If, on the other hand, the disturbance is assumed to be upstream, dispersive waves will propagate downstream ($c > 0$) with the mean flow at a velocity $(u + c)$ and never become stationary. Therefore, by considering the shock to be the disturbance or source of wave energy, the three criteria are satisfied. In discussing the effect of viscous dissipation on wave amplitude later on in Chapter VI it will be physically correct to say that the standing waves decay in amplitude in the -x or upstream direction.

Relative Importance of Axial Bending. From Eq. (39) the wave speed due to axial bending alone is

$$c_b = \sqrt{\frac{\pi^4 D_0^4 K_p \bar{\alpha}}{2\rho\lambda^4\sqrt{1-\bar{\alpha}}}} \tag{42}$$

and the wave speed due to axial tension alone is

$$c_t = \sqrt{\frac{\pi^2 T D_0 \bar{\alpha}}{\rho\lambda^2\sqrt{1-\bar{\alpha}}}} \tag{43}$$

Taking the ratio c_b/c_t and replacing K_p by $(1/12)E(h/R_0)^3/(1-\nu^2)$ with $\nu = 0.5$, and letting $T = \varepsilon_x Eh$ yields

$$\frac{c_b}{c_t} \approx \frac{2}{\sqrt{\varepsilon_x}}\left(\frac{h}{\lambda}\right) \tag{44}$$

The ratio (h/λ), wall thickness to wavelength ranges experimentally from approximately 0.005 to 0.02; with axial strain ranging from 0.023 to 0.174. Therefore, the ratio c_b/c_t ranges from 0.02 to 0.26. A comparison of the terms in Eq. (39) for the case of the shortest waves (5 cm), the smallest axial strain (0.023), and an area ratio of 0.40 reveals the following:

$$c^2 = c_\infty^2 + \frac{\pi^2 T D_0 \bar{\alpha}}{\rho\lambda^2\sqrt{1-\bar{\alpha}}} + \frac{\pi^4 D_0^4 \bar{\alpha} K_p}{2\rho\lambda^4\sqrt{1-\bar{\alpha}}}$$

$$(700) + (1200) + (360)$$

For this worst case, neglecting axial bending results in a difference in c of less than 10%. Considering the assumptions made in arriving at the model for axial bending, as well as the added complexity required to deal

with the higher order term, it seems reasonable to neglect the influence of axial bending in discussing the experimental results of this thesis.

Comparison with Experiments. Neglecting axial bending and letting $c = -u$ for the case of waves standing in the laboratory frame, Eq. (39) can be written as:

$$\sqrt{S^2 - 1} = \left[\lambda \sqrt{\frac{\rho c_\infty^2 \sqrt{1-\bar{\alpha}}}{\pi^2 D_0 T \bar{\alpha}}} \right]^{-1} \tag{45}$$

This relation is based on the assumption that viscous effects are not important in considering the wavelengths of waves that are stationary in a steady supercritical flow. Eq. (45) implies that at any location among standing waves, $S \sim 1/\lambda$. By comparing experimental results with the relation of Eq. (45) we can critically examine not only the inviscid assumption, but the model for axial tension as well.

For the experiments performed on tubes with finite axial pre-strain, peak-to-peak and trough-to-trough wavelengths and corresponding mean area ratios were measured. The data are plotted in Figure 19 in a log-log form suggested by Eq. (45). The theoretical result predicted by Eq. (45) is indicated as a dashed line of slope -1. The agreement with experiments is remarkable considering the nature of the model, which contains no dimensionless constants, though it is approximate in many respects.

Recall that in Chapter IV we discussed how the results of Swidler[29] indicate that our basic model for axial tension (Eq. 27) may overestimate the effective transmural pressure by approximately 30%. If we introduce an appropriate dimensionless constant of 0.70 into Eq. (45), multiplying

T, we obtain a modified theoretical result similar to Eq. (45) that is shown in Figure 19 as a dotted line, shifted somewhat downward. Except for a few data points, largely those corresponding to the lowest level of axial strain, all the data falls above the modified theoretical result. This provides further confirmation that except for the lowest strains, the result of Swidler[29] is reasonable in its verification of our simple model for axial tension.

The fact that the data points corresponding to the lowest level of axial strain fall the farthest below the dashed line of Eq. (45) is consistent with the possibility that axial bending may be influencing the data. If this were the case, the direction of the shift is in accordance with the result of Eq. (39); that for a constant speed index S a smaller wavelength should exist if axial bending is becoming significant.

Having considered how the models for axial tension and bending influence the results shown in Figure 19, we can now conclude that indeed it appears that viscous effects have a negligible influence on the observed wavelengths. This is fortunate, since it is known that viscous effects cause the mean gradient in area, and it will be shown in Chapter VI that viscous effects have a large influence on the amplitude of the waves.

CHAPTER VI:

DECAY OF STANDING WAVES IN A STEADY FLOW

In Chapter V it was shown that without dissipation ($f = 0$) small amplitude finite wavelength travelling waves will propagate according to the dispersion relation, Eq. (39), with no decay in wave amplitude. In addition, we established the radiation condition, showing that the experimentally observed standing waves originate in the shock region and decay in amplitude in the upstream direction.

In this Chapter we examine the influence of an assumed constant mean skin friction coefficient, $\bar{f}$, on both changes in mean area and wave amplitude decay. The effect of a spatially oscillatory perturbation in the skin friction coefficient, f', on wave amplitude decay is also discussed.

Consequences of a Constant Skin Friction Coefficient

Constant Area Supercritical Flow. As discussed in Chapter III, if the downstream end of the collapsible tube is free and not attached to a rigid tube, constant area supercritical flow is attainable. This occurs when the axial component of gravity just balances the frictional forces, as expressed by Eq. (33). Solving for the area ratio from Eq. (33) yields:

$$\alpha = \sqrt[3]{\frac{2\bar{f}u_0^2}{D_0 g \sin\theta}} \qquad (46)$$

where u_0 is the flow rate divided by the neutral area (Q/A_0), and θ is the

angle of the flat plate with the horizontal.

In arriving at a model for the mean skin friction coefficient several assumptions are made. For the gravity-friction experiments Reynolds numbers based on the hydraulic diameter ranged from 2,600 to 12,500, encompassing flows from transition to turbulence to fully turbulent. We make the simplifying assumption that the viscous effects can be modelled by neglecting inlet effects and treating the flow as fully developed and turbulent. The value of $\overline{f}$ is taken to be that typically used for fully developed turbulent flow in a smooth-walled tube of uniform area and cross-sectional shape; the Blasius relation[32]:

$$\overline{f} = \frac{0.3164}{4} R_e^{-0.25} \tag{47}$$

This relation is strictly valid only if the Reynolds number is less than 100,000. For fully developed turbulent flow in non-circular ducts Eq. (47) is valid as long as the cross-sectional shape has no sharp corners and the hydraulic diameter is used as the characteristic dimension. The hydraulic diameter is assumed to be equal to four times the cross-sectional area divided by the wetter perimeter:

$$D_e = \frac{4A}{P} = \alpha D_0 \tag{48}$$

For the limited number of experiments wherein the effects of gravity and friction resulted in asymptotically constant areas, Eq. (46) is used to calculate the experimental skin friction coefficient. A log-log plot of $\overline{f}_{exp}$ versus Reynolds number is shown in Figure 20, with both the Blasius

relation, Eq. (47), and the laminar result indicated as dashed lines.

As shown in Figure 20 the experimental data fall above the Blasius relation and are loosely fitted by an expression, $\overline{f}_{exp} \approx R_e^{-1/2}$. It is not surprising that the data fall above a prediction based on fully developed turbulent flow, particularly for the lower Reynolds numbers. In this regime inlet effects may be significant. At the higher Reynolds numbers the agreement with the Blasius relation is somewhat better. Considering that $\overline{f}_{exp} \sim \alpha^3$, this method for investigating the mean skin friction coefficient may be overly sensitive to errors in α.

Mean Area Increase with Waves. Griffiths[4] has shown that in supercritical flow friction causes the area to increase in the flow direction. This result will become apparent from the full nonlinear governing equations as they are arranged for numerical solution in Chapter VII. For the purposes of this discussion, the equation for the gradient in area ratio when tension effects are absent or small is simply:

$$\frac{d\alpha}{d\xi} = 2 f \left(\frac{S^2}{S^2 - 1} \right) \tag{49}$$

where ξ is a non-dimensional distance (x/D_0). It is evident from Eq. (49) that if $S^2 >> 1$, and the skin friction coefficient f is constant, then the gradient ($d\alpha/d\xi$) will be constant as long as ($dS/d\xi$) is small. That f may be constant through the region of partial collapse is not unlikely, since for a tube of constant wetted perimeter the Reynolds number based on the hydraulic diameter will be a constant for any given flow rate.

For the majority of experiments involving finite pre-strain, this appears to be the case. Even though axial tension results in the presence of standing waves, the waves are typically superimposed on a rather constant gradient in area. This implies that f', the fluctuating component of f, is either too small in amplitude to have any effect whatsoever; or simply that if it is indeed nearly sinusoidal, its average effect over a wavelength is small.

For a representative number of experiments spanning a range in Reynolds number of 3,700 to 13,000, the gradient in area through the waves was measured graphically. Using Eq. (49), the experimental skin friction coefficient was calculated for values of $(\overline{d\alpha}/d\xi)_0$ and S_0, near the inlet. The results are displayed in Figure 21 on a log-log plot of $\overline{f}_{exp}$ versus Reynolds number.

Though the measurement of the mean gradient in area is not precise, and the range of gradients is admittedly small, the data fall quite close to the Blasius relation as indicated by the dashed line in Figure 21. The improved agreement, compared to that of the gravity-friction flows shown in Figure 20, may be a consequence of the presence of the standing waves. One might argue, for instance, that inlet effects would be disrupted by the waviness of the tube wall, much as a small wire can trip a laminar or transition flow into a more fully developed turbulent flow. The improved agreement may also be due to the method of calculating $\overline{f}_{exp}$ from Eq. (49). Though the measurement of the mean gradient is technically not as precise as the measurement of local area ratio, $\overline{f}_{exp}$ is now directly proportional to $(\overline{d\alpha}/d\xi)$ rather than α^3 as for the gravity-friction flows.

Mean Pressure Rise with Waves. It is appropriate at this point to discuss the change in mean internal pressure that results from a mean gradient in area. As indicated in Figure 13a, a plot of a typical data record for a tension-friction flow, the internal pressure oscillates spatially in phase with the area variations of the standing waves. That an accompanying positive mean gradient in pressure is not as evident as the gradient in area can be shown by a simple calculation. In the region of partial collapse we can estimate the magnitude of $(\overline{dP}/dx)$ as:

$$\left(\frac{\overline{dP}}{dx}\right) \approx \left(\frac{\overline{dA}}{dx}\right)\left(\frac{\partial P}{\partial A}\right) = \frac{\rho c_\infty^2}{\alpha D_0}\left(\frac{\overline{d\alpha}}{d\xi}\right) \qquad (50)$$

Using typical values of $(\overline{d\alpha}/d\xi) \sim 0.02$, $c_\infty \sim 22$ cm/sec, $\alpha \sim 0.40$, $D_0 = 2.5$ cm, and $\rho = 1.05$ gm/cm^3, we find that a typical gradient in pressure is on the order of 0.01 mmHg/cm. Since the full scale range of the pressure transducer was 200 mmHg we would not expect to be able to resolve such a small axial gradient. Fortunately, in the region of partial collapse the local tube law is such that small changes in pressure, that are difficult to detect, result in large changes in area that we are able to measure quite accurately.

Effect of a Constant $\overline{f}$ on Wave Decay. Examination of Eq. (37) shows that even if the axial component of gravity balances the mean frictional force, the presence of an average or constant $\overline{f}$ can affect the solution for $A'(x,t)$, if $\overline{u} \neq 0$. We now simplify the analysis for waves standing in the laboratory frame, eliminating the time-dependence in Eq. (35), and letting the area be:

$$A'(x) = \hat{A}\, e^{-ikx} = \hat{A}\, e^{k_i x}\, e^{-ik_r x} \tag{51}$$

We now seek both the real and imaginary parts of the wave number for the case of standing waves influenced only by the mean skin friction coefficient. This is equivalent to letting $c = 0$ and $\hat{f} = 0$ in Eq. (37). Neglecting the effect of axial bending, this yields:

$$\left[\frac{T D_0 \bar{\alpha}}{4\rho\sqrt{1-\bar{\alpha}}}\right] k^4 + \left[c_\infty^2 - \bar{u}^2\right] k^2 - \left[\frac{6\bar{u}^2\bar{f}}{D_0\bar{\alpha}}\right] ki = 0 \tag{52}$$

Substituting $k = k_r + ik_i$ in Eq. (52), expanding, and setting the real and imaginary parts equal to zero results in two simultaneous equations for k_r and k_i:

$$k_r^3 - 3k_r k_i^2 - \left[\frac{4\rho(\bar{u}^2 - c_\infty^2)}{T\bar{\alpha} D_0}\right] k_r = 0 \tag{53}$$

$$k_i^3 - 3k_r^2 k_i + \left[\frac{4\rho(\bar{u}^2 - c_\infty^2)}{T\bar{\alpha} D_0}\right] k_i + \left[\frac{24\rho\bar{u}^2\bar{f}}{T\bar{\alpha}^2 D_0^2}\right] = 0 \tag{54}$$

By first solving Eq. (53) for k_r in terms of k_i and then substituting for k_r in Eq. (54) we obtain a third order polynomial for k_i (not shown). Since no analytic solution exists for this cubic equation we seek an approximate solution that will be valid only under certain conditions.

From Eq. (45) in the previous chapter, we define the real wave number for the loss-less case as k_0:

$$k_0 \equiv \left.\frac{2\pi}{\lambda}\right|_{f=0} = \sqrt{\frac{4\rho(\bar{u}^2 - c_\infty{}^2)\sqrt{1-\bar{\alpha}}}{T\, D_0\, \bar{\alpha}}} \tag{55}$$

As long as the solution for k_i is such that:

$$27\left(\frac{k_i}{k_0}\right)^2 << 1 \ , \tag{56}$$

Then the solution to the simultaneous equations (53) and (54), accurate to within ± 2% is:

$$k_i \cong \frac{3\bar{f}}{\bar{\alpha}\, D_0}\left(\frac{S^2}{S^2-1}\right) \tag{57}$$

and

$$k_r{}^2 \cong \left(\frac{2\pi}{\lambda}\right)^2 \cong k_0{}^2\left[1 + \frac{3k_i{}^2}{k_0{}^2}\right] . \tag{58}$$

Here, Eq. (57) shows a decay rate that is independent of axial tension, and Eq. (58) reveals that as long as the criteria of Eq. (56) is satisfied, the effect of $\bar{f}$ on the real wavelengths is negligibly small.

Comparison with Experiments. In order to evaluate these results, experimental values for amplitude decay rates were measured for both waves on a constant area (gravity-friction flows), and waves on a slowly increasing area (tension-friction flows). Experimental decay rates were obtained as indicated in Figures 22a and 22b. The semi-log plot usually yielded a reasonably straight line, sufficient for the preliminary study of a rather complex phenomenon.

The decay rates, expressed non-dimensionally in terms of the variable $k_i D_0$, are shown in Figure 23 plotted versus a corresponding average real wave number $(\bar{k}_r D_0) = (2\pi D_0/\bar{\lambda})$. For the gravity-friction flows, the wavelengths vary very little in the axial direction since the area is nearly constant. For the tension-friction flows, the wavelengths grow longer as the mean area increases.

Examination of Figure 23 reveals two important points. First, the experimental decay rates seem to increase consistently with $\bar{k}_r D_0$; and secondly, the corresponding results calculated from Eq. (57) are much too low, particularly for the higher wave numbers (shortest waves). Clearly the observed decay rates cannot be explained on the basis of a constant skin friction coefficient alone.

Consequences of Spatially Oscillatory Skin Friction Coefficient

Modelling of Losses. A number of investigators have studied turbulent flow over wavy surfaces (Benjamin[33], Zilker *et al.*[34]) and through wavy pipes (Hsu and Kennedy[35], Hsu[36]). For a semi-infinite stream moving past a wavy bed, Benjamin[33] predicted an upstream phase shift in the wall shear stress of 30°; that is, the peak in wall shear was displaced upstream from the peak in the wall height.

Hsu and Kennedy[35] found that for flow in sinusoidally wavy-walled pipes the *local* skin friction factor had a sinusoidal character. The magnitudes of the changes in f were greater than would be predicted by the slight change in pipe diameter alone. In addition, they demonstrated

that the degree of the upstream phase shift of the peak in skin friction coefficient increased with increasing amplitude-wavelength ratio. They measured phase shifts of boundary shear stress of 26° and 17.5° corresponding to pipe models with amplitude-wavelength ratios (radius amplitude) of 1/45 and 1/90, respectively.

Our case, that of turbulent flow through standing waves of area and shape, is certainly more complex than either of the two cases mentioned above. By modelling the flow as one-dimensional, however, we cannot hope to accurately represent the influence of non-uniformities in either the velocity or pressure profiles.

The presence of wall curvature leads to distortion of both the velocity profile and the pressure distribution across a cross-section. For example, the velocity profile may become less blunt in a region of expanding area. In a region of positive wall curvature the pressure nearest the wall may be significantly reduced, which may affect the wall deformation in a way not anticipated by the modified tube law. Such distortions of these parameters from their assumed one-dimensional form must affect not only the momentum flux across a cross-section, but also how the wall boundary layer grows and contracts. It is well known that steady-state boundary layers possess a certain "history", so that the wall shear stress is not just a function of local conditions, but is influenced by upstream conditions as well.

Clearly, it may be unrealistic to attempt to represent these complex two-dimensional phenomena by a simple harmonic perturbation in the skin friction coefficient. All of the previously mentioned effects associated

with wall curvature contribute to the total energy loss by influencing both the magnitude and phase of the wall shear stress.

A completely general solution to Eq. (37) involving arbitrary values of m and ϕ is not available at this time, and even if it were available it would be difficult to rationalize a detailed analytical study of its implications. Instead, it may be sufficiently illuminating to assume that due to a combination of all the aforementioned wall curvature effects, the skin friction coefficient has a sinusoidal component that is small in amplitude and 180° out of phase with the area. This phase shift differs by less than 30° from those previously mentioned, and implies that the perturbation in the skin friction coefficient is largest at local minimums in area.

That such a phase shift should represent the worst case, or lead to the greatest decay rates, can be inferred from a simple argument. With a phase shift of 180° the skin friction coefficient is perfectly in phase with the local mean flow velocity and the wall shear stress, by definition, is phase-maximized ($\tau_w \equiv f\left(\frac{1}{2}\rho u^2\right)$).

A convenient form that will yield the desired phase shift is:

$$f = \bar{f} + r\frac{d^2\alpha}{d\xi^2} \tag{59}$$

where r is a positive dimensionless constant. For the form of $f'(x,t)$ given by Eq. (36) this is equivalent to letting $\phi = \pi$, $m = 2$, and $\hat{f} = r\hat{A}/A_0$. For the case of standing waves ($c = 0$), Eq. (37) is again solved for both the real and imaginary parts of the complex wave number. Again, if the

criteria of Eq. (56) is satisfied, the solution for the decay rate, accurate to within ± 2% is:

$$k_i \cong \frac{3\bar{f}}{\bar{\alpha} D_0} \frac{S^2}{(S^2-1)} + \frac{4\rho \bar{u}^2 r \sqrt{1-\bar{\alpha}}}{T \bar{\alpha}} \tag{60}$$

Notice that the first term above is just the decay rate of Eq. (57), due to the effect of the mean component, $\bar{f}$. For future convenience let

$$\left(k_i\right)_{\bar{f}} \equiv \frac{3\bar{f}}{\bar{\alpha} D_0} \frac{S^2}{(S^2-1)} \tag{61}$$

The predicted effect on the real wavelengths is assessed through the relation:

$$k_r^2 = \left(\frac{2\pi}{\lambda}\right)^2 = k_0^2 - k_i^2 \left[1 - \frac{4(k_i)_{\bar{f}}}{k_i}\right] \tag{62}$$

where k_0 is the real inviscid wave number of Eq. (55), and k_i is from Eq. (60). It is evident that since $(k_0/k_i) \approx 10$ there should be little observable effect on the wavelengths predicted by the loss-less analysis. Using Eq. (55) to eliminate the velocity and tension terms in Eq. (60) yields:

$$k_i \cong \frac{1}{D_0}\left(\frac{S^2}{S^2-1}\right)\left[\frac{3\bar{f}}{\bar{\alpha}} + D_0^2 k_0^2 r\right] \tag{63}$$

In this form the consequences of the assumed form for f (Eq. (59)) become clear. The decay rate is increased above the previous result by a term that includes the wave number squared. In order to check whether or

not this result is realistic, some typical experimentally obtained values are used to estimate the value of r.

Sample Calculations. For one run of intermediate axial strain (0.11) and inlet speed index (6.0) a mean wave number of 0.66 cm^{-1} was measured about an area ratio of 0.40. The measured decay rate was 0.076 cm^{-1} with typical peak values of $d^2\alpha/d\xi^2$ of about $\pm$ 0.05, obtained by graphical estimation. These values are typical of the waves encountered experimentally.

Using Eq. (63) with $\overline{f}$ = 0.0077 this yields a value of 0.05 for the coefficient r. The relative magnitude of the fluctuating component of the skin friction coefficient, which by itself can account for the observed decay rate, can now be estimated:

$$\frac{|f'|}{\overline{f}} \approx r \frac{\left(\frac{d^2\alpha}{d\xi^2}\right)_{max}}{\overline{f}} \approx \frac{(.05)(.05)}{(.0077)} \approx 0.32$$

Therefore, a properly phased, small increase in the skin friction coefficient of about 30% may result in a three-fold increase in wave amplitude decay rate. While the assumed form of Eq. (59) is admittedly crude, it has resulted in semi-quantitative agreement with observed decay rates. Both the magnitudes and the wave number dependence of the experimental decay rates appear reasonable in light of this model.

Shock Scaling

The Shock as a Wave. In Chapter III the shock was treated rather simplistically as a diffuser. Assuming that the inlet and exit states are known, one can employ conservation of mass and momentum to place bounds on the pressure recovery possible in the transition. Though the experimental pressure recovery coefficients were well bounded by simple theoretical predictions, little insight into the structure of the shock was obtained. It is therefore desirable to relate in a more causal manner, some geometric shock parameters to shock inlet conditions. Specifically, we seek to relate the maximum area ratio gradient in the shock, $(d\alpha/d\xi)_{max}$, to parameters just upstream at the shock inlet.

Figure 24 illustrates a typical steady supercritical inlet flow. From both the dispersion relation (Eq. (39)) and the radiation condition (Eq. (40)) derived in Chapter V we know that the standing waves exist due to, and are maintained by energy that radiates upstream from the shock. This is experimentally evident in the fact that both the wave amplitude and maximum gradient in area ratio always decay in magnitude in the negative ξ direction, away from the shock. Thus, it is not to postulate a false causality that we seek downstream conditions as a function of upstream conditions; but simply to investigate to what extent the large amplitude shock phenomena can be represented by an analysis of linear waves.

The area ratio versus non-dimensional distance curve of Figure 24 can be approximated mathematically in terms of the complex wave number as:

$$\alpha = \alpha_0 + \left(\frac{d\alpha}{d\xi}\right)\xi + \left(\hat{\alpha}\, e^{k_i D_0 \xi}\right) e^{-ik_r D_0 \xi} \qquad (64)$$

where the term in parentheses represents the envelope of the maximum local amplitude in α about the mean gradient. For convenience let:

$$\hat{\hat{\alpha}} \equiv \left(\hat{\alpha}\, e^{k_i D_0 \xi}\right) \tag{65}$$

as indicated in Figure 24. Differentiating Eq. (64) with respect to ξ leads to, with Eq. (65):

$$\frac{d\alpha}{d\xi} = \left(\overline{\frac{d\alpha}{d\xi}}\right) + \hat{\hat{\alpha}}\left(k_i - i k_r\right) e^{-i k_r D_0 \xi} \tag{66}$$

Taking the maximum real part of Eq. (66) yields:

$$\left[\left(\frac{d\alpha}{d\xi}\right)_{max} - \left(\overline{\frac{d\alpha}{d\xi}}\right)\right] \Big/ \hat{\hat{\alpha}} = D_0 k_r \tag{67}$$

Recalling that the real wavelengths are largely unaffected by viscous effects, we let $k_r \approx k_0$ and substitute for k_0 using Eq. (55), obtaining the following:

$$\frac{\left[\left(\frac{d\alpha}{d\xi}\right)_{max} - \left(\overline{\frac{d\alpha}{d\xi}}\right)\right]}{\hat{\hat{\alpha}}} = \sqrt{\left(S^2-1\right)\left(\frac{\rho c_\infty^2}{E}\right)\left(\frac{D_0}{h}\right)\frac{4\sqrt{1-\bar{\alpha}}}{\bar{\alpha}\,\epsilon_x}} \tag{68}$$

where T has been replaced by $\epsilon_x hE$, and the speed index introduced.

Eq. (68) applies at inflection points of the area trace shown in Figure 24, where the local gradients are maximum. Within the limits of the linearizing assumptions Eq. (68) simply implies that for the small

amplitude waves, local maximum gradients in area ratio can be expressed as a function of local conditions. Eq. (68) can be written in an approximate way to reveal the dependence on the parameters S, ε_x, and α:

$$\left(\frac{d\alpha}{d\xi}\right)_{max} \sim \frac{\hat{\alpha}\, S}{\sqrt{\bar{\alpha}\, \varepsilon_x}} \left[1 - \bar{\alpha}\right]^{1/4} \tag{69}$$

We wish to obtain an expression analogous to Eq. (69) for the shock. In order to justify such an approach we suggest that the shock can be viewed as having two parts; one that is wave-like, and another that is more like a transition zone. The wave-like portion may be considered as that part of the shock that is still highly supercritical, with the area ratio less than 0.80 and the maximum gradient almost constant over the wave-like portion. The transition zone begins near an area ratio of about 0.80 when the gradient in area starts to decrease and the speed index is nearly unity. The transition zone also includes the region in which the area ratio asymptotically approaches unity, and the speed index drops to a typical value of about 0.10.

Shock Scaling Approximations. In order to apply Eq. (68) to the wave-like portion of the shock, it is necessary to make a number of assumptions that will be valid for the majority of shocks observed experimentally. We wish to evaluate Eq. (68) at the inflection point of the shock, α_3 as indicated in Figure 24, in terms of α_1 and S_1, at the inlet to the shock.

First, we can neglect the mean gradient in area ratio relative to the maximum gradient in the shock since:

$$\frac{\left(\frac{d\alpha}{d\xi}\right)}{\left(\frac{d\alpha}{d\xi}\right)_{max}} \approx \frac{0.020}{0.200} \sim 0.1 \ll 1 \tag{70}$$

Secondly, we approximate the local maximum amplitude $\hat{\hat{\alpha}}$ at the shock inflection point as half the value of the final jump in α:

$$\hat{\hat{\alpha}}_3 \approx \frac{(1-\alpha_1)}{2} \tag{71}$$

Thirdly, we estimate the value of α_3 to be midway between the inlet and final area ratios:

$$\alpha_3 \approx \frac{(\alpha_1+\alpha_2)}{2} \approx \frac{(1+\alpha_1)}{2} \tag{72}$$

With these approximations we can express the mean flow velocity u_3 in terms of u_1 and α_1:

$$u_3 = u_1 \frac{\alpha_1}{\alpha_3} \approx u_1 \frac{2\alpha_1}{(1+\alpha_1)} \tag{73}$$

If the speed index at the inflection point is such that $S_3^2 \gg 1$, then:

$$\left(S_3^2 - 1\right) \approx S_3^2 \tag{74}$$

Employing these assumptions; Eqs. (70) -(74), Eq. (68) becomes

$$\left(\frac{d\alpha}{d\xi}\right)_{\substack{max \\ shock}} \approx \left[\frac{S_1^2}{\varepsilon_x} \cdot \frac{8\,\alpha_1^2(1-\alpha_1)^2}{\sqrt{2}(1+\alpha_1)^3} \cdot \frac{\rho c_{\infty_1}^2}{E} \cdot \frac{D_0}{h}\right]^{1/2} \tag{75}$$

If we let $c_{\infty_1} \approx 22$ cm/sec (since the local tube law is reasonably flat in the region $0.30 < \alpha_1 < 0.70$), and replace E and D_0/h by the values 16×10^6 dynes/cm^2 and 29.3 respectively, Eq. (75) becomes:

$$\left(\frac{d\alpha}{d\xi}\right)_{\substack{\max \\ \text{shock}}} \approx 0.073 \frac{S_1}{\sqrt{\epsilon_x}} \frac{\alpha_1(1-\alpha_1)^{5/4}}{(1+\alpha_1)^{3/2}} \qquad (76)$$

Comparison with Experiments. For the tension-friction flows described in Chapter III, the maximum gradients in area ratio were measured graphically. The results are shown in Figure 25 with the prediction of Eq. (76) indicated as a dashed line.

In spite of the many assumptions leading to Eq. (76) the degree of agreement is quite reasonable, indicating that the initial part of a shock-like transition may possess strong wave character. That the linearized approach to shocks is somewhat successful is not entirely surprising, given that such shocks are typically 2.5 to 10 tube diameters long.

CHAPTER VII:

NUMERICAL INTEGRATIONS

Purpose. The scope of the numerical analysis is limited to the type of steady flows obtained experimentally -- those with supercritical inlets and dominated by axial tension and fluid friction. The purpose of the numerical analysis is to generate solutions to the full nonlinear governing equations. From solutions in the form of axial distributions of area ratio and other related parameters qualitative assessment of wave asymmetry or shape is possible, and large amplitude effects can be investigated. The influence of initial conditions on wave amplitude is studied along with a general verification of the results from the linearized analysis.

Governing Equations. There is but one major difference from the preceding analysis, involving the modified tube law. In Chapter IV, the modified tube law was developed in relation to the geometric configuration shown in Fig. 18. We concluded that while the assumed geometric configuration may be appropriate for a tube in a state of partial collapse, it could not be expected to provide much quantitative insight into the nature of shock-like transitions, particularly as $\alpha \to 1.0$.

As evident in Eq. (27), the modified tube law in Chapter IV, the tension term blows up as $\alpha \to 1.0$ due to the presence of the $\sqrt{1-\alpha}$ term in the denominator. This singularity arises from the assumed geometric configuration along with the constraint of constant perimeter. As such the singularity is not physically realistic.

In Chapter VI we speculated that a shock may be considered as having two parts; one that is supercritical and wave-like with large gradients in area that are elliptical in shape, and another that is more like a transition zone that is subcritical with smaller gradients in area as the shape changes from elliptical to circular. We presented experimental evidence that indicates that our simple modified tube law may be a reasonable approximation over the wave-like portion of a shock. However, in relation to the transition zone, both our assumed geometric configuration and all of its consequences are greatly in doubt.

At this stage of the investigation we chose to remove the singularity at $\alpha \to 1.0$ by further simplyfying the modified tube law. Since we have not yet developed a model for the transition zone that is fundamentally sound, it would be false rigor to postulate modifications of increasing complexity without increased understanding. Hopefully, in the future, this gap in our model will be filled.

Eliminating the $\sqrt{1-\alpha}$ term, Eq. (27) becomes

$$(p-p_e) = K_p P(\alpha) - \frac{T}{2\pi R_0} \frac{d^2A}{dx^2} \tag{77}$$

For steady flow, continuity is simply:

$$uA = u_0A_0 = Q = \text{constant} \tag{78}$$

or $u = u_0/\alpha$. Substitution of the tube law of Eq. (77) into the momentum equation (Eq. (29)) and letting $\frac{\partial}{\partial t} = 0$ yields, after simplification and non-dimensionalization:

$$\frac{d^3\alpha}{d\xi^3} = \frac{4\rho u_0^2 D_0}{T\alpha^3}\left[\left(\frac{1}{S^2} - 1\right)\frac{d\alpha}{d\xi} + 2f\right] + \frac{4D_0}{T}\left[\frac{dP_e}{d\xi} + \rho g \frac{dz}{d\xi}\right] \tag{79}$$

For the purposes of this thesis the two terms representing gradients in external pressure and elevation shall be set to zero, leaving just:

$$\frac{d^3\alpha}{d\xi^3} = \frac{4\rho u_0^2 D_0}{T\alpha^3}\left[\left(\frac{1}{S^2} - 1\right)\frac{d\alpha}{d\xi} + 2f\right] \tag{80}$$

Numerical Technique. Equation (80) can be represented by a system of three simultaneous first order, ordinary nonlinear differential equations. A standard fourth order Runge-Kutta routine is used to integrate the system of equations (Hornbeck[37]). The problem is therefore treated as an initial value problem, with the solution resulting from a step-wise integration of the system equations.

Brower[28] used a similar integration scheme in attempting to predict area distributions and pressure-flow characteristics for the case of sub-critical inlets. For such cases there are no waves or shocks in steady flow. Instead, near the downstream rigid attachment, a flow-limiting throat will often form, with very large derivatives in area accompanying the rapid expansion to the rigid tube. In order to satisfy all boundary conditions Brower found it necessary to develop a very complex and time-consuming iterative technique, including the influence of flow-loading (Eq. (24)) on axial strain. In view of the simplicity of our model, no attempt is made to rigorously satisfy all boundary conditions.

Instead, the governing equations are integrated forwards or backwards, depending on the region of interest -- waves or shocks, respectively. The Runge-Kutta scheme requires initial conditions for α, $d\alpha/d\xi$ and $d^2\alpha/d\xi^2$, as well as speed index. The spatial step size found to yield satisfactory results is 1/40 of a diameter (approximately 0.6 mm)

Results of Forward Integration-Waves

Constant Skin Friction Coefficient. Figures 26 and 27 illustrate the effect of initial conditions on waves that are superimposed on a mean gradient in area. The initial conditions for the curves of Figure 26 are $\alpha_0 = 0.275$, $S_0 = 10.0$, $\varepsilon_x = 0.10$, $(d^2\alpha/d\xi^2)_0 = 0$, and three values of $(d\alpha/d\xi)_0 = 0.03, 0.075, 0.135$. It is evident, qualitatively, that the wave amplitude increases with increasing initial gradient; and that until the amplitudes get very large, the wavelengths all coincide. As shown in Figure 26, as the amplitudes become larger the wavelengths become slightly larger. The same behavior can be seen in Figure 27 for the case of smaller axial strain and slightly greater initial gradients in α.

As mentioned earlier, no attempt was made to satisfy all natural boundary conditions. The wave growth shown in Figure 26 eventually leads to unrealistically large values of α. Even if the model was complete, it is likely that only a small number of specific sets of initial conditions would result in a meaningful final or downstream area. This type of behavior limits the usefulness of the numerical technique.

From the solutions shown in Figures 26 and 27 (as well as others not shown) several results of the linearized analysis can be verified. Recall

the manner in which the validity of the inviscid dispersion relation was investigated experimentally in Chapter V. For tension-friction flows experimental peak-to-peak and trough-to-trough wavelengths were measured along with corresponding values for mean area ratio and flow velocity. The experimental waves were not purely sinusoidal, nor were their amplitudes symmetric about the mean gradient in area. In order to assess the possible influence of this approximate measurement technique, numerically obtained distributions of area were analyzed in the same way as the previous experimental results. These results, compared with the inviscid dispersion relation of Eq. (45), with the $\sqrt{1-\alpha}$ term omitted, are shown plotted in Figure 28 in a manner similar to that of Figure 19. From the agreement evident in Figure 28 we can conclude that the measurement technique for estimating the wavelengths of standing waves is quite reasonable, even in the presence of a mean gradient in area.

Growth rates (or equivalently, decay rates in the negative ξ direction) for the wave trains shown in Figures 26 and 27 compare well with the small amplitude result of Eq. (57). (Note that for the case of constant skin friction coefficient the growth rate is independent of axial tension.) For very small amplitude waves (not shown) the comparison is quite good, within ± 2%. Only when the amplitudes $\hat{\alpha}$ are large; $\hat{\alpha} > 0.10$ does the linearized result begin to fail. The linear solution begins to yield inaccurate results not only for large amplitude waves, when nonlinear effects become important, but for any flow in which the speed index approaches unity. This can be seen from the expression of Eq. (57) which predicts infinite wave growth in the + x direction as $S \rightarrow 1.0$.

It is this tendancy toward singular behavior as $S \to 1.0$ that in part prevents us from obtaining meaningful numerical integrations that include both the standing waves and the shock. Even with the $\sqrt{1-\alpha}$ omitted, the solution is most unstable as $S \to 1.0$. Though the effect of axial tension is to allow continuous transitions from sub- to supercritical flow, it is in the region of $S = 1.0$ that the assumed model for axial tension will have its greatest influence. Unfortunately, it is also in this region where our model is admittedly a poor approximation.

Fluctuating Skin Friction Coefficient. Figures 29 and 30 show the effect of a fluctuating component in the skin friction coefficient. The form is that of the phase-maximized worst case (Equation (59)) discussed in Chapter VI. Figure 29 corresponds to Figure 26 (same I.C.'s) with $(d\alpha/d\xi)_0 = 0.03$ and $r = 0.03$. Similarly, Figure 30 corresponds to Figure 27 with $(d\alpha/d\xi)_0 = 0.03$ and $r = 0.01$.

For these two figures the decay rates were measured about the mean gradient line and compared to the result of Eq. (63). For the first three or four waves, while the peaks and troughs are still symmetric about the mean gradient line, the amplitudes of the peaks decay at a rate 10% larger than the linearized result, while the troughs decay at a rate about 10% less than the linearized result. As the waves increase in amplitude in the flow direction they become less symmetrically disposed about the mean gradient line. Consequently, it is difficult to estimate amplitudes in a consistent, meaningful way. Numerical analysis of cases in which there is no mean gradient and the amplitudes are smaller confirms that Eq. (63) is a correct linear approximation for very small amplitudes.

The results shown in Figures 29 and 30 represent the consequences of rather arbitrarily chosen initial conditions and values of the coefficient r. They are intended primarily to show the degree of departure from the results of Figures 26 and 27 due to the added component of the skin friction ccefficient. It is apparent that the waves of the latter figures are more asymmetric than before, while still quite sinusoidal in nature.

Backwards Integrations: Shock-Like Transitions

Equation (75) can also be integrated backwards simply by using a negative spatial step and choosing appropriate initial conditions. The preceding results of forward integrations have shown that it is difficult to choose initial conditions at a point where standing waves exist. Though the shock is a structure that is poorly understood, the initial conditions downstream of a shock are easily estimated. Experimental results show that all derivatives of α are small and the speed index is typically on the order of 0.10.

Figures 31 and 32 show the results of backward integrations for initial conditions of $\alpha_0 = 1.0$, $(d\alpha/d\xi)_0 = (d^2\alpha/d\xi^2)_0 = 0.0$, $S_0 = 0.15$. These two figures represent essentially the same parameters as the results of Figures 29 and 30 respectively, except that the initial conditions are different. These results are not intended to match experimental results in detail, though the wavelengths and decay rate can be simulated with reasonable accuracy. Until a better model of the shock is available there is no point in pursuing the numerical integrations beyond the present level.

Other difficulties arise when numerically integrating Eq. (80) for the case of subcritical flow $S < 1$, $\alpha \geq 1.0$. Such is the case when integrating downstream from a shock. Experimental results indicate that the effect of axial tension becomes small relative to that of the local tube law when the tube is nearly inflated. As a consequence, the term of highest order is based on a physical effect that is vanishing, and the numerical integrations become unstable. Future work may involve making a smooth transition from a third order system to one of first order and perhaps back again.

CHAPTER VIII:

SUMMARY AND CONCLUSIONS

The primary motivation for this work stems from the belief that collapsible tube flows are important in many areas of human physiology and in connection with several medical devices. Until the very recent past most of the research on flow in collapsible tubes focussed on so-called "Starling resistors" -- a conceptual trap that led investigations to view collapsible tubes as three-port "black-box" devices with intriguing pressure-flow characteristics.

The thrust of this thesis research has not been directed toward any specific application, but rather to improve our fundamental understanding of collapsible tube flows. In particular, some phenomena associated with steady supercritical flow have been addressed experimentally, analytically, and numerically. The emphasis has been on performing accurate experiments on flow in thin-walled latex tubes, and developing a theoretical model that couples one-dimensional flow mechanics with a simple tube law that incorporates the effect of axial tension.

Experimental

The first phase of the investigation resulted in the development of an electrical impedance technique for accurate shape-independent area measurement. Using the impedance technique, the local tube law or pressure-area relation for uniform collapse, was determined and shown to be in good agreement with existing theoretical predictions for both extreme two-

lobed collapse and positive pressure inflation. From smoothed P-α data the phase velocity for long wavelength, small amplitude waves, c_∞, was derived as a function of area ratio α. Once the tube had been characterized by the local tube law, it was possible to infer from the measurement of flow rate and area such parameters as mean fluid velocity, $u = Q/A$, and speed index, $S = u/c_\infty$.

Experiments were performed on two classes of steady, supercritical inlet flows; gravity-friction flows, and tension-friction flows. The gravity-friction flows were performed primarily to qualitatively demonstrate that supercritical flow is a necessary but not sufficient condition for either standing waves of area or shock-like transitions. The tension-friction flows incorporated a moderate range of inlet speed indexes and axial strains to achieve a variety of standing wave structures upstream of shock-like transitions. Both qualitative and quantitative observations of the steady flow experiments were used in the subsequent development of a theoretical model of the combined fluid and structural mechanics.

Theoretical

The fluid equations, continuity and momentum, were derived in general form, including time-dependent terms. The flow was treated as one-dimensional with pressure and velocity assumed to be uniform across the cross-section. Losses were modelled in terms of a skin friction coefficient that related wall shear stress to the mean fluid velocity. The flow was assumed to be turbulent and fully developed. The effects of gradients in external pressure and elevation were also included.

A simplified model for the geometry of a partially collapsed tube was adopted that represented the actual quasi-elliptical cross-sectional shape as two parallel sections joined at the sides by half circles. The effect of axial tension in combination with axial curvature of the flat sections then gives rise to a transmural pressure difference similar to the way in which surface tension and surface curvature combine to produce an interfacial pressure difference. The effect of axial bending was included in an analogous way by considering only the bending of the flat sections. A modified tube law was then postulated, assuming that the actual transmural pressure is the result of superimposing the local tube law, and incremental transmural pressures due to axial tension and bending. Time-dependent terms were neglected and the entire structural mechanics of the tube represented in terms of a transmural pressure that depended not only on the area, but on spatial derivatives of the area, as well as the geometric and structural properties of the tube.

Linear Analysis - Inviscid

The governing equations were linearized for small perturbations in area, fluid velocity, and skin friction coefficient about constant mean values, primarily to investigate wave propagation phenomena. The perturbation in area was assumed to have the form of a complex exponential representing a travelling wave of unknown phase velocity and complex wave number. For the case of waves propagating into a stagnant fluid, without viscous losses, the inviscid dispersion relation or $c(\lambda)$ was derived, including the effects of both axial tension and bending. From the dispersion relation

the group velocity c_g, at which energy propagates, was shown to always exceed the phase velocity of the dispersive waves. The standing wave structures observed experimentally were discussed in terms of the dispersion relation and the group velocity. In addition, the dispersion relation was used to establish a criteria for the conditions under which the influence of axial bending can be neglected relative to that of axial tension. It was then shown that for all the tension-friction flows, the effect of axial bending was relatively small.

Experimental results from the tension-friction flows were compared to the inviscid dispersion relation. The wavelengths measured experimentally compared very favorably with those predicted by the linearized analysis -- indicating that the approximate model for representing the effect of axial tension was quite acceptable. In addition, the effect of a mean gradient in area, a consequence of viscous losses, was shown to be small.

Linear Analysis - Viscous

The consequences of the dominant viscous effect; those arising from a constant skin friction coefficient based on fully developed turbulent flow, were examined for both gravity-friction and tension-friction flows. When the axial component of gravity just balanced the frictional force constant-area supercritical flow was achieved. Experimental asymptotic areas were measured and used to calculate effective experimental skin friction coefficients. Comparison with the Blasius relation showed the experimental results to be higher. This may indicate that under the circumstances of no standing waves the flow was not fully developed, or that there was a small shape effect.

Mean gradients in area for the tension-friction flows were also measured and used to calculate effective experimental skin friction coefficients. Comparison with the Blasius relation showed the experimental results to be in relatively good agreement. Though the measurement of the mean gradients was not precise, and the range of gradients small, the average skin friction coefficients through the waves were only slightly greater than the predicted values. In this case the gradients had a much smaller effect than might be anticipated.

A preliminary study of wave amplitude decay was also performed. For the gravity-friction flows the amplitudes of the waves were observed to decay away from the shocks in the upstream direction; the wave amplitudes appearing somewhat symmetric about a constant mean area. For the tension-friction flows the same was generally true, except that the wave amplitudes were less symmetric about a constant gradient in area. Assuming a simple exponential-type decay, a single decay rate was measured for each group of standing waves. From qualitative observation that the shorter waves appeared to decay more rapidly than the longer waves, it seemed appropriate to plot experimental decay rates versus mean real wave number.

The influence of a constant mean skin friction coefficient on wave decay was found by solving the linearized equations for the case of stationary waves and finding an expression for the complex part of the wave number -- the decay rate. The resulting relation revealed no dependence on axial tension or wave number, as well as predicting decay rates that were much too small compared to the experimental values.

Clearly, some other explanation was required for the large decay rates observed experimentally. A review of the literature on turbulent flow over wavy surfaces revealed that it is possible for the local skin friction coefficient to have a sinusoidal character -- even though the mean may be close to that based on the mean geometry. The sinusoidal behavior observed by previous investigations has been discussed as resulting from a complex combination of several effects; including two-dimensional phenomena such as changes in the velocity profile, distortion of the pressure distribution across a cross-section, and shear history effects in the wall boundary layer. Basically, the observed skin friction coefficients of others were sinusoidal and phase-shifted approximately 30° upstream from local minimums in area.

A worst-case form for a sinusoidal perturbation in the skin friction coefficient was postulated by letting the perturbation be in phase with the fluid velocity, or 180° out of phase with the area. Subsequent solution of the linearized equations yielded an expression for the decay rate that had an additional term with a dependency on the wave number squared. In addition, comparison with experiments indicated that a relatively small perturbation in the skin friction coefficient could yield a three-fold increase in decay rate, without significantly affecting the wavelengths. Since an essentially two-dimensional phenomena was incorporated rather crudely into a one-dimensional model, more direct comparison with experimental results was not pursued.

Shock-Like Transitions

For the steady supercritical inlet flows achieved with finite axial strain a transition from sub- to supercritical flow always occurred over some portion of the tube. That portion with a positive gradient in area, extending from a local minimum in area (where flow was supercritical) to a local maximum or plateau in area (where flow was subcritical) was defined as the shock. As such, shocks were investigated in two ways -- as diffusers, and as part of the standing wave system.

As diffusers, the shocks were shown to exhibit pressure recovery coefficients that were well bounded by simple theoretical limits. Comparison with two-dimensional straight-walled diffusers indicated that even the steepest shocks had approximate open angles that were much too small to result in either full stall or jet flow. Qualitative observations on the degree of unsteadiness coupled with the actual values of pressure recovery coefficients indicated that the steepest shocks were operating at worst in the region of transitory stall. Many shocks were gradual enough to allow wall shear to dominate over expansion-entrainment type losses, exhibiting very little unsteadiness.

Though the shock transition is typically the most abrupt, large-amplitude change in area observed, shock lengths ranged from approximately 2.5 to 10 tube diameters, making the shock appear more like a wave than a discontinuity. Consequently, an effort was made to relate the maximum gradient in the shock to shock inlet conditions (area ratio, speed index, axial strain) by applying the linearized wave analysis to the shock. Though physical causality is certainly not purely in the downstream direction,

the analysis was made in order to gain some insight into the scaling of the shock parameters.

A simple relation was derived that showed the maximum gradient in area ratio directly proportional to the inlet speed index and inversely proportional to the square root of the axial strain. Comparison with experimental shocks revealed good semi-quantitative agreement, indicating that the supercritical part of a shock-like transition may reasonably be described as a truncated wave.

Numerical Integrations

The scope of the numerical analysis was limited to the type of steady supercritical flows observed experimentally -- those in which axial tension and fluid friction are dominant. The term in the axial tension model that results in a singularity when the area ratio equals one was set to unity and the effect of axial bending neglected. The resulting third order nonlinear ordinary differential equation was evaluated using a fourth order Runge-Kutta technique. Solutions were generated in the form of axial distributions of area ratio, speed index, and other related parameters, largely to confirm the previous solutions to the linearized equations through small amplitude numerical "experiments". For this purpose it was not necessary to satisfy all natural boundary conditions, but only to choose reasonable initial conditions for the self-starting Runge-Kutta routine.

Using forward integration, the inviscid dispersion relation, plus the various expressions for wave amplitude decay were confirmed in the limit of small amplitudes. The solutions to the linearized equations

were also shown to be quite valid for all but the largest amplitude waves observed experimentally. By integrating backwards, as from downstream of a shock, qualitative agreement with the experimentally observed shock/wave systems was demonstrated.

In conclusion, the numerical analysis confirmed the accuracy of the previously derived solutions to the linearized equations while providing little additional insight. It is recommended that in future studies the linearized approach be used unless the phenomena is large-amplitude in nature, well-defined, and of sufficient importance to warrant the greatly increased effort.

Conclusions

The following conclusions pertain to steady flows with supercritical inlets:

(i) There is a mean area increase with distance that is due to friction, and is substantially independent of wave phenomena associated with axial tension. The mean gradient in area agrees with the simple one-dimensional theory.

(ii) If there is a suitable disturbance, standing waves of area associated with axial tension appear, superimposed on the mean area increase.

(iii) The wavelengths of the standing waves are in agreement with the inviscid dispersion relation, which was arrived at by a linearized small amplitude theory and the use of

a simple approximate model for estimating how the local p-A relationship is affected by axial tension.

(iv) The dispersion relation reveals that the phase velocity increases with decreasing wavelength, and as a consequence, the group velocity always exceeds the phase velocity. Hence, in a supercritical flow energy can propagate upstream from a disturbance and allow waves to become stationary at a location where the mean fluid velocity equals the local finite wavelength phase velocity.

(v) The amplitudes of the standing waves decay in the upstream direction. The rate of decay cannot be explained on the basis of the simple one-dimensional theory, but requires a perturbation component in the skin friction coefficient that is substantially out of phase with the area.

(vi) If the downstream pressure is sufficiently high, a stationary shock-like transition appears which changes the flow from a supercritical partially collapsed state to a subcritical inflated state. The stationary shock serves as the disturbance from which the stationary waves radiate upstream.

(vii) Characterized as diffusers, stationary shock-like transitions exhibit pressure recovery coefficients that are less than the maximum predicted for a loss-less expansion, and greater than the minimum that would result from an abrupt Carnot-Borda expansion.

(viii) The shock thickness, as characterized by the maximum area gradient in the shock, is in agreement with an analysis that treats the upstream, supercritical part of the shock as part of the train of standing waves.

REFERENCES

1. Shapiro, A. H., "Physiologic and Medical Aspects of Flow in Collapsible Tubes", *Proceedings of the Sixth Canadian Congress of Applied Mechanics,* pp. 883-906, 1977.
2. Weber, W., "Theorie der durch Wasser oder andere Incompressible Flussigkeiten in Elastischen Rohren Fortgepflanzten Wellen" *Verh. Koenigl. Saechs. Ges. Wiss 18:* 353, 1866, Leipzig.
3. Griffiths, D. J., "Urethral Elasticity and Micturition Hydrodynamics in Females", *Med. & Biol. Eng. 7:* 201-215, 1969.
4. Griffiths, D. J., "Hydrodynamics of Male Micturition -- I: Theory and Steady Flow Through Elastic-Walled Tubes", *Med. & Biol. Eng. 9:* 581-588, 1971.
5. Griffiths, D. J., "Steady Fluid Flow Through Veins and Collapsible Tubes," *Med. & Biol. Eng. 9:* 597-602, 1971.
6. Griffiths, D. J., "The Mechanics of the Urethra and of Micturition", *British J. of Urology 45:* 497-507, 1973.
7. Oates, G. C., "Fluid Flow in Soft-Walled Tubes; Part 1: Steady Flow", *Med. & Biol. Eng. 13:* 773-778, 1975.
8. Shapiro, A. H., "Steady Flow in Collapsible Tubes", *Trans. ASME, J. Biomech. Eng. 99:* 126-147, 1977.
9. Olsen, J. H., and Shapiro, A. H., "Large-Amplitude Unsteady Flow in Liquid-Filled Elastic Tubes", *J. Fluid Mech. 29:* 513-538, 1977.
10. Kamm, R. D., and Shapiro, A. H., "Unsteady Flow in a Collapsible Tube Subjected to External Pressure or Body Forces", *J. Fluid Mech., Pt. 1, 95:* 1-78, 1979.

11. Lambert, J. W., "On the Nonlinearities of Fluid Flow in Non-Rigid Tubes", *J. Franklin Inst. 266:* 83-102, 1958.

12. Beam, R. M., "Finite-Amplitude Waves in Fluid-Filled Elastic Tubes: Wave Distortion, Shock Waves, and Korotkoff Sounds", *NASA Tech. Note* TN D-4803, 1968.

13. Rudinger, G., "Shock Waves in Mathematical Models of the Aorta", *J. Appl. Mech. 37:* 34-37, 1970.

14. Anliker, M., Rockwell, R. L., and Ogden, E., "Nonlinear Analysis of Flow Pulses and Shock Waves in Arteries, I, II. *ZAMP 22:* 217-246, 563-581, 1971.

15. Kivity, Y., and Collins, R., "Nonlinear Wave Propagation in Visco-elastic Tubes: Application to Aortic Rupture", *J. Biomechanics 7:* 67-76, 1974.

16. Kececioglu, I., Kamm, R. D., and Shapiro, A. H., "Structure of Shock Waves in Collapsible-Tube Flow", *Proceedings of the 31st Annual Conference on Engineering in Medicine and Biology,* p. 92, 1978.

17. Kececioglu, Ifiyenia, "Experimental Determination of the Structure of Shock Waves in Fluid Flow through Collapsible Tubes with Application to the Design of a Flow Regulator", Thesis for the Degree of Mechanical Engineer, M.I.T., 1979.

18. Elliot, E. A., and Dawson, S. V., "Fluid Velocity Greater than Wave-speed and the Transition from Supercritical to Subcritical Flow in Elastic Tubes", *Med. & Biol. Eng. 17:* 192-198, 1979.

19. Weaver, D. S., and Paidoussis, "On Collapse and Flutter Phenomena in Thin Tubes Conveying Fluid", *J. Sound & Vibration 50:* 117-132, 1977.

20. Matsuzaki, Y., and Fung, Y. C., "Stability Analysis of Straight and Buckled Two-Dimensional Channels Conveying an Incompressible Flow", *J. Appl. Mechanics 44:* 548-552, 1977.

21. Raman, K. R., "Experimental Study of the Mechanical Behavior of a Flexible Fluid-Filled Tube Simulating Arteries", Engineer's Thesis, Dept. Aero & Astro., Stanford University, 1964.

22. Flaherty, J. E., Keller, J. B., and Rubinow, S. I., "Post-Buckling Behavior of Elastic Tubes and Rings with Opposite Sides in Contact", SIAM, *J. Appl. Math. 24:* 446-455, 1972.

23. Tadbakhsh, I., and Odeh, F., "Equilibrium States of Elastic Rings", *J. Math. Anal. & Appl. 18:* 59-74, 1967.

24. Treloar, L. R.G., *The Physics of Rubber Elasticity,* Clarendon Press, 1958.

25. Miller, Donald S., *Internal Flow: A Guide to Losses in Pipe and Duct Systems,* Cranfield, British Hydromechanics Research Association, 1971.

26. Johnston, J. P., "Internal Flows", Chapter 3 in *Topics in Applied Physics, Vol. 12: Turbulence,* Ed. P. Bradshaw, pp. 139-144, Springer-Verlag, New York, 1978.

27. Kamm, R. D., "A Study of External Pneumatic Compression for the Prevention of Deep Venous Thrombosis", Ph.D. Thesis, Department of Mechanical Engineering, M.I.T., May, 1977.

28. Brower, R. W., "Pressure-Flow Characteristics of Collapsible Tubes", Ph.D. Thesis, Department of Biomedical Engineering, University of Pennsylvania, 1970.

29. Swidler, S. C., "Effect of Longitudinal Tension and Curvature on Pressure-Area Relationships of Collapsible Tubes", S.M. Thesis, Department of Mechanical Engineering, M.I.T., 1979.

30. Hus, S., and Kennedy, J. F., "Turbulent Flow in Wavy Pipes", *J. Fluid Mech. 47:* 481-502, 1971.

31. Whitham, G. B., *Linear and Nonlinear Waves,* John Wiley & Sons, New York, 1974.

32. Schlichting, Hermann, *Boundary-Layer Theory,* 6th edition, McGraw-Hill, New York, 1968.

33. Benjamin, K. B., "Shearing Flow Over a Wavy Boundary", *J. Fluid Mech. 6:* 161-205, 1959.

34. Zilker, D. P., Cook, G. W., and Hanratty, T. J., "Influence of the Amplitude of a Solid Wavy Wall on a Turbulent Flow. Part 1: Non-Separated Flows", *J. Fluid Mech. 82:* 29-51, 1977.

35. Hsu, S., and Kennedy, J. F., "Turbulent Flow in Wavy Pipes", *J. Fluid Mech. 47:* 481-502, 1971.

36. Hsu, Sheng-Tien, "Turbulent Flow in Wavy Pipes", Ph.D. Thesis, Department of Hydraulic Engineering, University of Iowa, 1968.

37. Hornbeck, R. W., *Numerical Methods,* Quantum, New York, 1975, p. 195.

TABLE 1

Tabulated Tube Law

α	P	c_∞ cm/sec	α	P	c_∞ cm/sec
0.2000	-11.180	71.40	0.3400	-5.304	21.67
0.2025	-10.870	78.00	0.3450	-5.281	21.77
0.2050	-10.600	80.15	0.3500	-5.259	21.87
0.2075	-10.340	81.50	0.3550	-5.236	21.98
0.2100	-10.070	82.40	0.3600	-5.212	22.09
0.2125	-9.800	83.10	0.3650	-5.190	22.19
0.2150	-9.540	83.65	0.3700	-5.168	22.30
0.2175	-9.270	84.10	0.3750	-5.144	22.40
0.2200	-9.000	84.46	0.3800	-5.120	22.50
0.2225	-8.740	84.73	0.3850	-5.098	22.61
0.2250	-8.480	84.95	0.3900	-5.075	22.71
0.2275	-8.220	85.10	0.3950	-5.050	22.81
0.2300	-7.950	85.27	0.4000	-5.029	22.87
0.2325	-7.700	85.25	0.4050	-5.005	22.94
0.2350	-7.440	85.20	0.4100	-4.983	23.00
0.2375	-7.180	85.00	0.4150	-4.961	23.06
0.2400	-6.940	84.56	0.4200	-4.940	23.13
0.2425	-6.690	83.25	0.4250	-4.918	23.18
0.2450	-6.470	81.00	0.4300	-4.898	23.24
0.2475	-6.250	76.60	0.4350	-4.878	23.29
0.2500	-6.080	67.50	0.4400	-4.857	23.34
0.2525	-5.950	59.40	0.4450	-4.836	23.39
0.2550	-5.850	48.25	0.4500	-4.817	23.44
0.2575	-5.800	37.12	0.4550	-4.798	23.48
0.2600	-5.762	32.30	0.4600	-4.777	23.52
0.2625	-5.734	28.81	0.4650	-4.758	23.57
0.2650	-5.710	27.22	0.4700	-4.738	23.61
0.2675	-5.688	25.51	0.4750	-4.719	23.65
0.2700	-5.670	24.20	0.4800	-4.700	23.69
0.2750	-5.635	22.95	0.4850	-4.681	23.73
0.2800	-5.607	22.55	0.4900	-4.662	23.77
0.2850	-5.579	22.25	0.4950	-4.643	23.81
0.2900	-5.551	22.02	0.5000	-4.625	23.85
0.2950	-5.523	21.85	0.5050	-4.607	23.88
0.3000	-5.497	21.72	0.5100	-4.589	23.91
0.3050	-5.470	21.63	0.5150	-4.570	23.94
0.3100	-5.446	21.57	0.5200	-4.550	23.97
0.3150	-5.421	21.54	0.5250	-4.532	24.01
0.3200	-5.398	21.53	0.5300	-4.514	24.04
0.3250	-5.374	21.54	0.5350	-4.496	24.07
0.3300	-5.350	21.56	0.5400	-4.478	24.10
0.3350	-5.329	21.61	0.5450	-4.460	24.12

TABLE 1 (continued)

α	P	c_∞ cm/sec	α	P	c_∞ cm/sec
0.5500	-4.444	24.15	0.7600	-3.800	25.56
0.5550	-4.426	24.17	0.7650	-3.786	25.70
0.5600	-4.409	24.20	0.7700	-3.770	25.85
0.5650	-4.390	24.24	0.7750	-3.758	26.02
0.5700	-4.373	24.27	0.7800	-3.742	26.20
0.5750	-4.356	24.29	0.7850	-3.728	26.39
0.5800	-4.338	24.31	0.7900	-3.712	26.60
0.5850	-4.320	24.33	0.7950	-3.698	26.82
0.5900	-4.304	24.35	0.8000	-3.682	27.05
0.5950	-4.288	24.37	0.8050	-3.669	27.30
0.6000	-4.270	24.38	0.8100	-3.653	27.56
0.6050	-4.254	24.40	0.8150	-3.638	27.85
0.6100	-4.239	24.41	0.8200	-3.621	28.16
0.6150	-4.221	24.42	0.8250	-3.606	28.48
0.6200	-4.207	24.43	0.8300	-3.590	28.84
0.6250	-4.191	24.45	0.8350	-3.572	29.21
0.6300	-4.176	24.46	0.8400	-3.555	29.58
0.6350	-4.160	24.47	0.8450	-3.540	30.00
0.6400	-4.142	24.49	0.8500	-3.521	30.41
0.6450	-4.129	24.50	0.8550	-3.503	30.86
0.6500	-4.113	24.52	0.8600	-3.485	31.33
0.6550	-4.097	24.54	0.8650	-3.466	31.85
0.6600	-4.080	24.56	0.8700	-3.445	32.35
0.6650	-4.065	24.58	0.8750	-3.424	32.89
0.6700	-4.049	24.60	0.8800	-3.402	33.45
0.6750	-4.033	24.63	0.8850	-3.380	34.04
0.6800	-4.019	24.65	0.8900	-3.360	34.65
0.6850	-4.004	24.67	0.8950	-3.337	35.30
0.6900	-3.989	24.70	0.9000	-3.313	36.00
0.6950	-3.975	24.73	0.9050	-3.288	36.70
0.7000	-3.961	24.76	0.9100	-3.262	37.47
0.7050	-3.948	24.80	0.9150	-3.236	38.32
0.7100	-3.934	24.83	0.9200	-3.208	39.24
0.7150	-3.920	24.86	0.9250	-3.179	40.25
0.7200	-3.908	24.91	0.9300	-3.149	41.50
0.7250	-3.895	24.96	0.9350	-3.118	43.00
0.7300	-3.880	25.01	0.9400	-3.082	45.05
0.7350	-3.869	25.07	0.9450	-3.047	47.03
0.7400	-3.855	25.15	0.9500	-3.005	49.84
0.7450	-3.842	25.23	0.9550	-2.961	51.96
0.7500	-3.829	25.32	0.9600	-2.912	55.62
0.7550	-3.814	25.43	0.9650	-2.855	59.82

TABLE 1 (continued)

α	P	c_∞ cm/sec
0.9700	-2.790	64.25
0.9750	-2.715	74.00
0.9800	-2.616	89.50
0.9850	-2.465	113.50
0.9875	-2.345	132.00
0.9896	-2.174	149.00
0.9900	-2.000	154.00
0.9930	-1.880	190.00
0.9940	-1.780	208.00
0.9950	-1.650	228.00
0.9960	-1.450	256.00
0.9970	-1.200	296.00
0.9980	-0.088	346.00
0.9990	-0.045	390.00
1.0000	0.0	436.00
1.0010	0.072	490.00
1.0020	1.570	534.00
1.0030	2.550	568.00
1.0040	3.650	595.00
1.0050	4.850	616.00
1.0060	6.200	637.00
1.0070	7.550	655.00
1.0080	8.950	671.00
1.0090	10.340	685.00
1.0100	11.750	697.00
1.0110	13.180	708.00
1.0120	14.510	718.70

$$\alpha \leq .20 \begin{cases} P = -\alpha^{-3/2} \\ c_\infty = \sqrt{\frac{3}{4}\frac{K_p}{\rho}} \cdot \alpha^{-3/4} \end{cases}$$

$$\alpha \geq 1.012 \begin{cases} P = \beta(1-\alpha^{-2}) - 6.0 \\ c_\infty = \sqrt{\frac{2K_p\beta}{\rho}} \cdot \alpha^{-1} \end{cases}$$

K_p = 304 dynes/cm^2

β = 870 dynes/cm^2

A_0 = 4.985 cm^2

h = 0.086 cm

TABLE 2

Summary of Experimental Results

Run	ε_x	α_0	S_0	α_1	S_1	$\left(\frac{d\alpha}{d\xi}\right)_{max}$	C_p	R_e
1	.023	.270	8.00	.435	5.05	.356	.605	10,630
2		.270	8.00	.583	3.70	.209	.489	10,630
3		.270	8.00	.352	6.70	.378	.554	10,630
4		.270	8.00	.315	7.60	.398	.568	10,630
5		.261	4.60	.640	2.41	.090	.425	7,920
7		.261	4.60	.472	3.42	.231	.607	7,920
8		.261	4.60	.382	4.45	.332	.688	7,920
9		.261	4.60	.315	5.70	.302	.626	7,920
10		.252	1.73	.475	2.30	.114	.476	5,280
11		.248	1.30	.462	2.30	.120	--	5,280
12		.248	1.30	.323	3.70	.212	.628	5,280
13		.248	0.95	.308	2.70	.148	.708	3,700
14		.453	4.80	.558	3.80	.311	.588	10,630
15		.453	4.80	.538	3.90	.251	.550	10,630
16		.453	4.80	.627	3.30	.197	.414	10,630
17		.453	4.80	.475	4.60	.290	.555	10,630
18		.453	4.80	.440	5.00	.318	.564	10,630
19		.440	3.70	.530	3.00	.155	.460	7,920
20		.440	3.70	.435	3.80	.237	.545	7,920
21		.440	2.45	.417	2.70	.171	.662	5,280

TABLE 2 (continued)

Run	ε_x	α_0	S_0	α_1	S_1	$\left(\frac{d\alpha}{d\xi}\right)_{max}$	C_p	R_e
22	.023	.440	2.48	.422	2.60	.166	--	5,280
23	.046	.269	8.16	.489	4.50	.157	.584	10,680
24		.272	8.29	.377	6.20	.245	.590	10,680
25		.269	7.88	.299	8.10	.322	.621	10,680
26		.269	7.88	.279	8.40	.327	.606	10,680
28		.267	5.80	.560	2.90	.046	.310	8,010
29		.267	5.80	.432	3.80	.165	.694	8,010
30		.267	5.80	.322	5.70	.260	.725	8,010
31		.267	5.80	.286	6.20	.266	.693	8,010
32		.258	2.77	.375	3.00	.076	.452	5,340
33		.258	2.77	.385	2.90	.085	.450	5,340
34		.258	2.77	.301	3.80	.154	.627	5,340
45	.091	.275	8.80	.620	3.60	.057	.322	10,930
46		.275	8.80	.404	5.90	.212	.591	10,930
47		.275	8.80	.313	8.20	.320	.712	10,930
48		.275	8.80	.290	8.70	.285	.670	10,930
50		.270	6.38	.450	3.80	.106	.503	8,200
51		.270	6.38	.311	5.80	.215	.631	8,200
52		.270	6.38	.290	6.10	.232	.624	8,200
53		.270	6.38	.280	6.20	.220	.602	8,200
54		.275	10.10	.567	4.50	.100	.410	12,580

TABLE 2 (continued)

Run	ε_x	α_0	S_0	α_1	S_1	$\left(\frac{d\alpha}{d\xi}\right)_{max}$	C_p	R_e
55	.091	.275	10.10	.424	6.40	.232	.581	12,580
56		.275	10.10	.366	7.80	.338	.765	12,580
57		.275	10.10	.300	9.80	.391	.600	12,580
58	.110	.276	10.30	.504	5.30	.146	.608	12,700
59		.276	10.30	.408	6.85	.230	.716	12,700
60		.276	10.30	.364	8.00	.253	.701	12,700
61		.276	10.30	.310	9.70	.372	.666	12,700
62		.276	8.40	.669	3.40	.064	.330	11,050
63		.276	8.40	.496	4.40	.147	.530	11,050
64		.276	8.40	.376	6.20	.230	.755	11,050
65		.276	8.40	.316	8.30	.288	.651	11,050
67		.271	6.50	.410	4.20	.139	.631	8,290
68		.271	6.50	.273	6.30	.197	.650	8,290
70		.276	5.60	.351	4.30	.141	.480	6,900
73	.142	.290	10.30	.513	5.30	.143	.664	12,640
74		.290	10.30	.387	7.50	.215	.676	12,640
75		.290	10.30	.336	9.00	.328	.750	12,640
77		.290	9.20	.417	6.00	.176	.588	11,240
78		.290	9.20	.316	8.60	.273	.762	11,240
80		.291	6.90	.465	3.75	.081	.481	8,420
81		.291	6.90	.371	5.30	.157	.575	8,420

TABLE 2 (continued)

Run	ϵ_x	α_0	S_0	α_1	S_1	$\frac{d\alpha}{d\xi}_{max}$	C_p	R_e
82	.142	.291	6.90	.310	6.60	.195	.695	8,420
83	.174	.288	10.40	.598	4.50	.077	.467	13,000
84		.285	10.30	.413	6.90	.200	.620	13,000
85		.293	10.40	.335	9.20	.262	.733	13,000
86		.293	10.40	.295	10.40	.278	.772	13,000
87		.296	9.42	.732	3.1	.033	--	11,430
88		.291	9.40	.421	6.20	.168	.580	11,430
89		.291	9.40	.322	8.80	.218	.663	11,430
90		.296	7.10	.578	3.20	.034	.250	8,575
91		.285	7.20	.385	5.20	.146	.700	8,575
92		.275	7.30	.300	7.00	.187	.690	8,575

LIST OF FIGURES

Fig. 1 Schematic of the overall apparatus: A - upstream head tank, B - rotameter, C - pressure transducer, D - traversing drive, E - potentiometer, F - test section, G - area probe voltage pick-off, H - teflon tubing, I - pulley, J - tilting table, K - calibration voltage pick-off, L - downstream head tank, M - circulating pump.

Fig. 2 Details of the test section: tension-friction flow, B - glycerine in water mixture, C - probe catheter, D - rigid tubing, E - seal ring, F - end cap, G - flanged plexiglas tube, H - latex tube, I - external pressure port, J - adjustable sphincter.

Fig. 3 Details of the test section: gravity-friction flow, A - adjustable sphincter, B - flat plate, C - rod for creating disturbance, D - probe catheter.

Fig. 4 Schematic of the test section showing elements of the electrical impedance technique for measuring cross-sectional area.

Fig. 5 Block diagram of the impedance method instrumentation.

Fig. 6 Sources of error: common mode and shunt leakage effects.

Fig. 7 Area measurement of a rigid converging-diverging tube; solid line by volumetric excursion method; open circles by electrical impedance technique.

Fig. 8a Log-log plot of P versus α; enlarged to show details of the region $\alpha < 0.25$, indicating similarity and probe interference.

Fig. 8b The local tube law: open circles are P-α data; solid line is the derived infinite wavelength phase velocity c_∞. (Data included in Table 1).

Fig. 8c Plot of P vs. $(1-\alpha^{-2})$ for $\alpha \geq 1.00$, the inflated tube, showing correlation with Eq. (5b).

Fig. 9 A local tube law for the same tube as in Fig. 8a-8c but supported by a flat plate; open circles are unsmoothed P-α data; solid line is derived c_∞.

Fig. 10 Gravity-friction experimental result: α vs. x; $\alpha_0 = 0.384$, $S_0 = 4.2$, $\theta = 4.8°$; at maximum area ratio $\alpha = 0.625$, $S = 1.8$.

Fig. 11 Gravity-friction experimental result: α vs. x, inlet area ratio and flow rate adjusted for constant $\alpha = 0.70$, $S = 1.40$, $\theta = 4.8°$, small disturbance near exit.

Fig. 12 Gravity-friction experimental result; α vs. x, $\alpha_0 = 0.450$, $S_0 = 4.7$, $\theta = 9.0°$; large disturbance creates shock with standing waves.

Fig. 13a Typical data record: tension-friction flows; $(A-A_p)$ vs. x, p vs. x; A - rigid tube, B - inflated tube, C - sphincter region, D - standing waves, E - shock-like transition, F - inflated tube, G - rigid tube.

Fig. 13b Photograph of a typical tension-friction flow; front view showing all features mentioned in relation to Fig. 13a.

Fig. 13c Photograph of same flow as in Fig. 13b, angled close-up revealing four distinct standing waves.

Fig. 14 Tension-friction experimental results: α vs. ξ, runs 1-4 for four levels of downstream pressure, $\alpha_0 = 0.270$, $S_0 = 8.0$, $\varepsilon_x = 0.023$.

Fig. 15a-d Tension-friction experimental results representative of four broad classes based on axial strain and inlet speed index, α vs. ξ.

Fig. 15a Small ε_x, small S_0: run no. 10, $\alpha_0 = .252$, $S_0 = 1.7$, $\varepsilon_x = 0.023$.

Fig. 15b Small ε_x, large S_0: run no. 1, $\alpha_0 = .270$, $S_0 = 8.0$, $\varepsilon_x = 0.023$.

Fig. 15c Large ε_x, small S_0: run no. 79, $\alpha_0 = .291$, $S_0 = 6.9$, $\varepsilon_x = 0.142$.

Fig. 15d Large ε_x, large S_0: run no. 83, $\alpha = .290$, $S_0 = 1.4$, $\varepsilon_x = 0.174$.

Fig. 16 The shock model: showing inlet and outlet locations, designated control volume.

Fig. 17 Plot of C_p vs. α_1: experimental pressure recovery coefficient vs. shock inlet area ratio, dashed lines indicate theoretical results discussed in Chapter III.

Fig. 18 The tube model: assumed geometric shape for a partially collapsed tube.

Fig. 19 Log-log plot of $\sqrt{S^2 - 1}$ versus $\lambda \sqrt{\frac{\rho c_\infty^2 \sqrt{1-\bar{\alpha}}}{\pi^2 T D_0 \bar{\alpha}}}$ for experimental tension-friction flows; dashed line is theoretical inviscid dispersion relation Eq. (45).

Fig. 20 Gravity-friction experimental results: log-log plot of experimentally obtained skin friction coefficient, $\bar{f}_{exp}$, versus Reynolds number.

Fig. 21 Tension-friction experimental results: log-log plot of experimentally obtained skin friction coefficient, $\bar{f}_{exp}$, versus Reynolds number.

Fig. 22a Schematic curve of α vs. ξ showing method for estimating wave amplitude.

Fig. 22b Plot of $-\ell n(\Delta\alpha/\Delta\alpha_0)$ vs. ξ' indicating method for estimating wave amplitude decay rate.

Fig. 23 Plot of $k_i D_0$ vs. $\bar{k}_r D_0$: wave amplitude decay rates versus mean real wave number; both tension friction and gravity-friction flows.

Fig. 24 Schematic plot of α vs. ξ for typical shock and wave train, indicating exponential envelope and two important gradients in area ratio.

Fig. 25 Experimental results: maximum area ratio gradient in shock vs. shock inlet parameters; dashed line shown is theoretical result of Eq. (76).

Fig. 26 Numerical results: α vs. ξ, forward integrations, initial conditions $\alpha_0 = 0.275$, $S_0 = 10.0$, $\varepsilon_x = 0.10$, $(d^2\alpha/d\xi^2) = 0.0$, for three different initial gradients $(d\alpha/d\xi)_0 = 0.03$ heavy line, 0.075 medium line, 0.135 light line.

Fig. 27 Numerical results: α vs. ξ, forward integrations, initial conditions $\alpha_0 = 0.275$, $S_0 = 10.0$, $\varepsilon_x = 0.025$ $(d^2\alpha/d\xi^2)_0 = 0.00$, for three different initial gradients $(d\alpha/d\xi)_0 = 0.030$ heavy line, 0.135 medium line, 0.195 light line.

Fig. 28 Log-log plot of $\sqrt{S^2 - 1}$ vs. $\lambda \sqrt{\frac{\rho c_\infty^2}{\pi^2 T \bar{\alpha} D_0}}$ from numerical results.

Fig. 29 Numerical results: α vs. ξ, forward integration with additional skin friction coefficient term $r = 0.03$, initial conditions $\alpha_0 = 0.275$, $S_0 = 10.0$, $\varepsilon_x = 0.10$, $(d^2\alpha/d\xi^2)_0 = 0.0$, $(d\alpha/d\xi)_0 = 0.03$.

Fig. 30 Numerical results: α vs. ξ, forward integration with additional skin friction coefficient term $r = 0.01$, initial conditions $\alpha_0 = 0.275$, $S_0 = 10.0$, $\varepsilon_x = 0.025$, $(d^2\alpha/d\xi^2)_0 = 0.0$, $(d\alpha/d\xi)_0 = 0.03$.

Fig. 31 Numerical results: α vs. ξ, backwards integration, additional skin friction coefficient term with $r = 0.03$, initial conditions $\alpha_0 = 1.00$, $S = 0.15$, $\varepsilon_x = 0.10$, $(d^2\alpha/d\xi^2)_0 = (d\alpha/d\xi)_0 = 0.0$.

Fig. 32 Numerical results: α vs. ξ, backwards integration; addition skin friction coefficient term with $r = 0.01$. Initial conditions $\alpha_0 = 1.00$, $S_0 = 0.15$, $\varepsilon_x = 0.025$, $(d^2\alpha/d\xi^2)_0 = (d\alpha/d\xi)_0 = 0.00$.

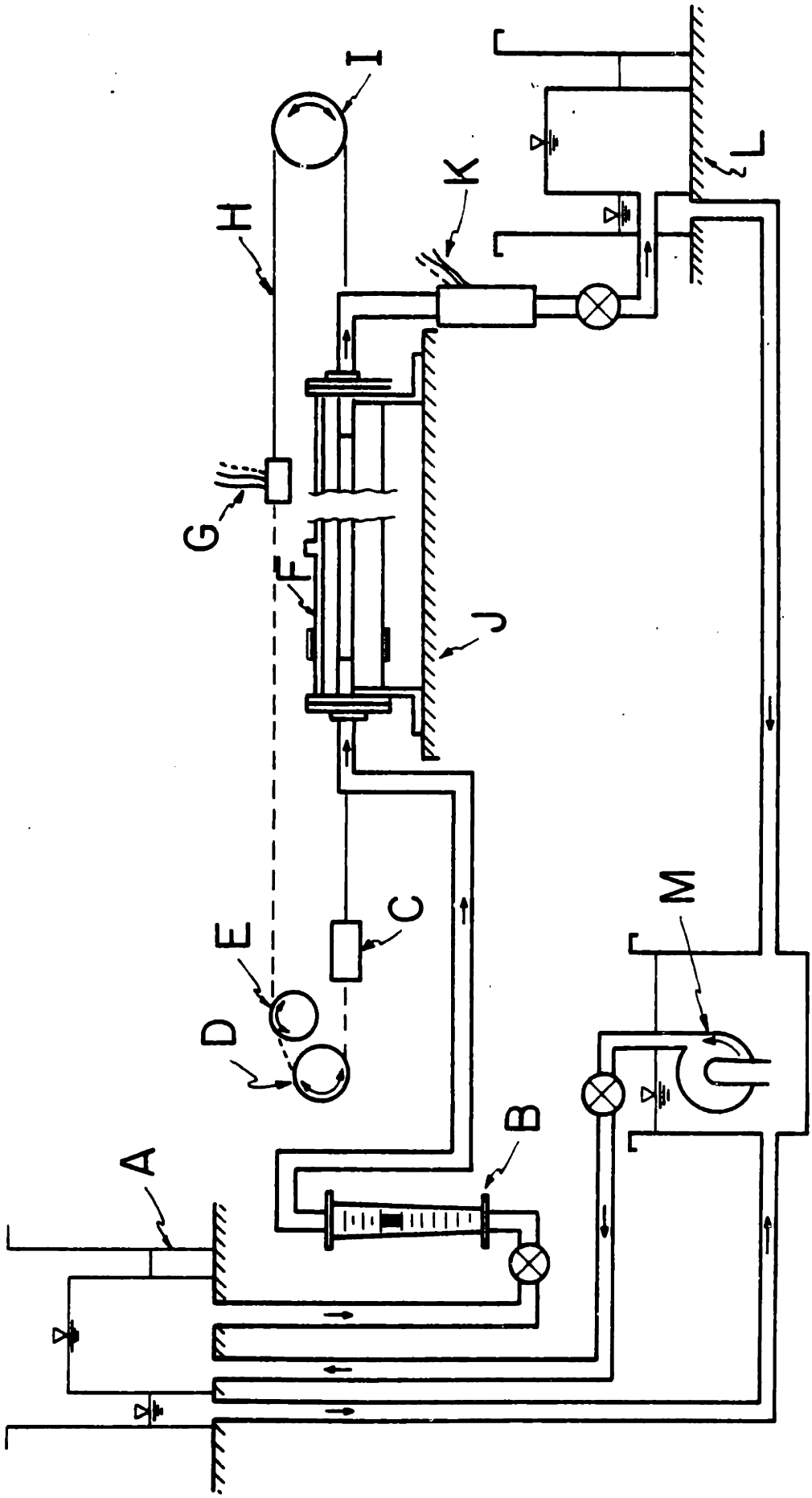

Figure 1

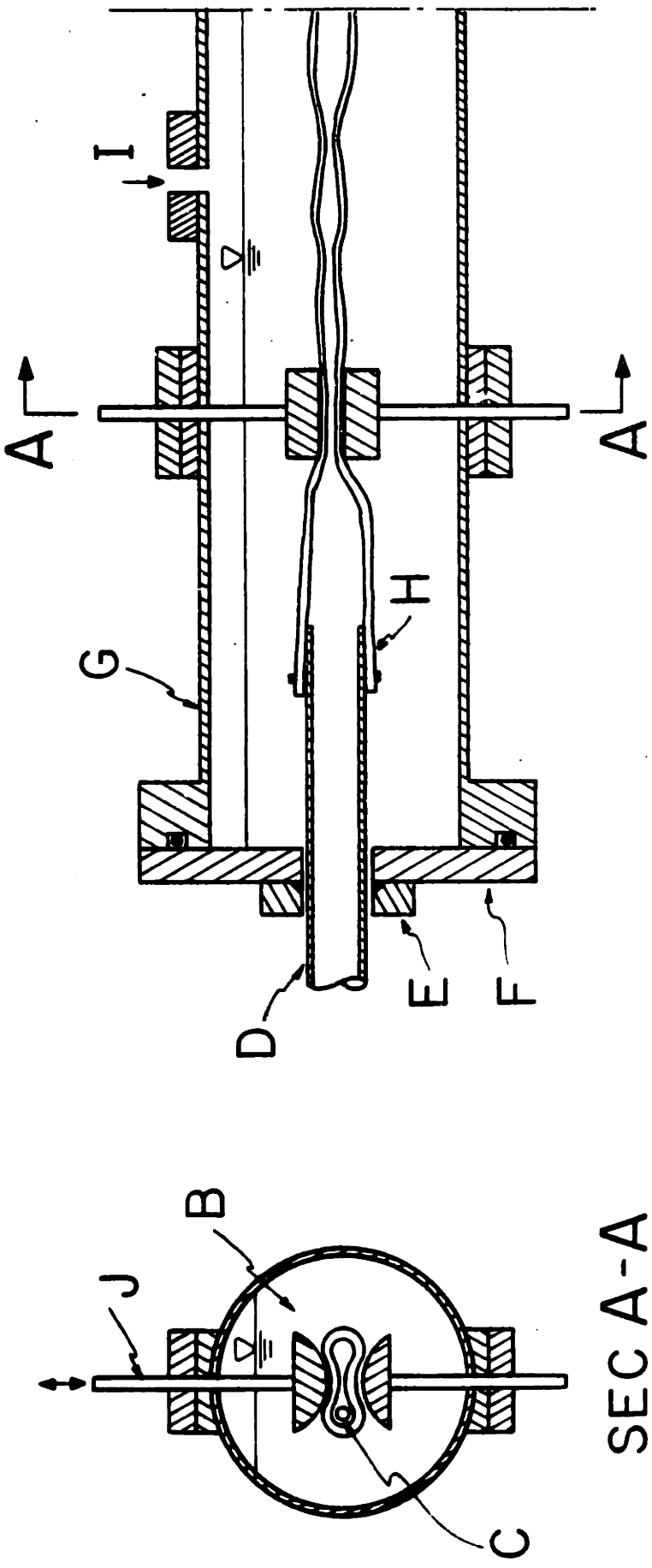

Figure 2

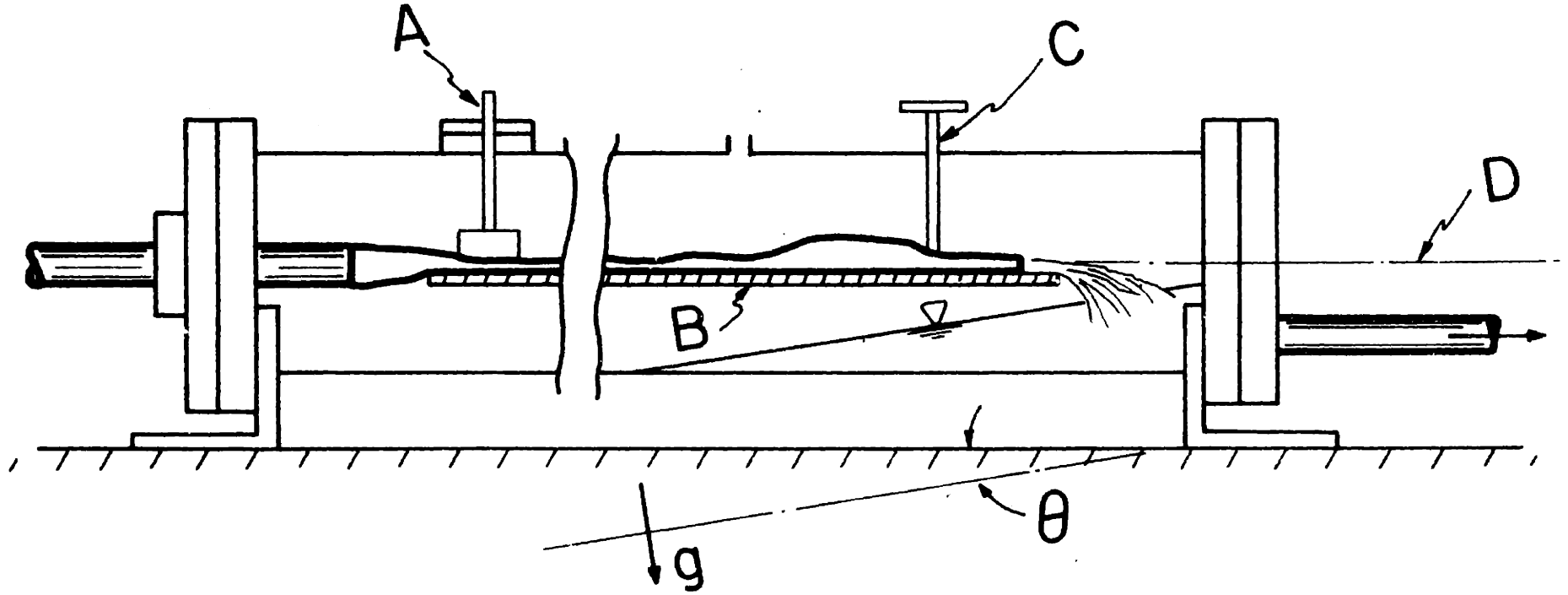

Figure 3

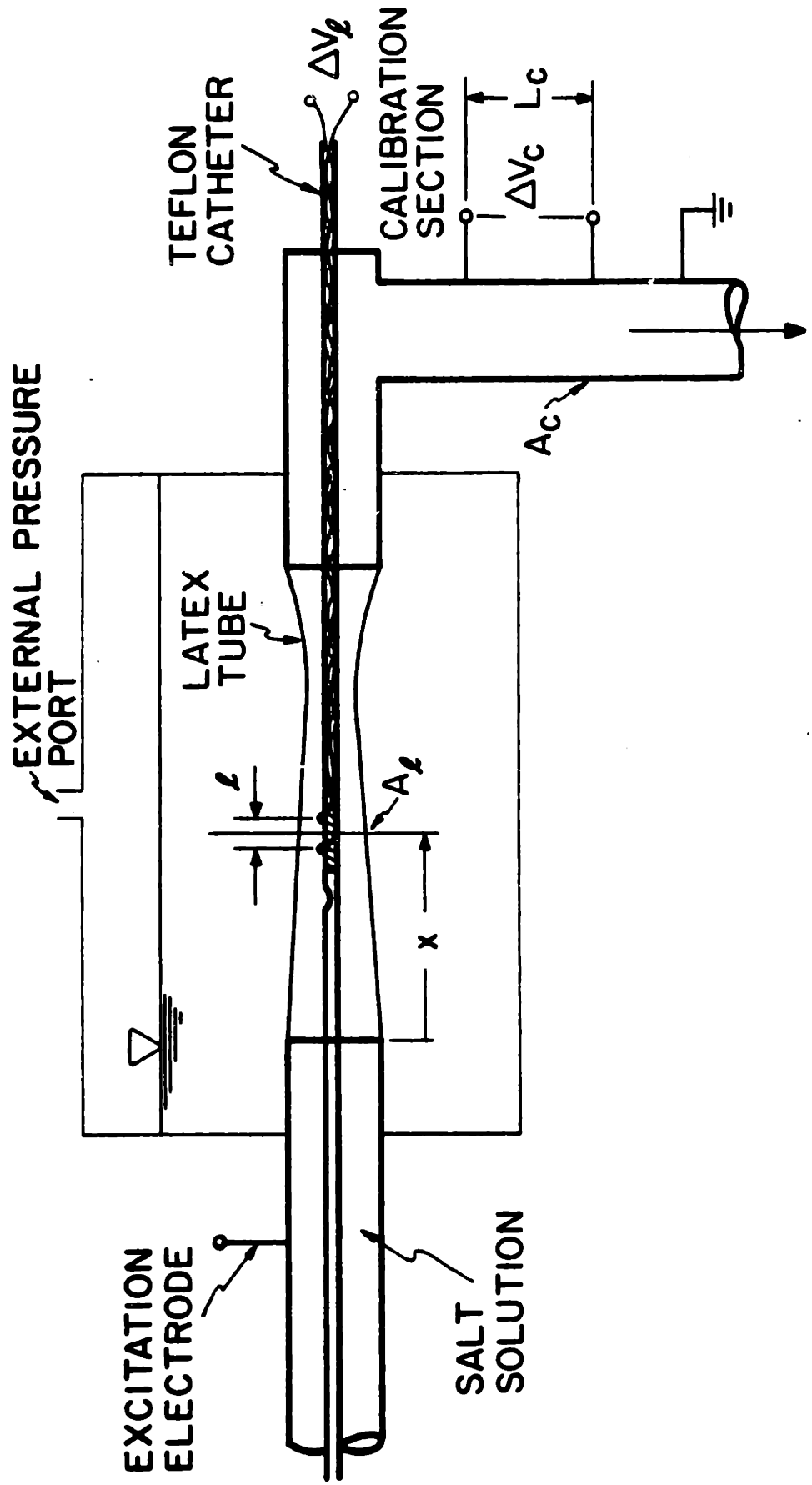
EXTERNAL PRESSURE PORT
LATEX TUBE
TEFLON CATHETER
ΔV_ℓ
CALIBRATION SECTION
L_c
ΔV_c
A_c
ℓ
A_ℓ
x
EXCITATION ELECTRODE
SALT SOLUTION

Figure 4

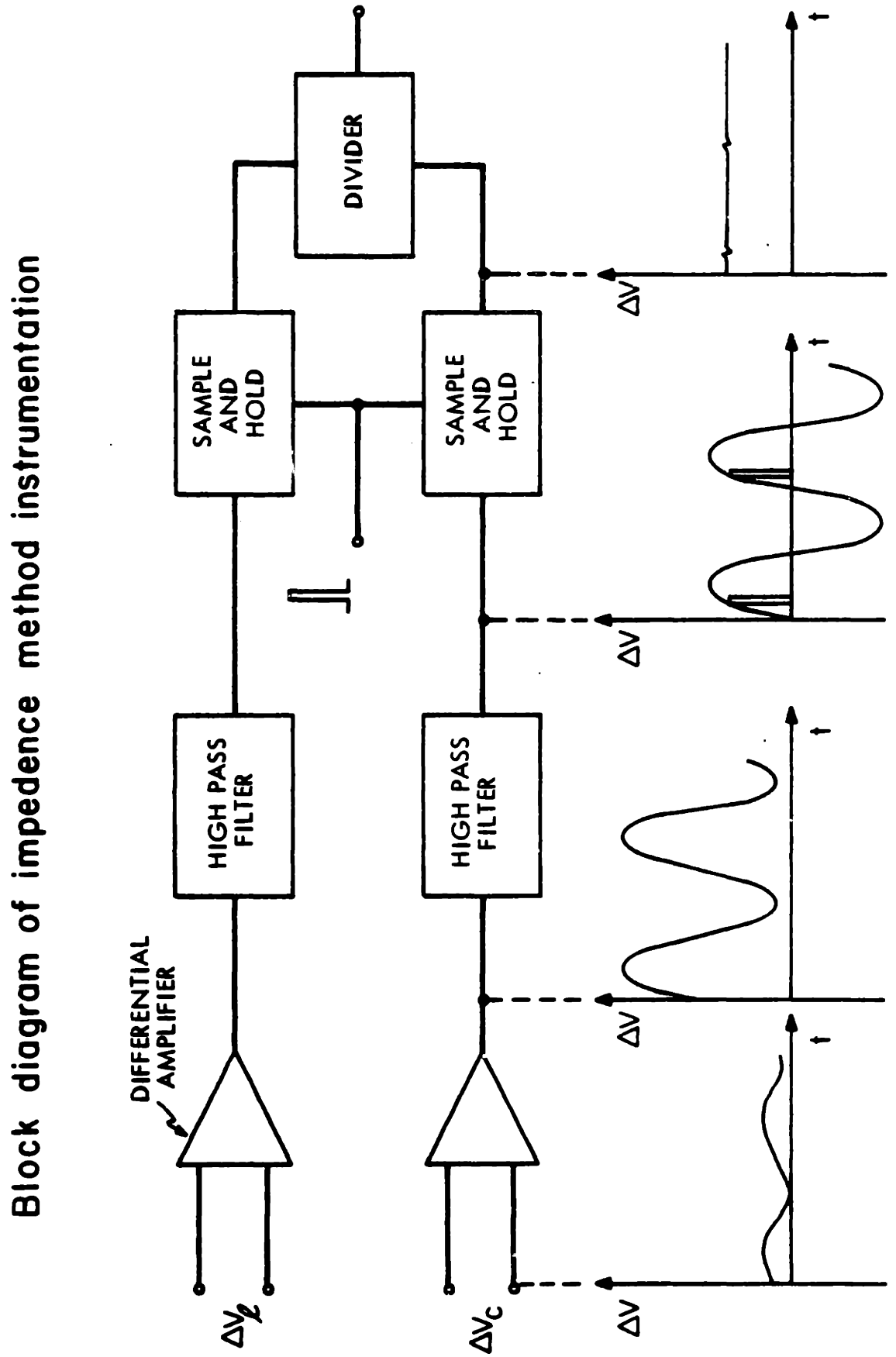
Block diagram of impedence method instrumentation
DIFFERENTIAL AMPLIFIER
HIGH PASS FILTER
HIGH PASS FILTER
SAMPLE AND HOLD
SAMPLE AND HOLD
DIVIDER
ΔVℓ
ΔVc
ΔV
t

Figure 5

Sources of error

COMMON MODE

- CMRR = $20 \log_{10} \left(\frac{E_{cm}}{E_{cm_e}} \right)$
- E_{cm_e} INCREASES ΔV_ℓ PRIMARILY
- CMRR DECREASES AS EXICITATION FREQUENCY INCREASES

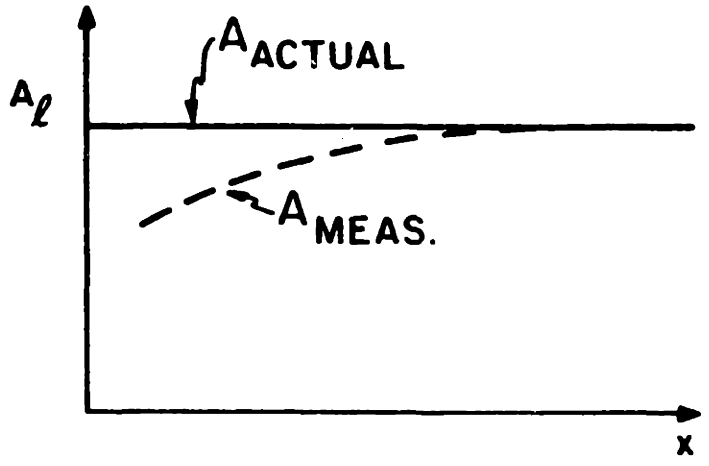

SHUNT LEAKAGE

- PRIMARILY RESISTIVE BUT INCREASES WITH EXCITATION FREQUENCY
- CURRENT LEAKAGE DECREASES ΔV_ℓ
- MAXIMUM ERROR $\sim \left(\frac{R_{internal}}{R_{external}} \right)$

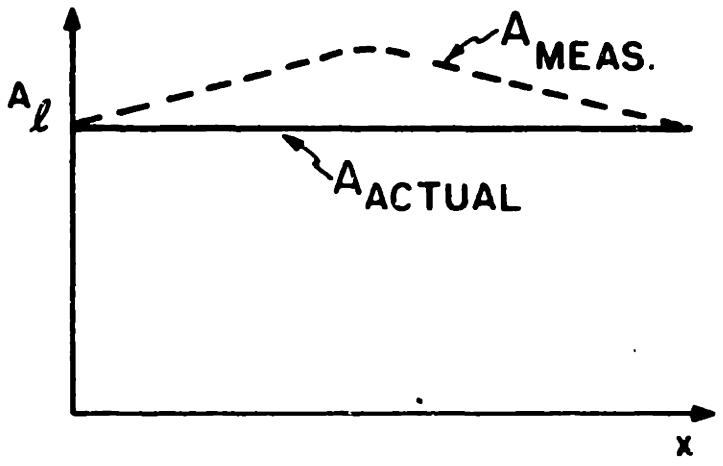

Figure 6

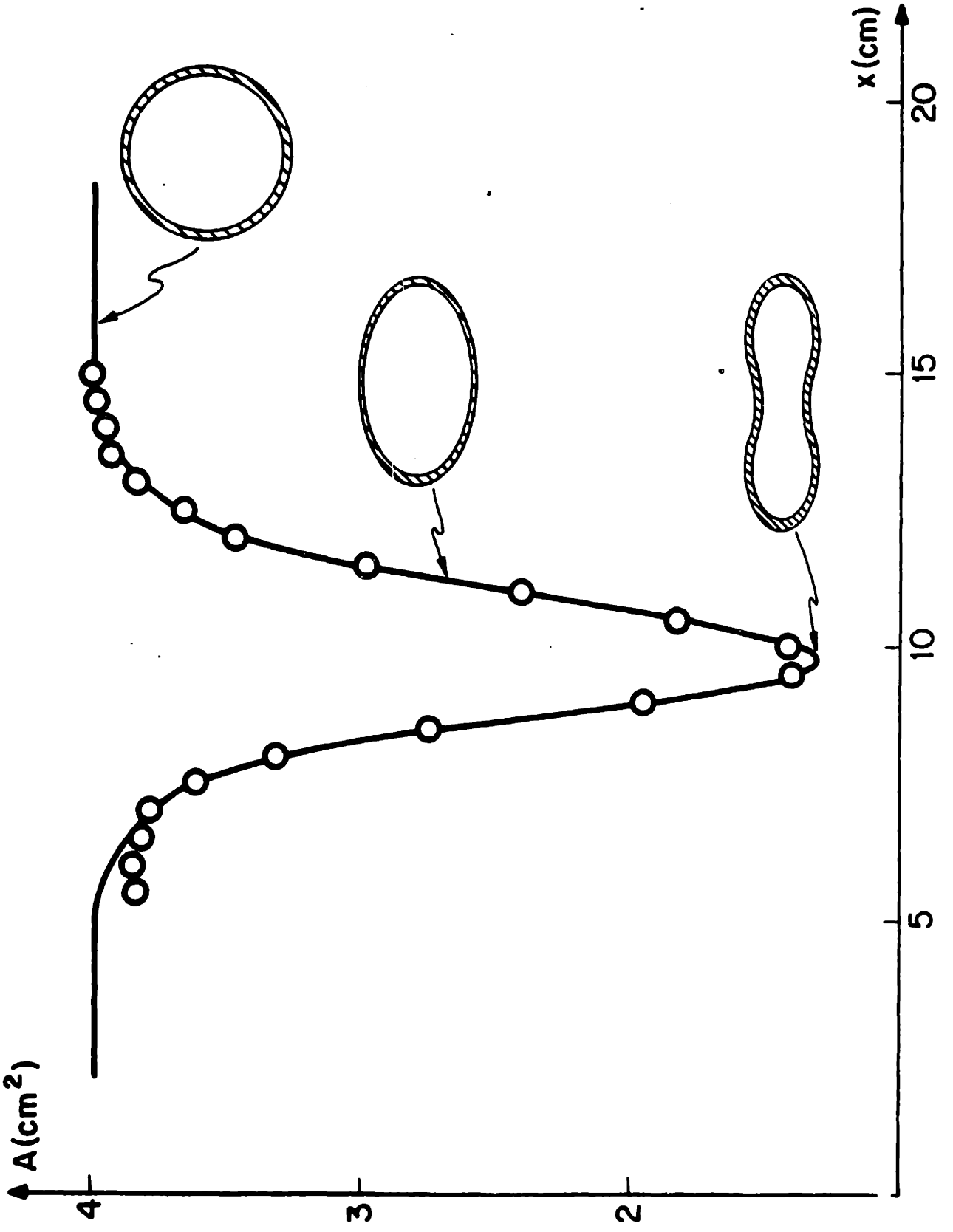

Figure 7

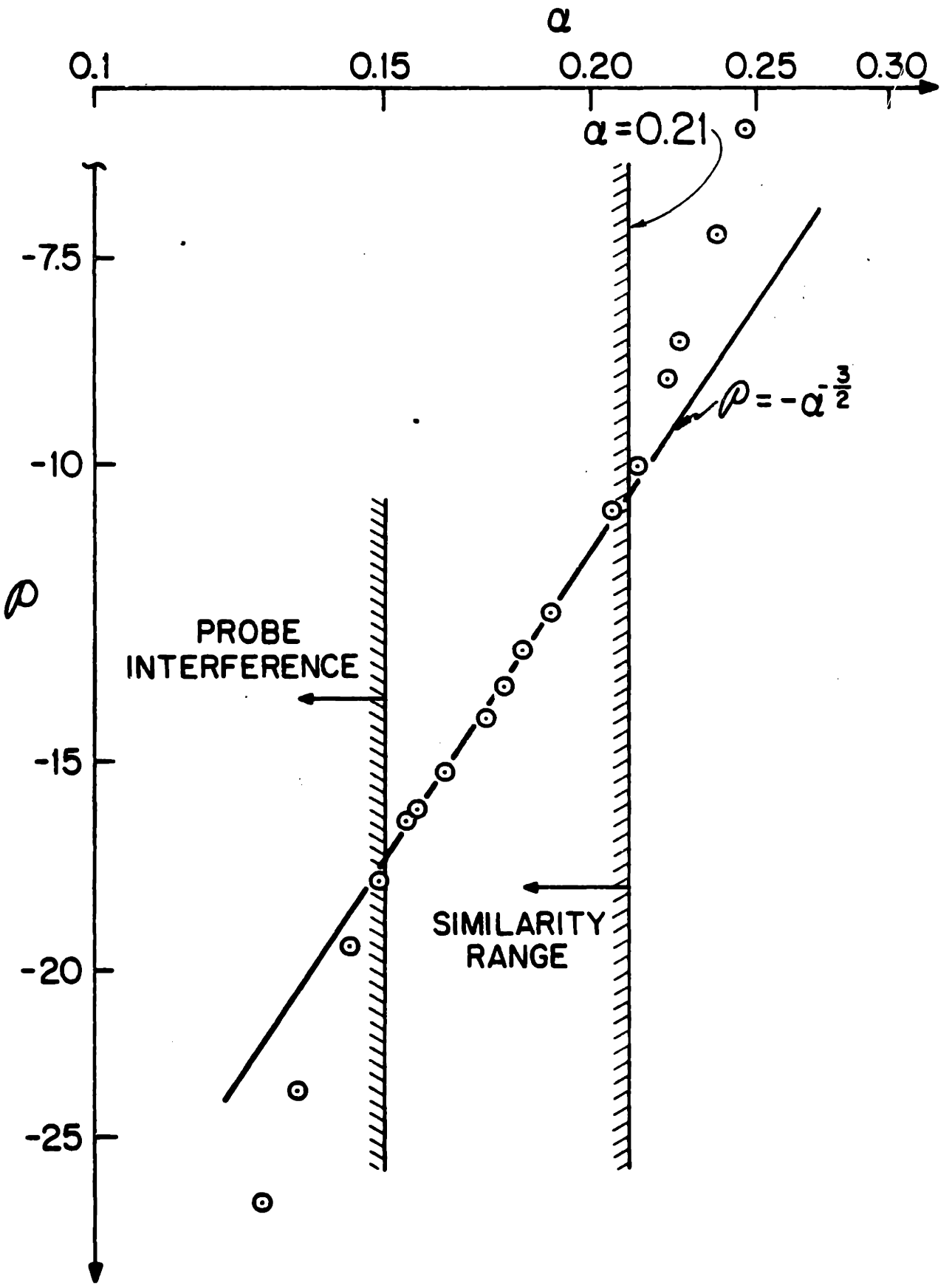
α
0.1
0.15
0.20
0.25
0.30
α=0.21
-7.5
-10
-15
-20
-25
ρ
ρ = -α^-3/2
PROBE
INTERFERENCE
SIMILARITY
RANGE

Figure 8a

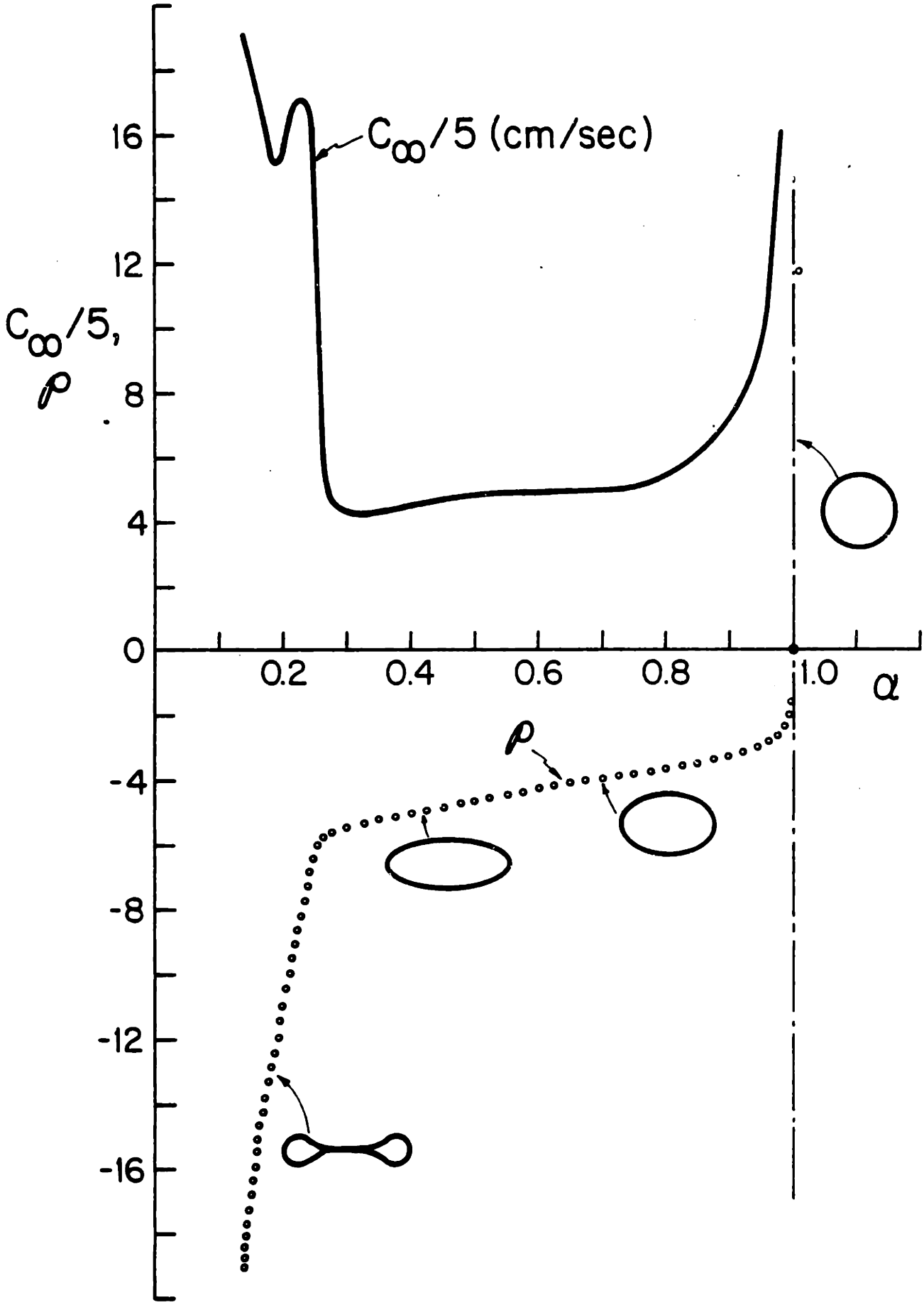
$C_\infty/5$ (cm/sec)
$C_\infty/5$, ρ
16
12
8
4
0
-4
-8
-12
-16
0.2
0.4
0.6
0.8
1.0
α
ρ

Figure 8b

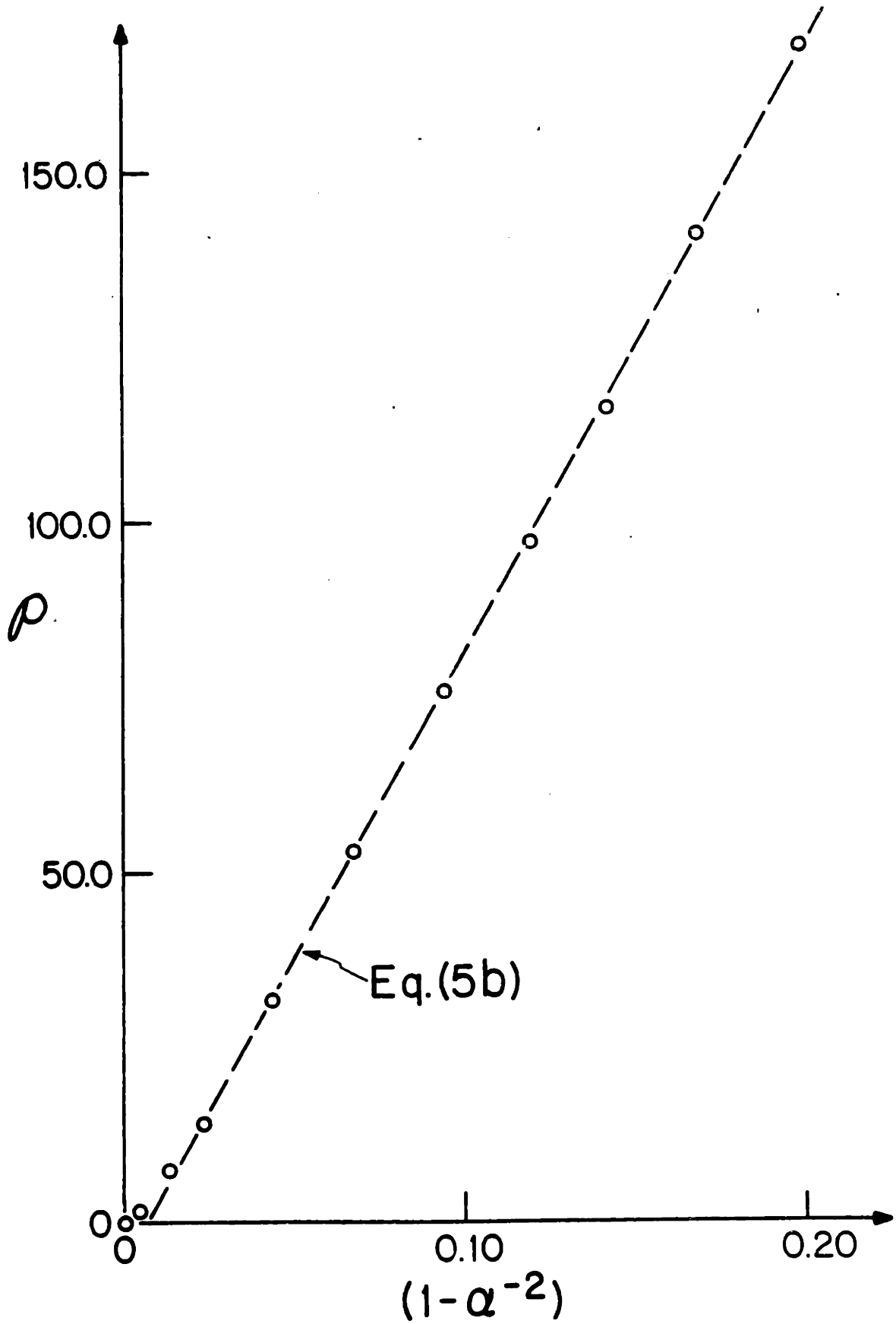

Figure 8c

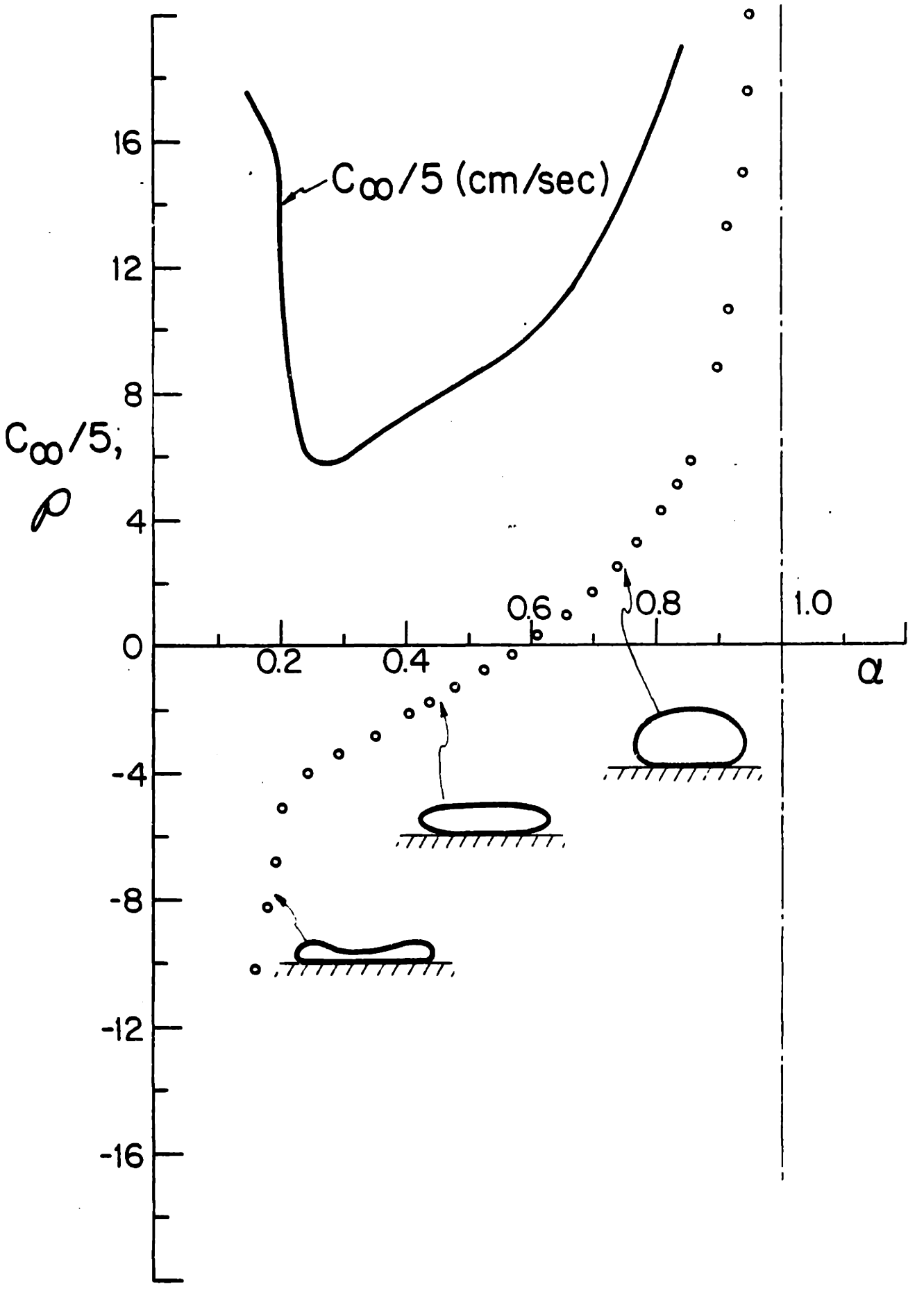
$C_\infty/5$ (cm/sec)
$C_\infty/5$, ρ
16
12
8
4
0
-4
-8
-12
-16
0.2
0.4
0.6
0.8
1.0
α

Figure 9

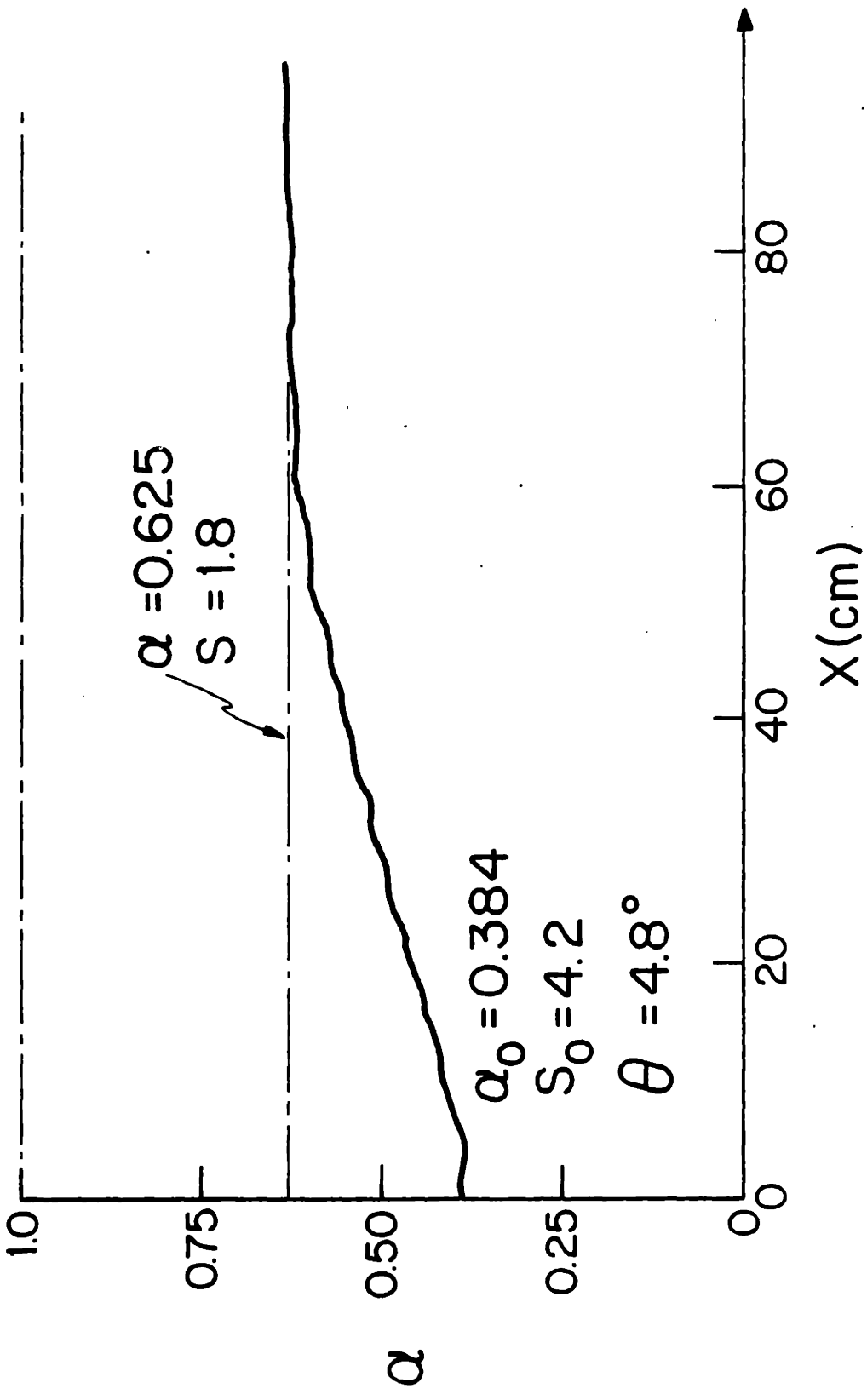

Figure 10

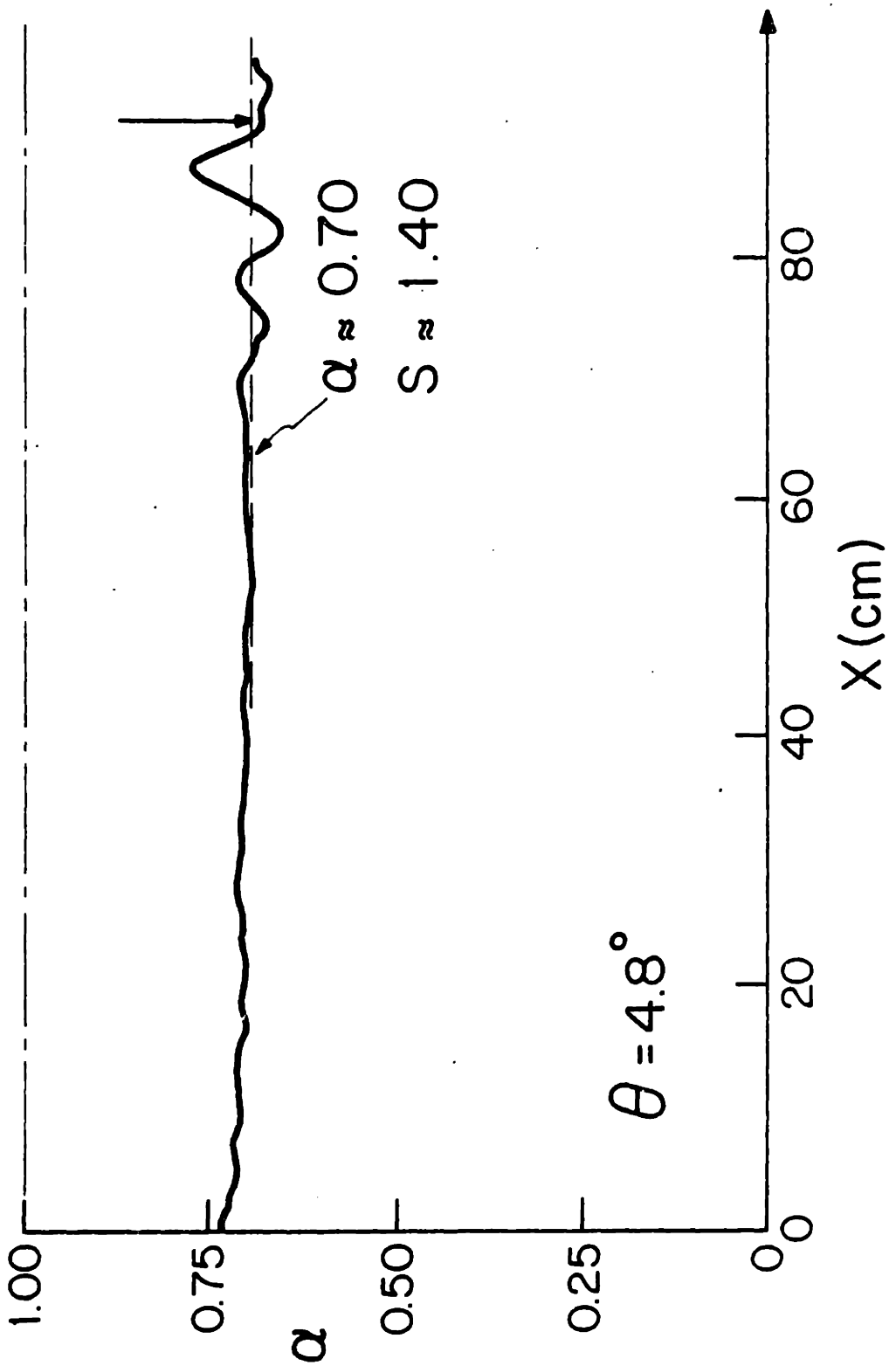

Figure 11

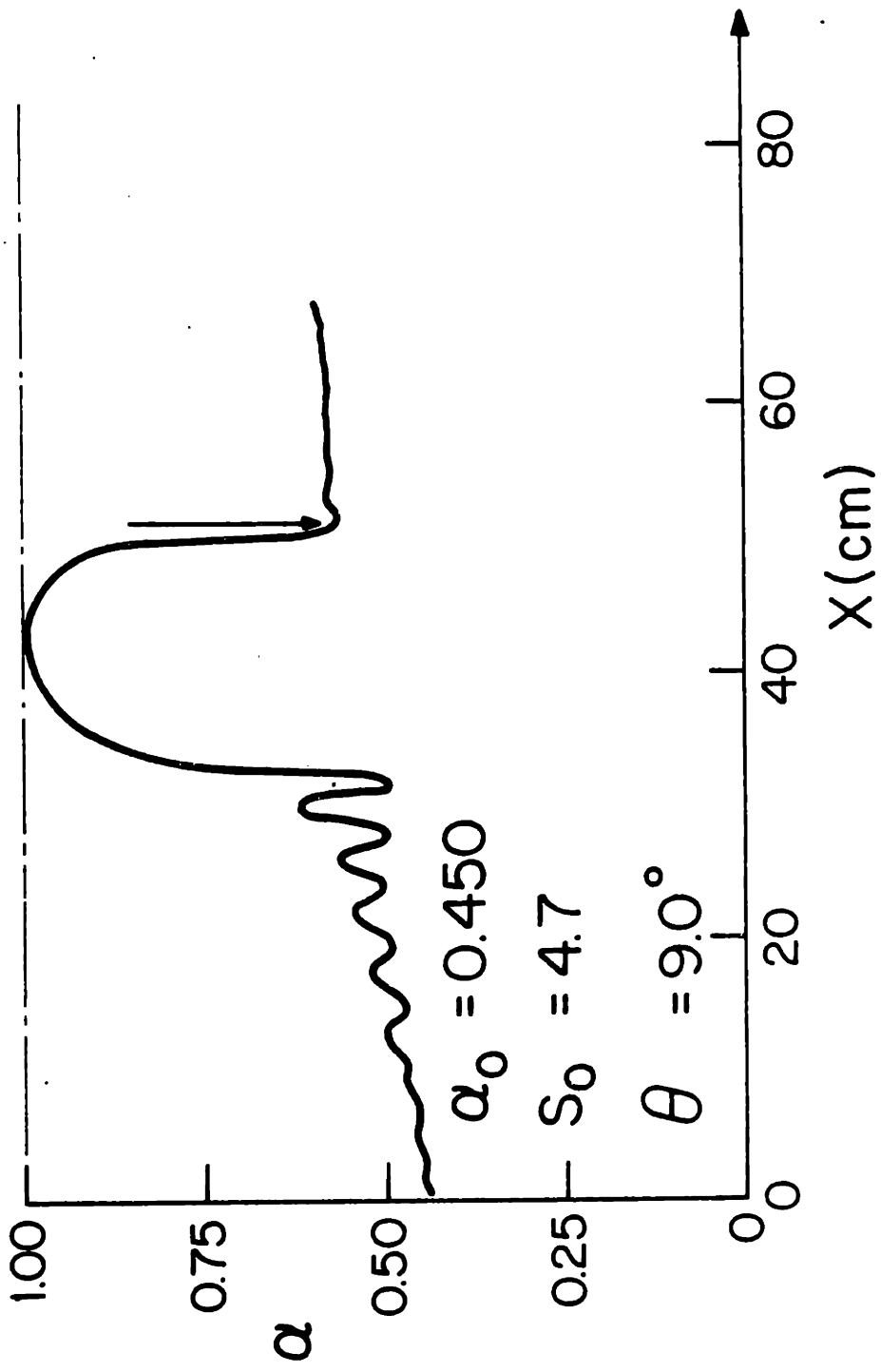

Figure 12

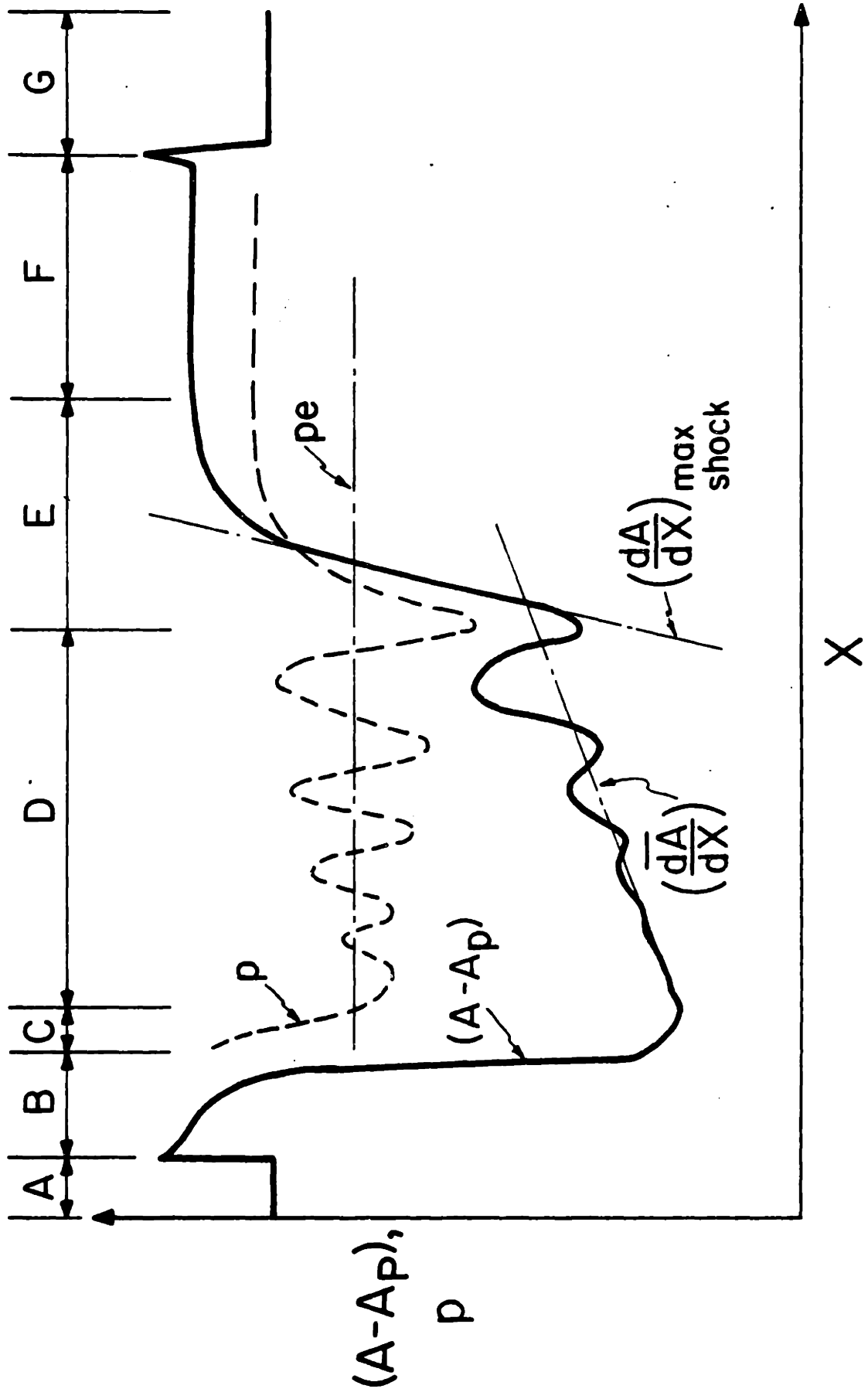

Figure 13a

Figure 13b

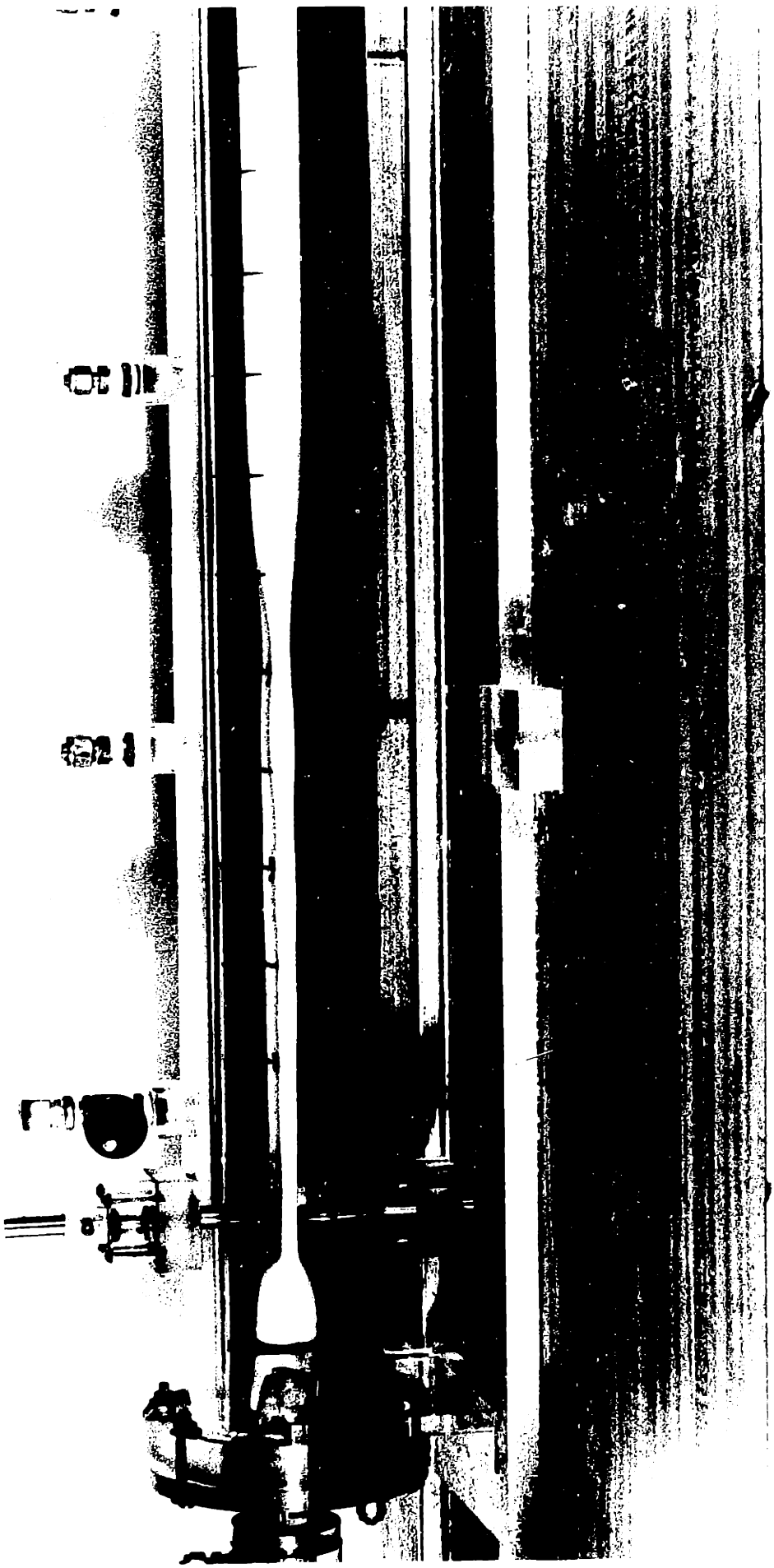

Figure 13b

Figure 13c

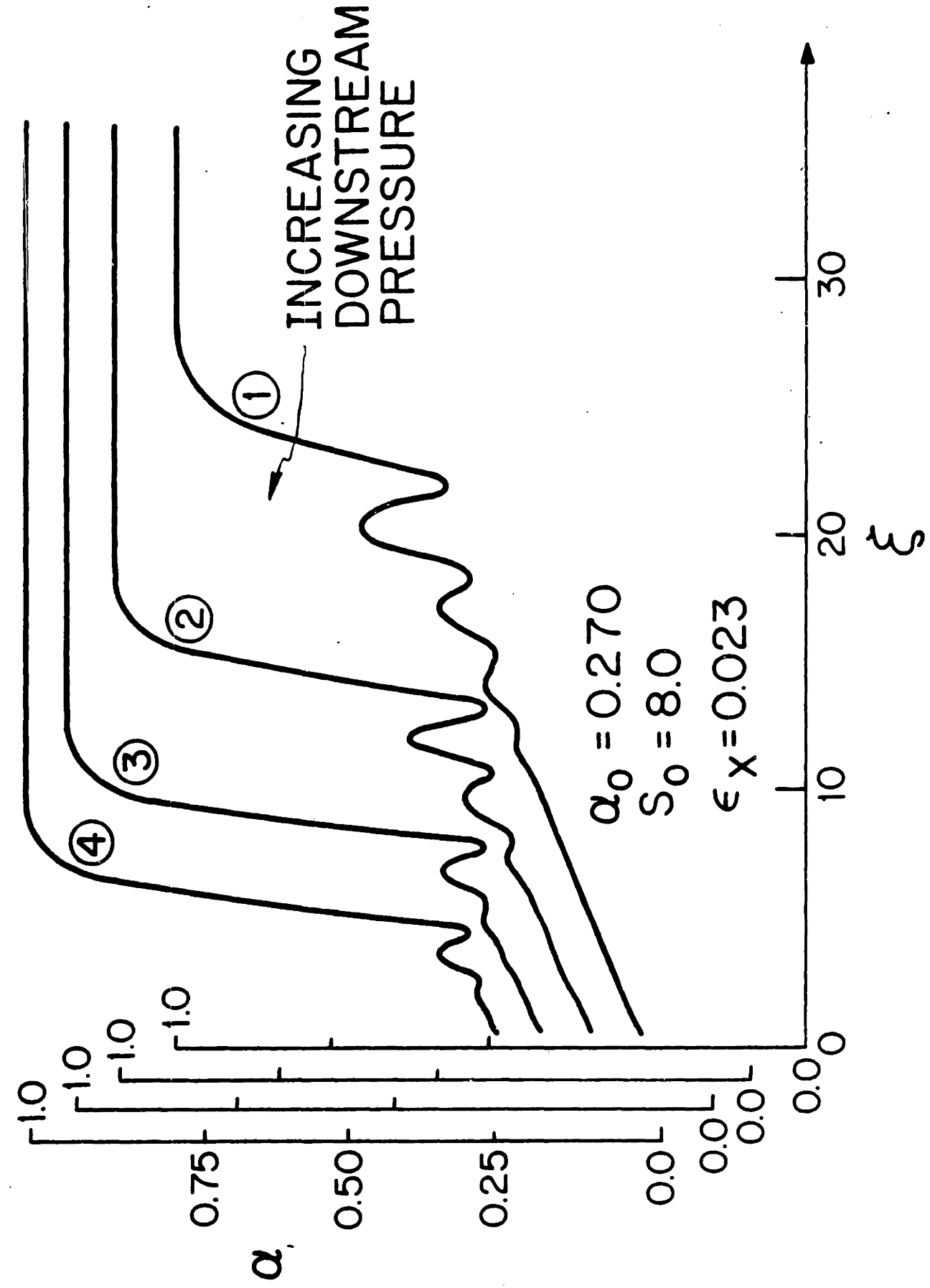
INCREASING
DOWNSTREAM
PRESSURE
1
2
3
4
$\alpha_o = 0.270$
$S_o = 8.0$
$\epsilon_x = 0.023$
α
ξ
0.0
0.25
0.50
0.75
1.0
10
20
30

Figure 14

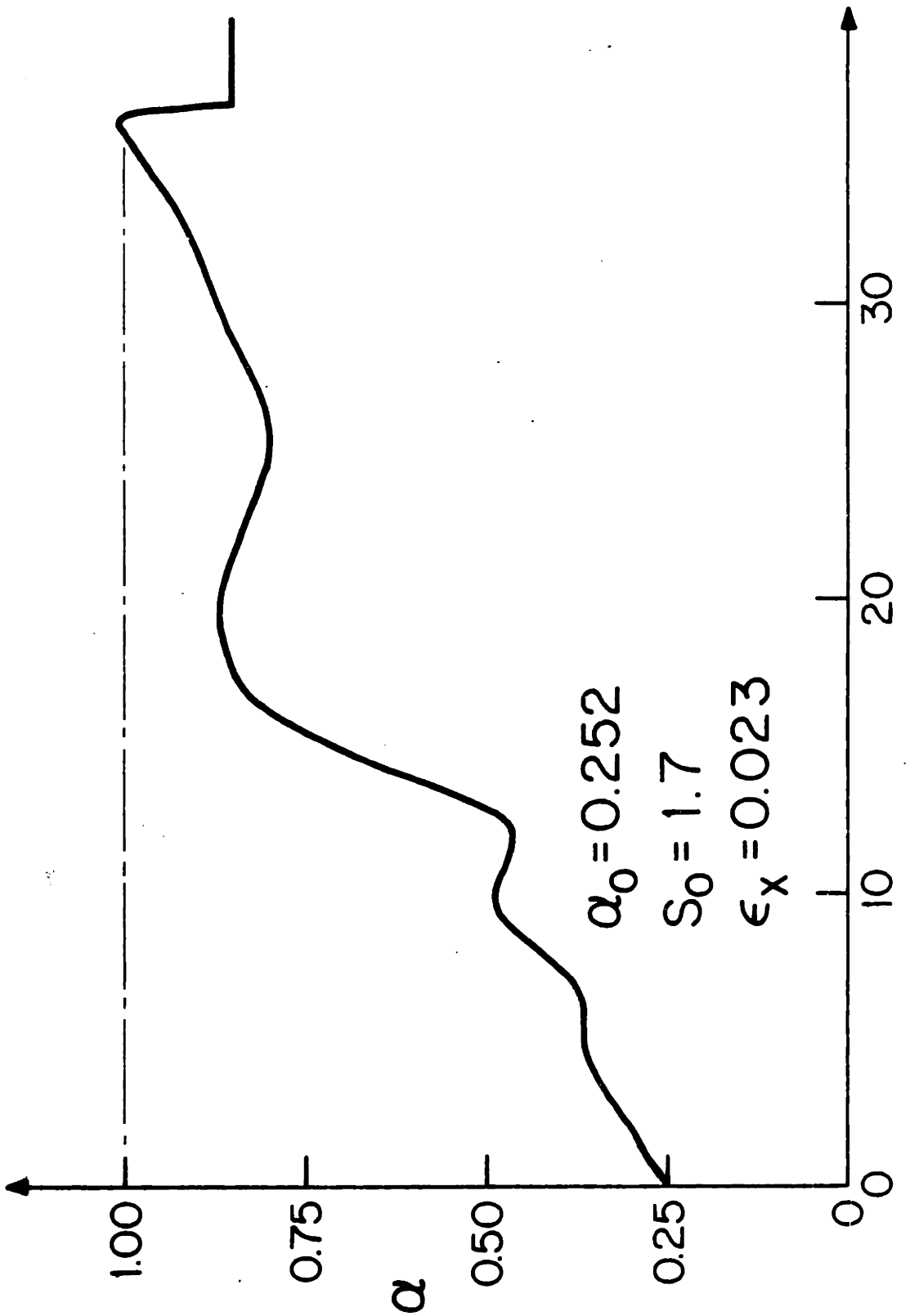

Figure 15a

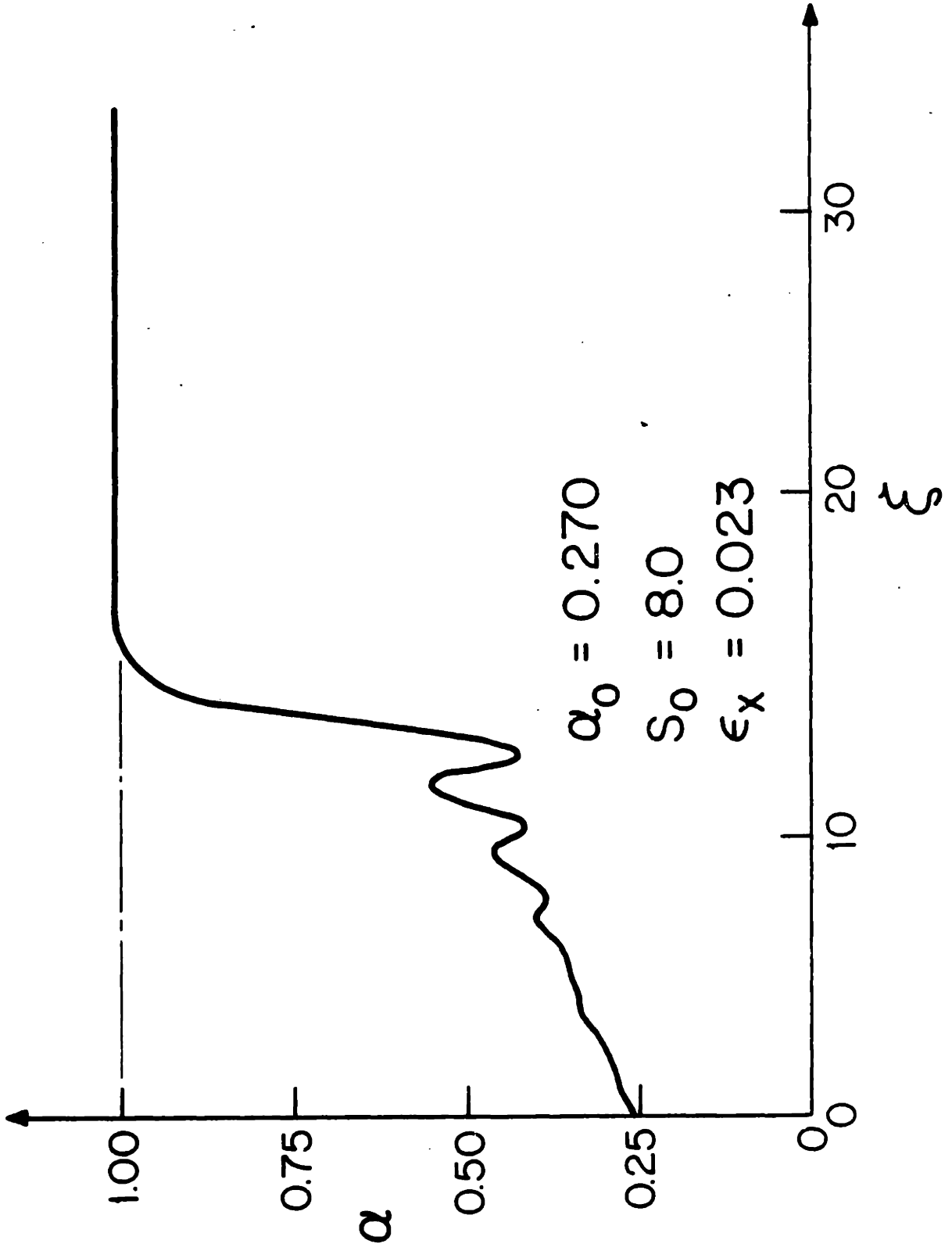

Figure 15b

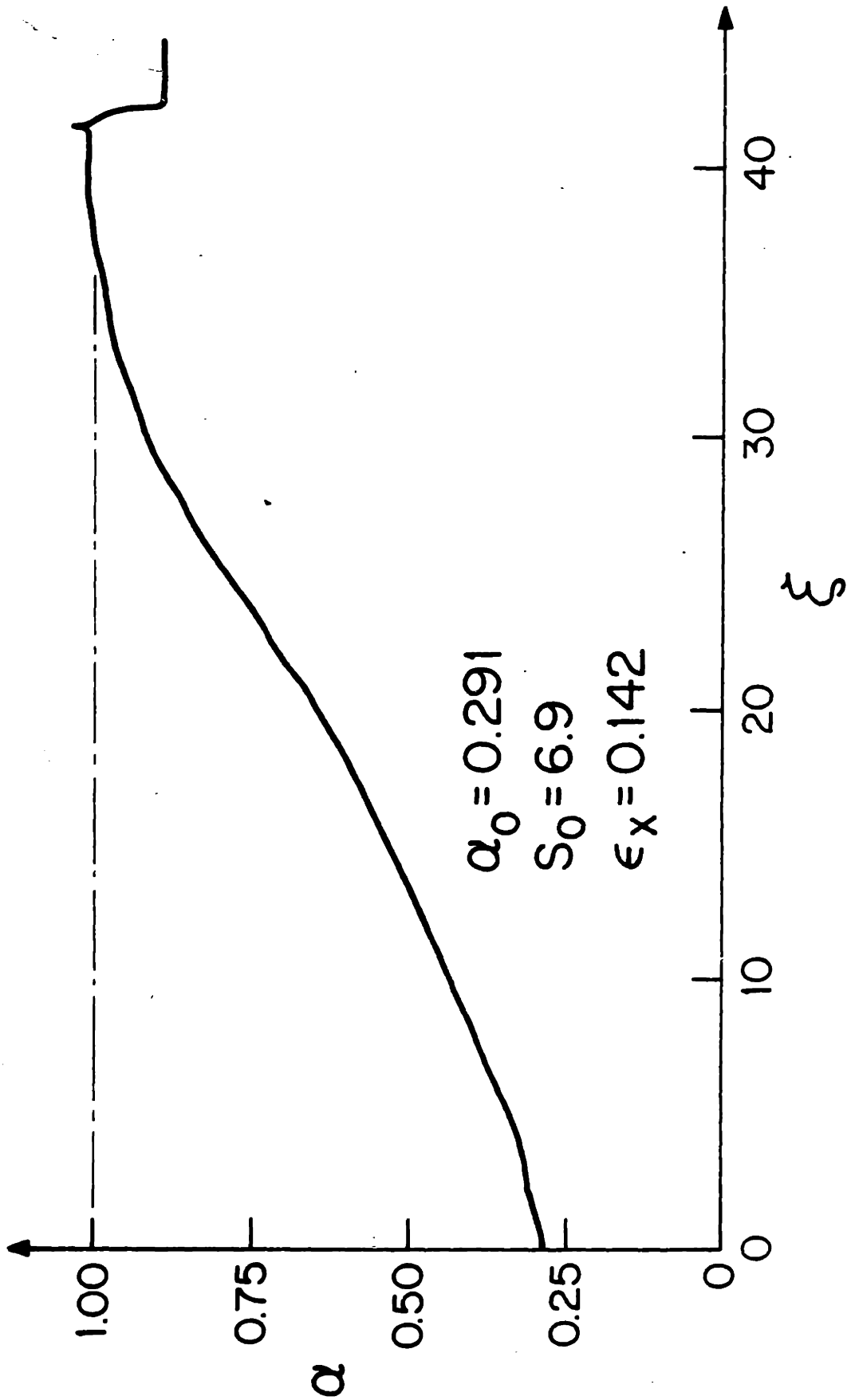

Figure 15c

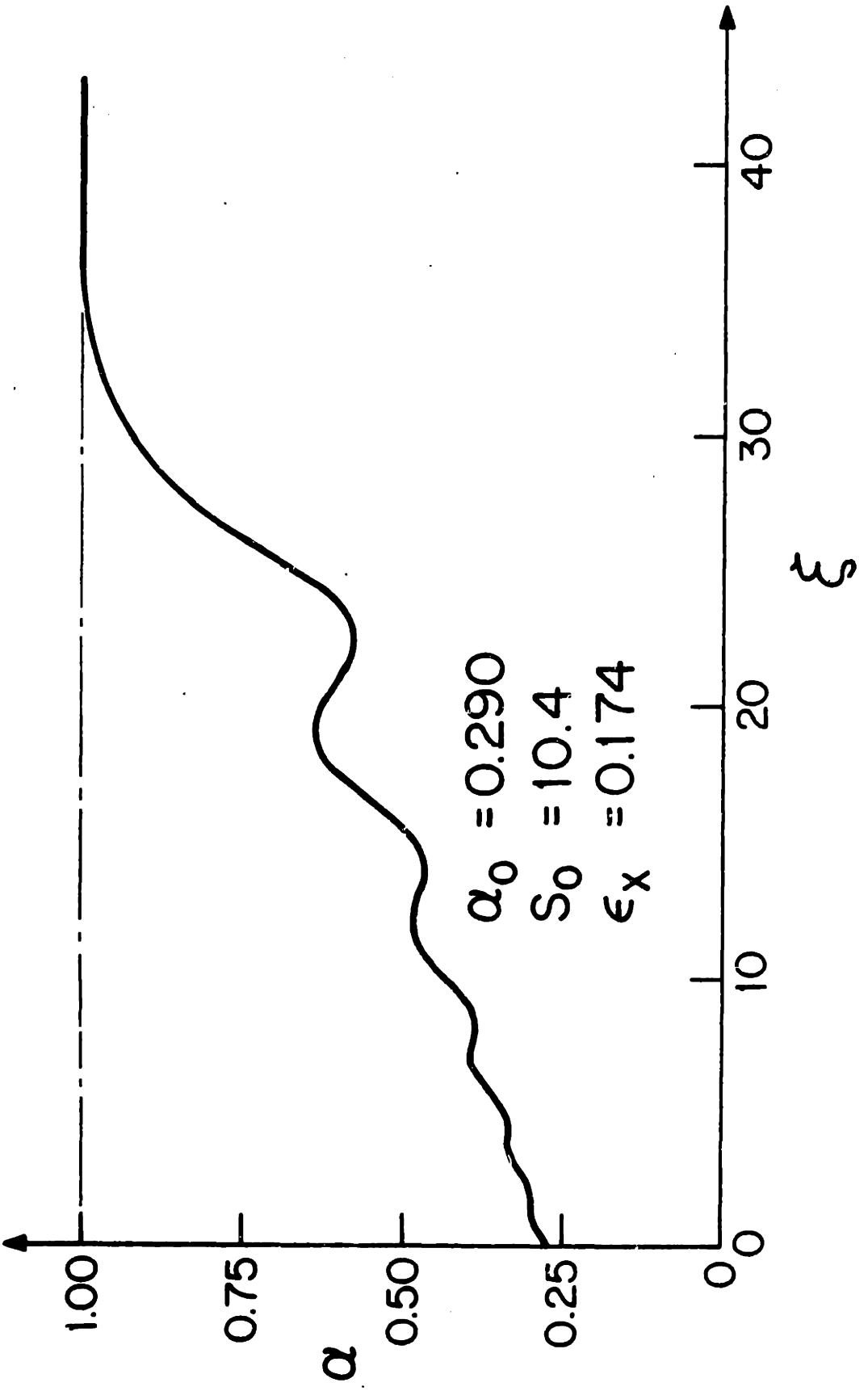
1.00
0.75
0.50
0.25
α
0
10
20
30
40
ξ
α_0 =0.290
S_0 =10.4
ϵ_x =0.174

Figure 15d

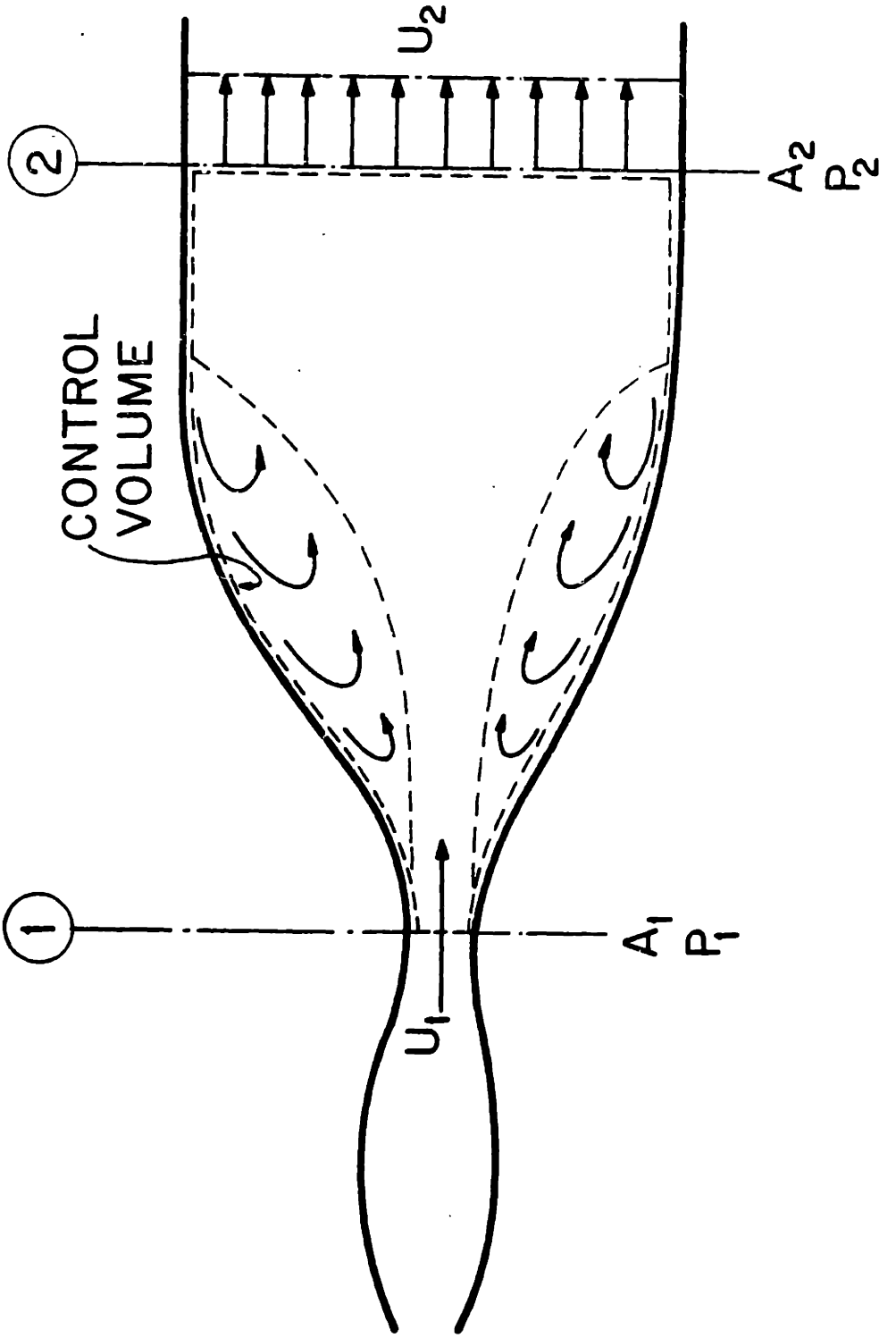

Figure 16

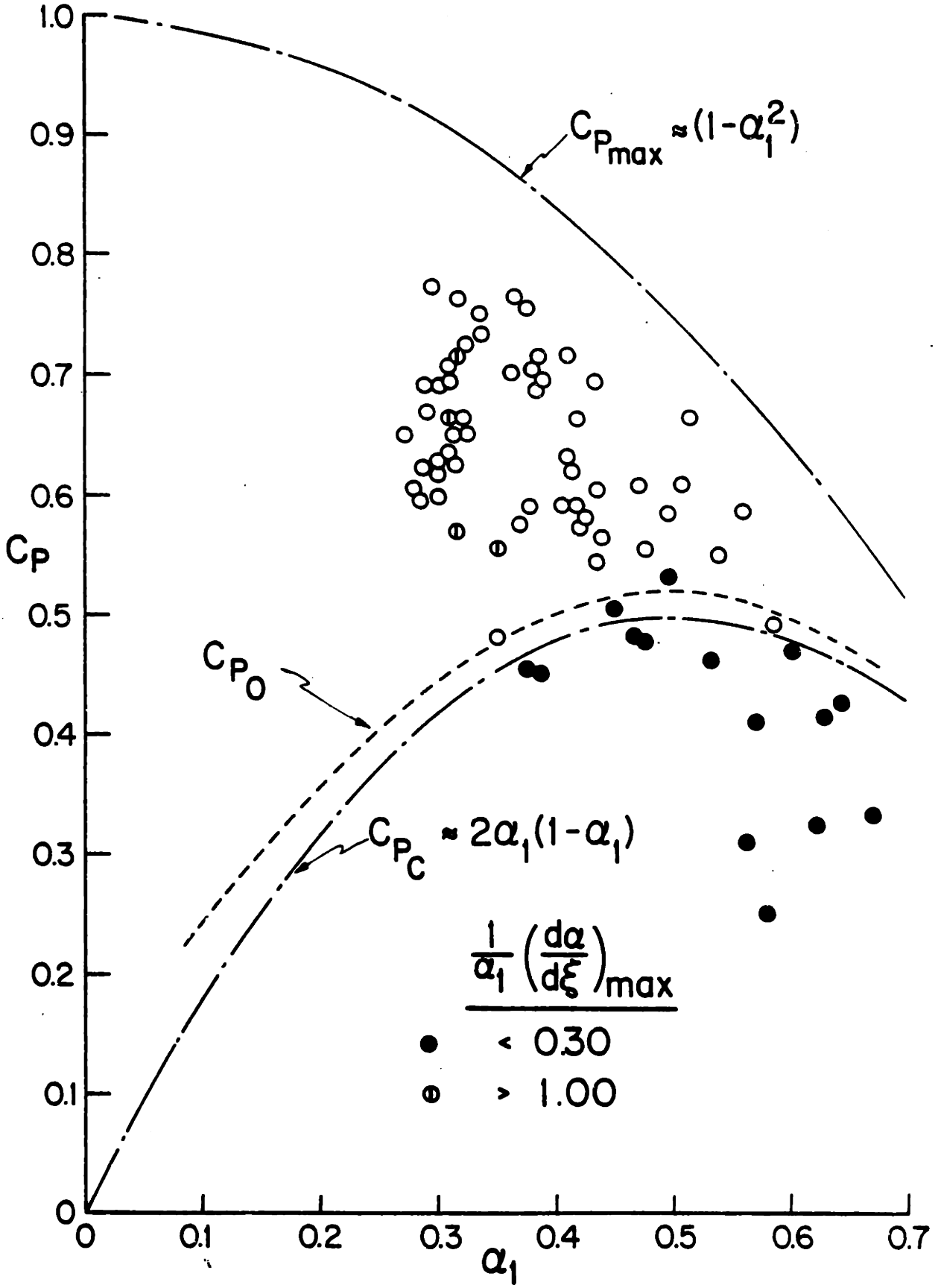
1.0
0.9
0.8
0.7
0.6
0.5
0.4
0.3
0.2
0.1
0
C_P
$C_{P_{max}} \approx (1-\alpha_1^2)$
C_{P_0}
$C_{P_c} \approx 2\alpha_1(1-\alpha_1)$
$\frac{1}{\alpha_1}\left(\frac{d\alpha}{d\xi}\right)_{max}$
● < 0.30
⊙ > 1.00
0
0.1
0.2
0.3
0.4
0.5
0.6
0.7
α_1

Figure 17

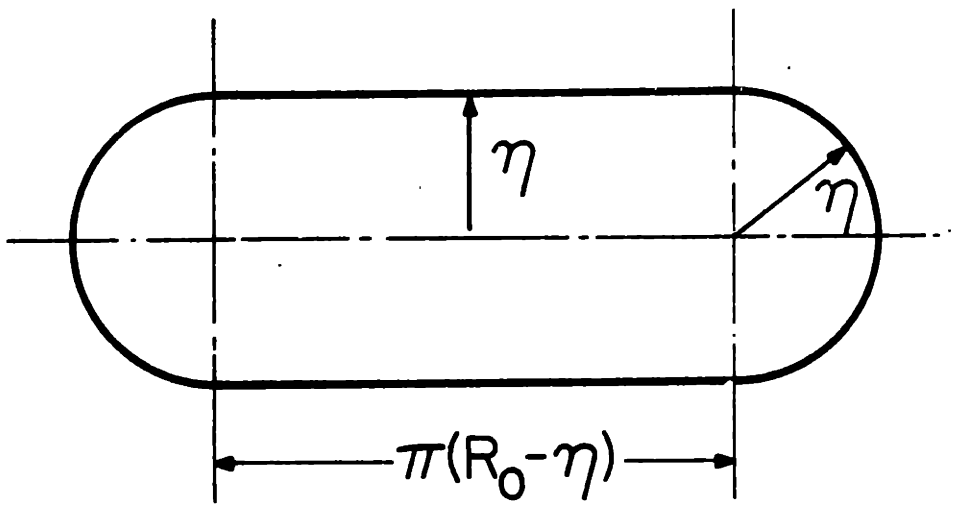

Figure 18

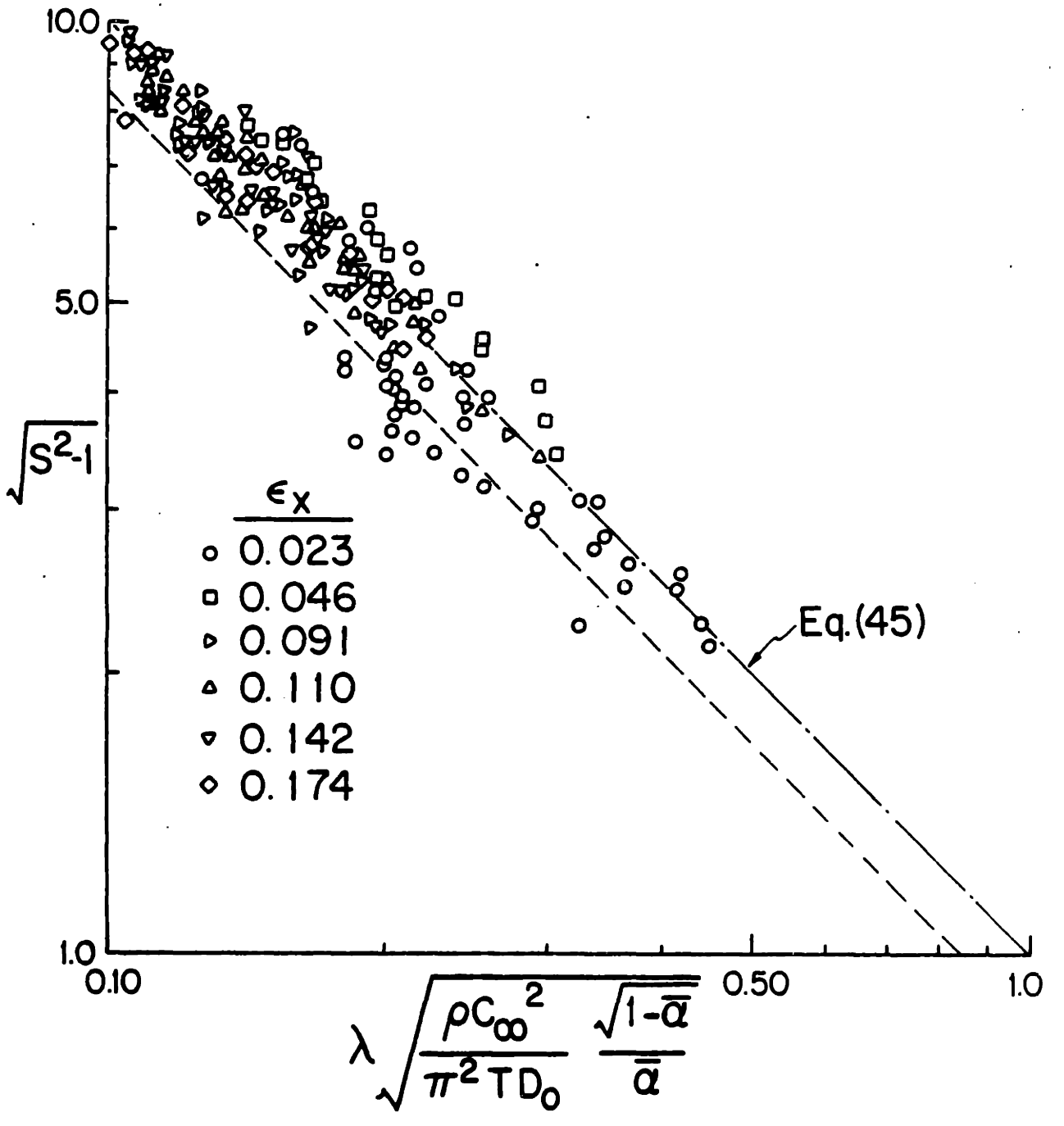
10.0
5.0
1.0
0.10
0.50
1.0
$\sqrt{S^2-1}$
ϵ_x
0.023
0.046
0.091
0.110
0.142
0.174
Eq.(45)
$\lambda\sqrt{\frac{\rho C_\infty^2}{\pi^2 T D_0}\,\frac{\sqrt{1-\bar{\alpha}}}{\bar{\alpha}}}$

Figure 19

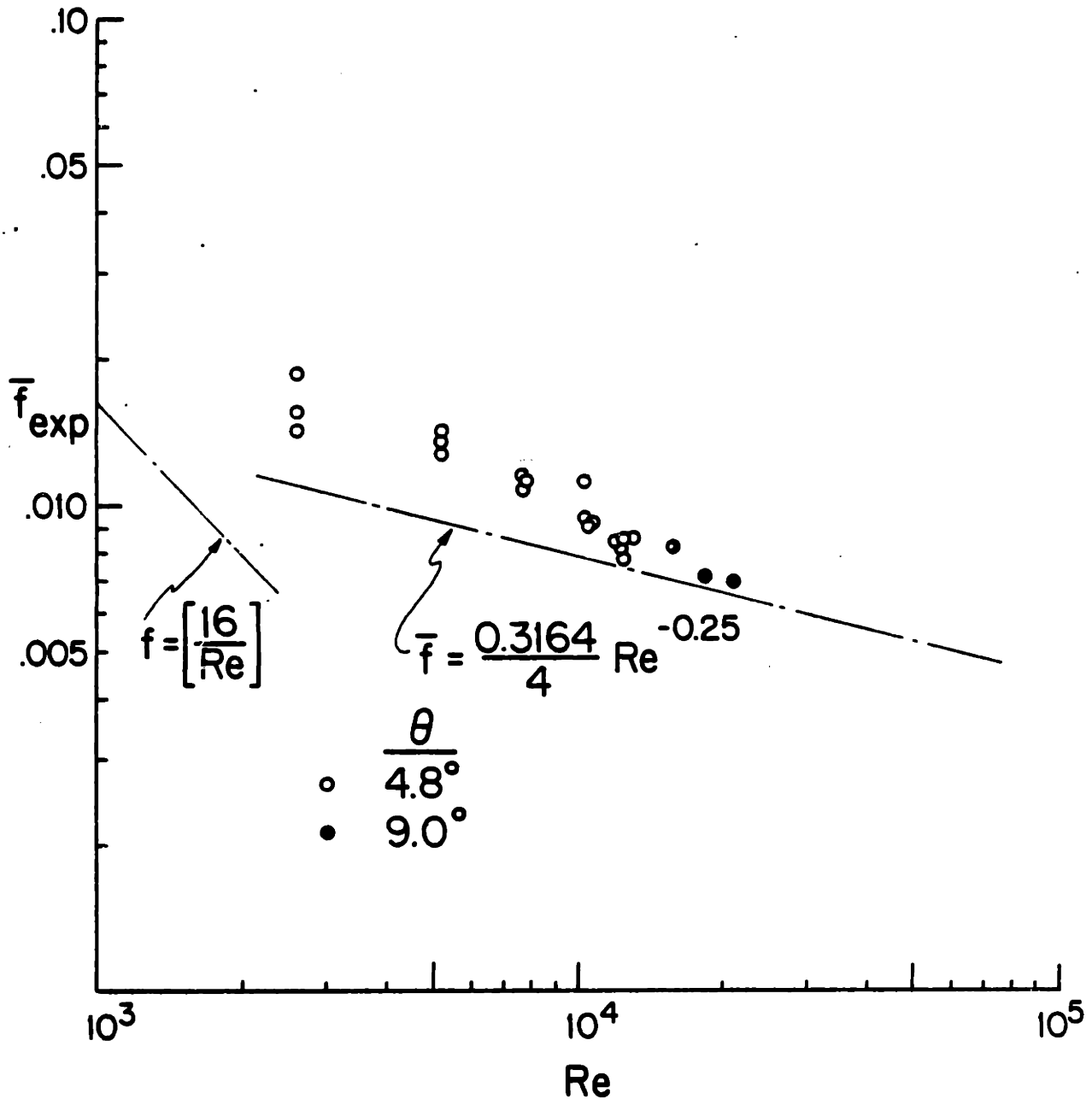
.10
.05
.010
.005
$\bar{f}_{exp}$
$f = \left[\frac{16}{Re}\right]$
$\bar{f} = \frac{0.3164}{4} Re^{-0.25}$
θ
4.8°
9.0°
10^3
10^4
10^5
Re

Figure 20

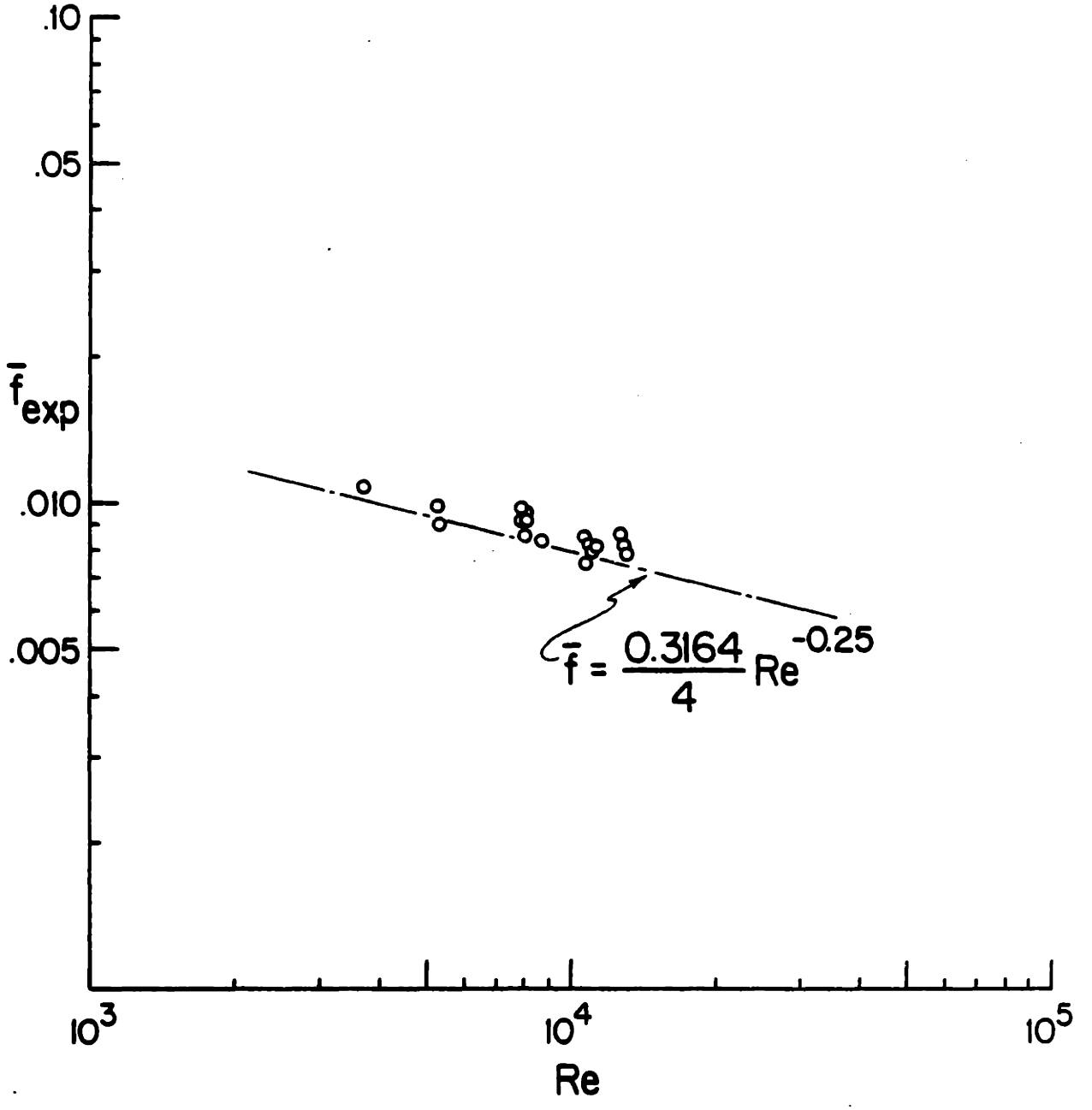

Figure 21

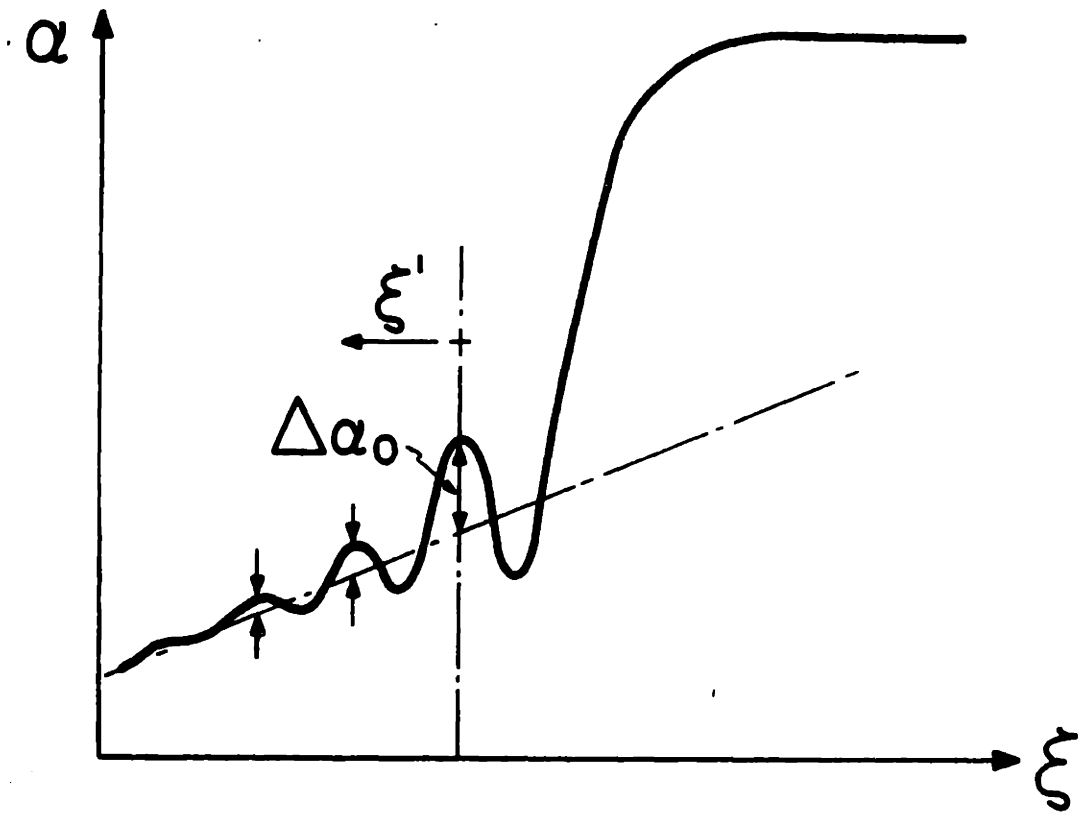

Figure 22a

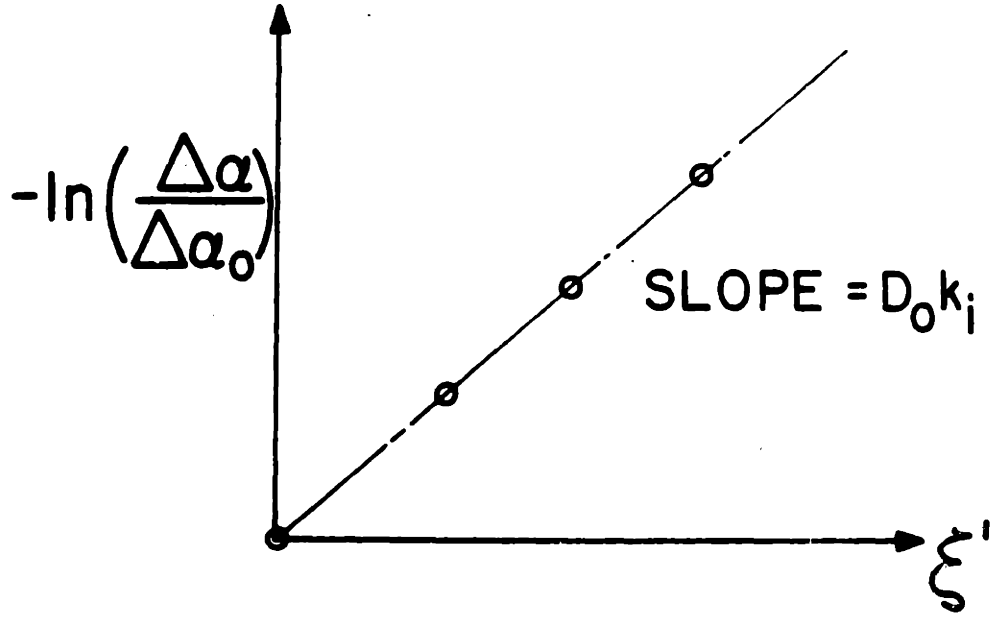

Figure 22b

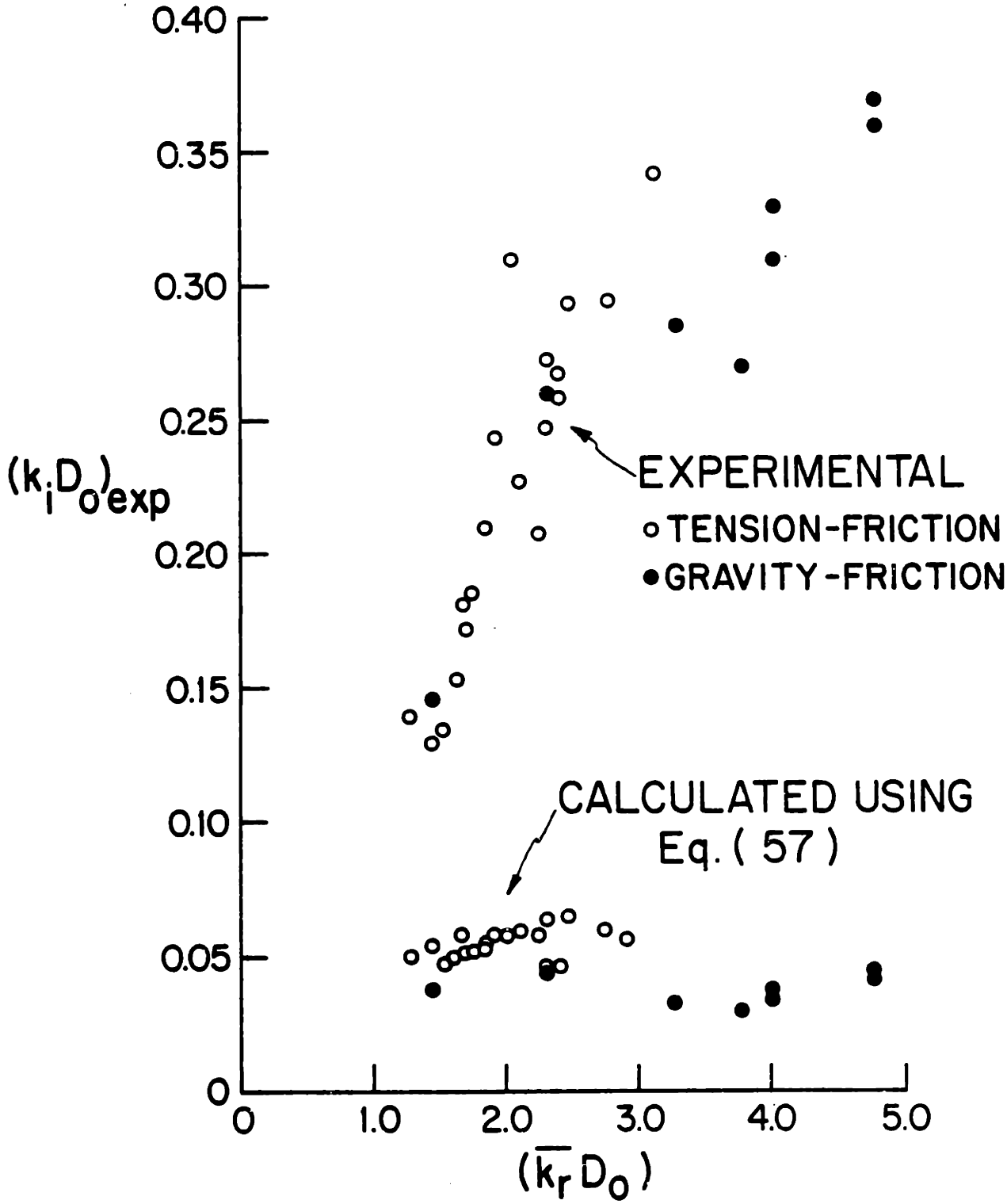
0.40
0.35
0.30
0.25
0.20
0.15
0.10
0.05
0
$(k_i D_o)_{exp}$
EXPERIMENTAL
TENSION-FRICTION
GRAVITY-FRICTION
CALCULATED USING
Eq. (57)
0
1.0
2.0
3.0
4.0
5.0
$(\overline{k_r} D_o)$

Figure 23

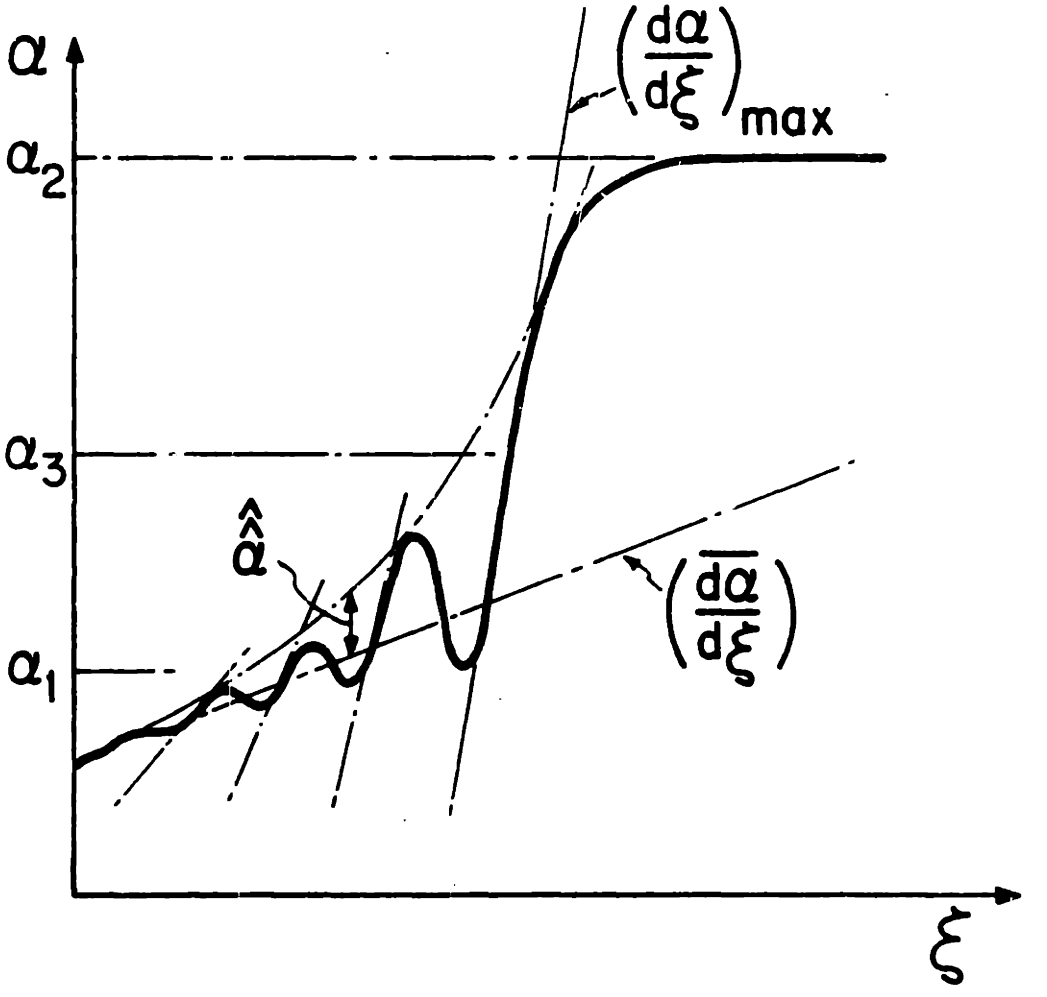

Figure 24

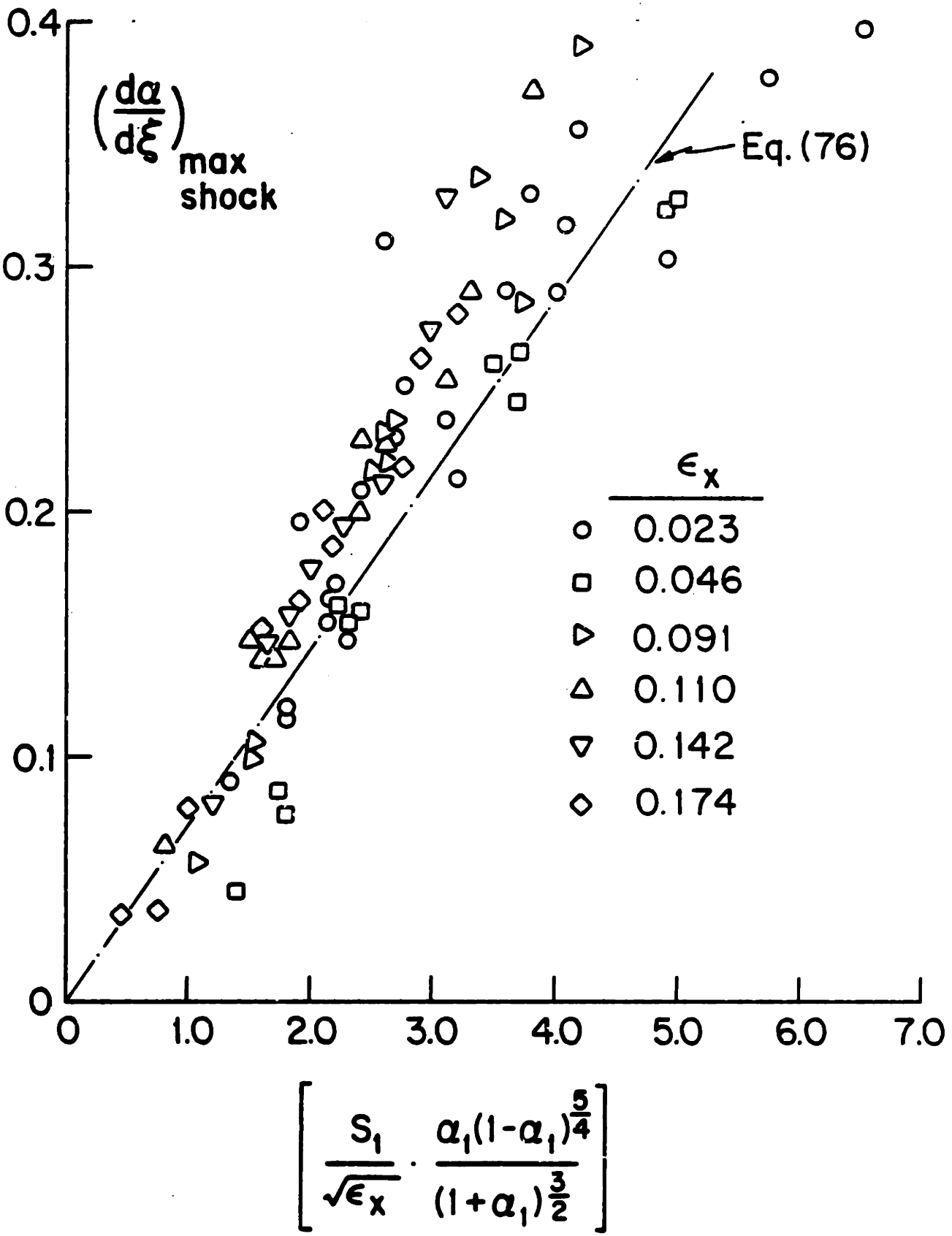
0.4
0.3
0.2
0.1
0
$\left(\frac{d\alpha}{d\xi}\right)_{max\ shock}$
Eq. (76)
ϵ_x
0.023
0.046
0.091
0.110
0.142
0.174
0
1.0
2.0
3.0
4.0
5.0
6.0
7.0
$\left[\frac{S_1}{\sqrt{\epsilon_x}} \cdot \frac{\alpha_1(1-\alpha_1)^{\frac{5}{4}}}{(1+\alpha_1)^{\frac{3}{2}}}\right]$

Figure 25

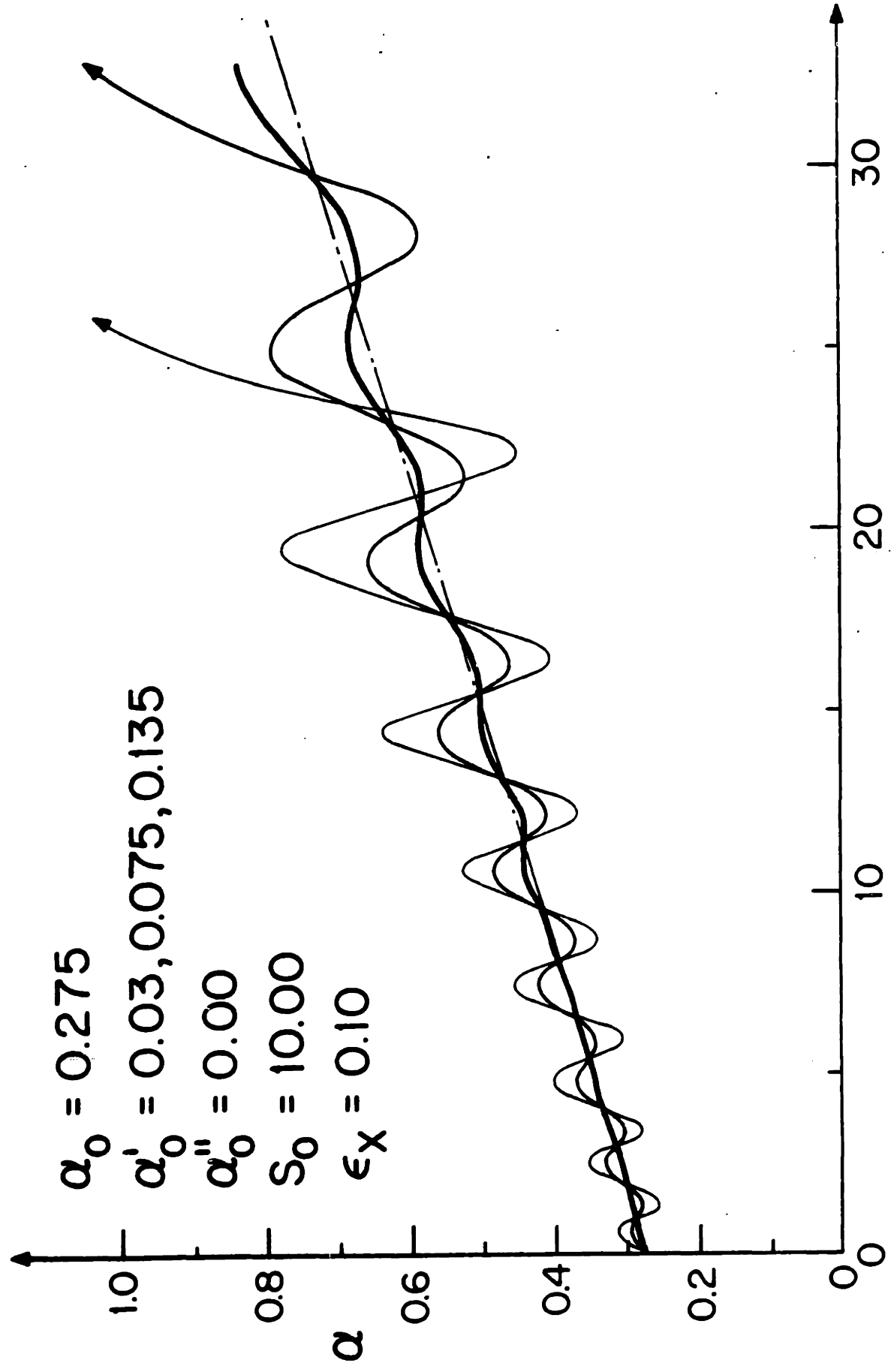
$\alpha_0 = 0.275$
$\alpha_0' = 0.03, 0.075, 0.135$
$\alpha_0'' = 0.00$
$S_0 = 10.00$
$\epsilon_X = 0.10$
α
1.0
0.8
0.6
0.4
0.2
0
10
20
30
ξ

Figure 26

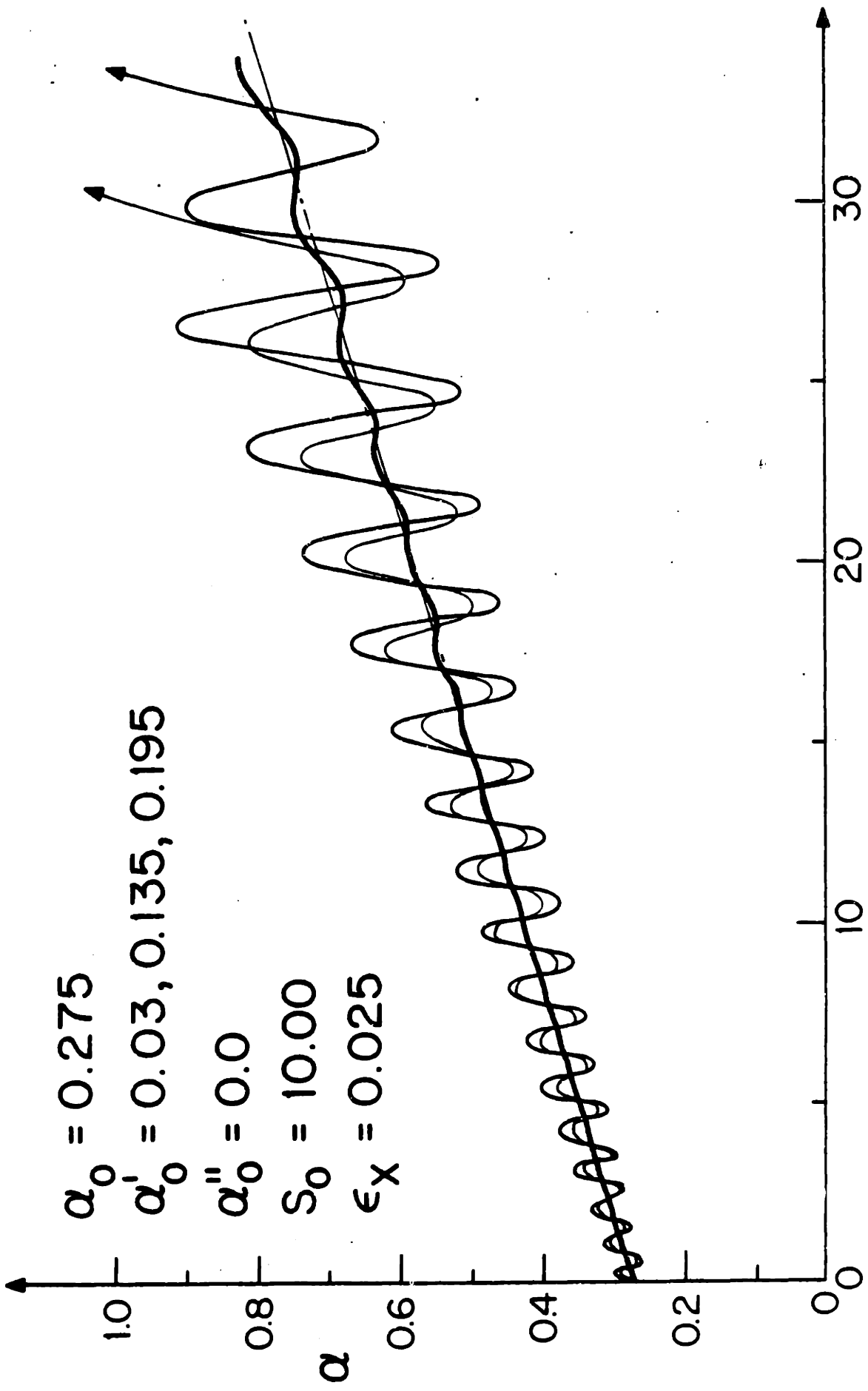
α_0 = 0.275
α_0' = 0.03, 0.135, 0.195
α_0'' = 0.0
S_0 = 10.00
ϵx = 0.025
α
ξ
0.0
0.2
0.4
0.6
0.8
1.0
10
20
30

Figure 27

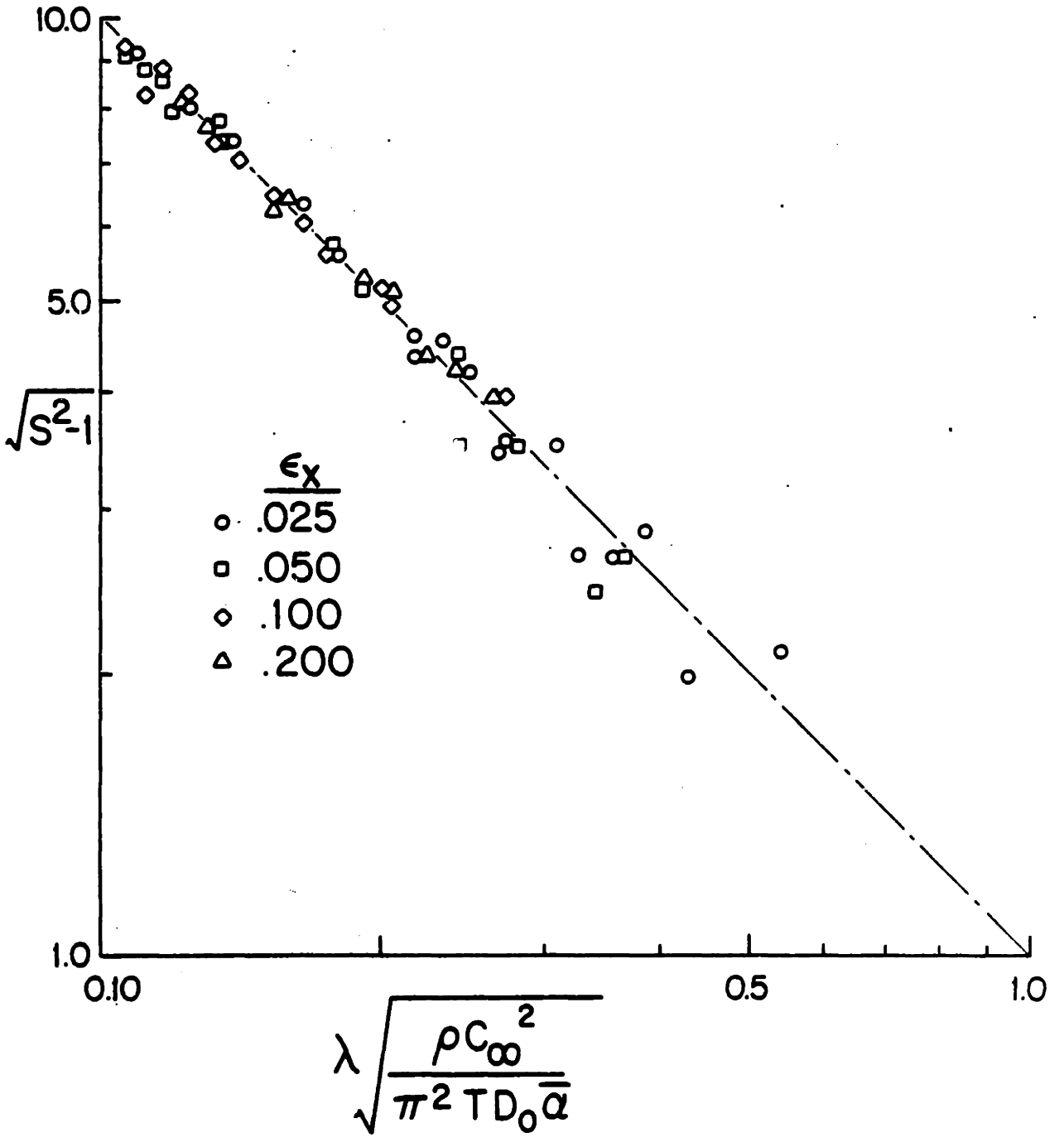
10.0
5.0
1.0
0.10
0.5
1.0
$\sqrt{S^2-1}$
ϵ_x
.025
.050
.100
.200
$\lambda\sqrt{\frac{\rho C_\infty^2}{\pi^2 T D_0 \bar{\alpha}}}$

Figure 28

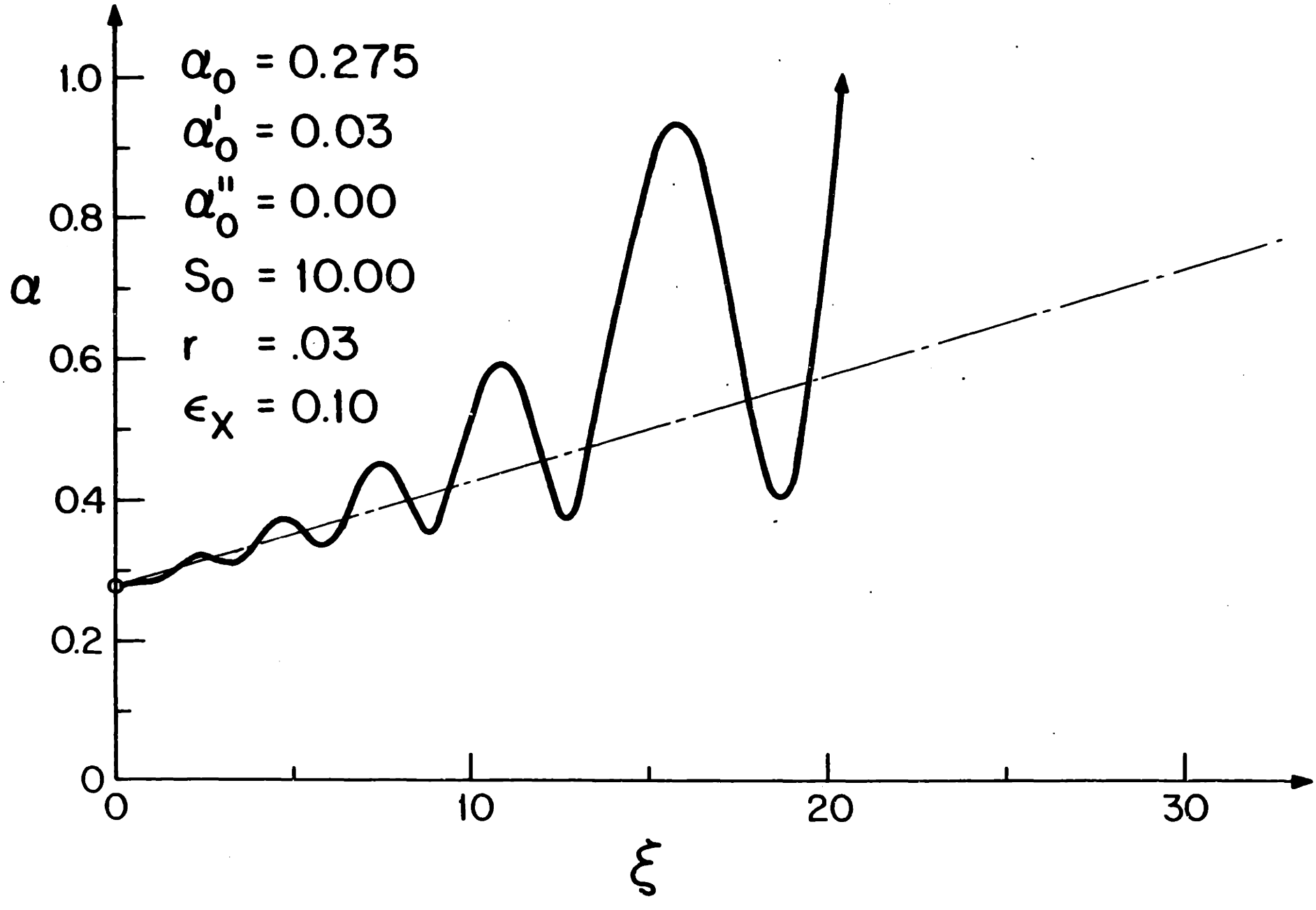
$\alpha_0 = 0.275$
$\alpha_0' = 0.03$
$\alpha_0'' = 0.00$
$S_0 = 10.00$
$r = .03$
$\epsilon_X = 0.10$
1.0
0.8
0.6
0.4
0.2
0
α
0
10
20
30
ξ

Figure 29

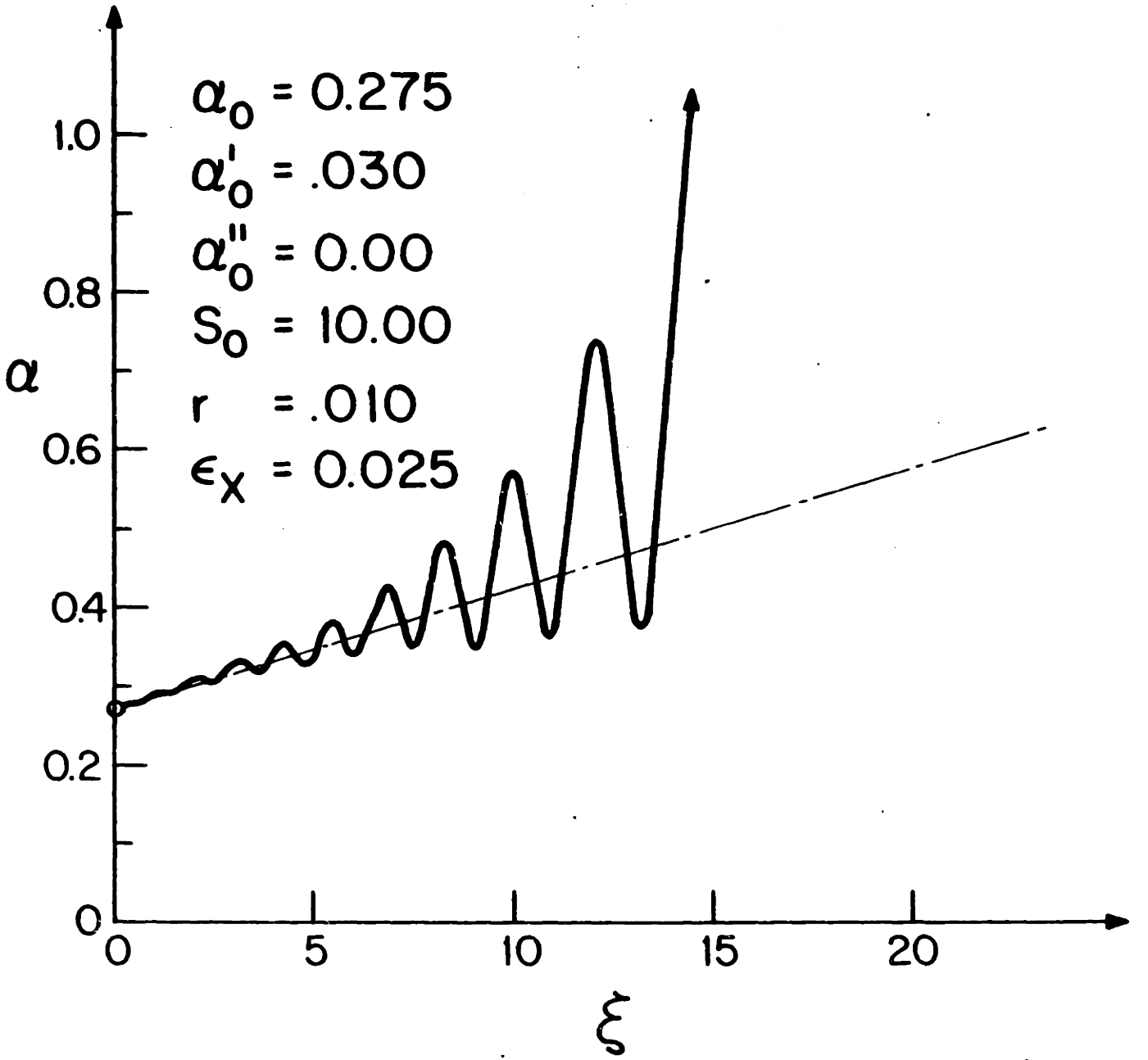
$\alpha_0 = 0.275$
$\alpha_0' = .030$
$\alpha_0'' = 0.00$
$S_0 = 10.00$
$r = .010$
$\epsilon_X = 0.025$
α
1.0
0.8
0.6
0.4
0.2
0
0
5
10
15
20
ξ

Figure 30

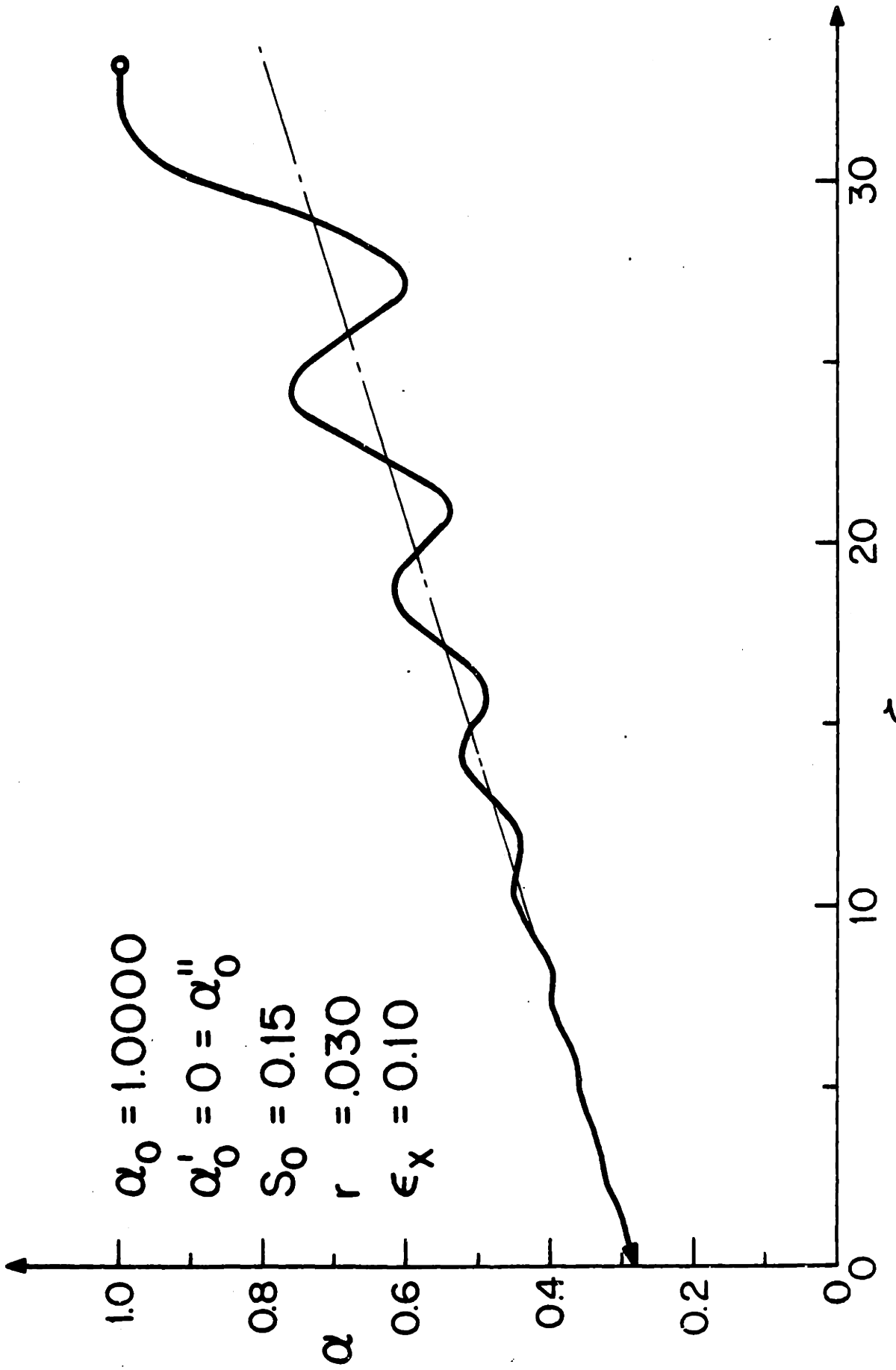
$\alpha_0 = 1.0000$
$\alpha_0' = 0 = \alpha_0''$
$S_0 = 0.15$
$r = .030$
$\epsilon_x = 0.10$
α
1.0
0.8
0.6
0.4
0.2
0
0
10
20
30
ξ

Figure 31

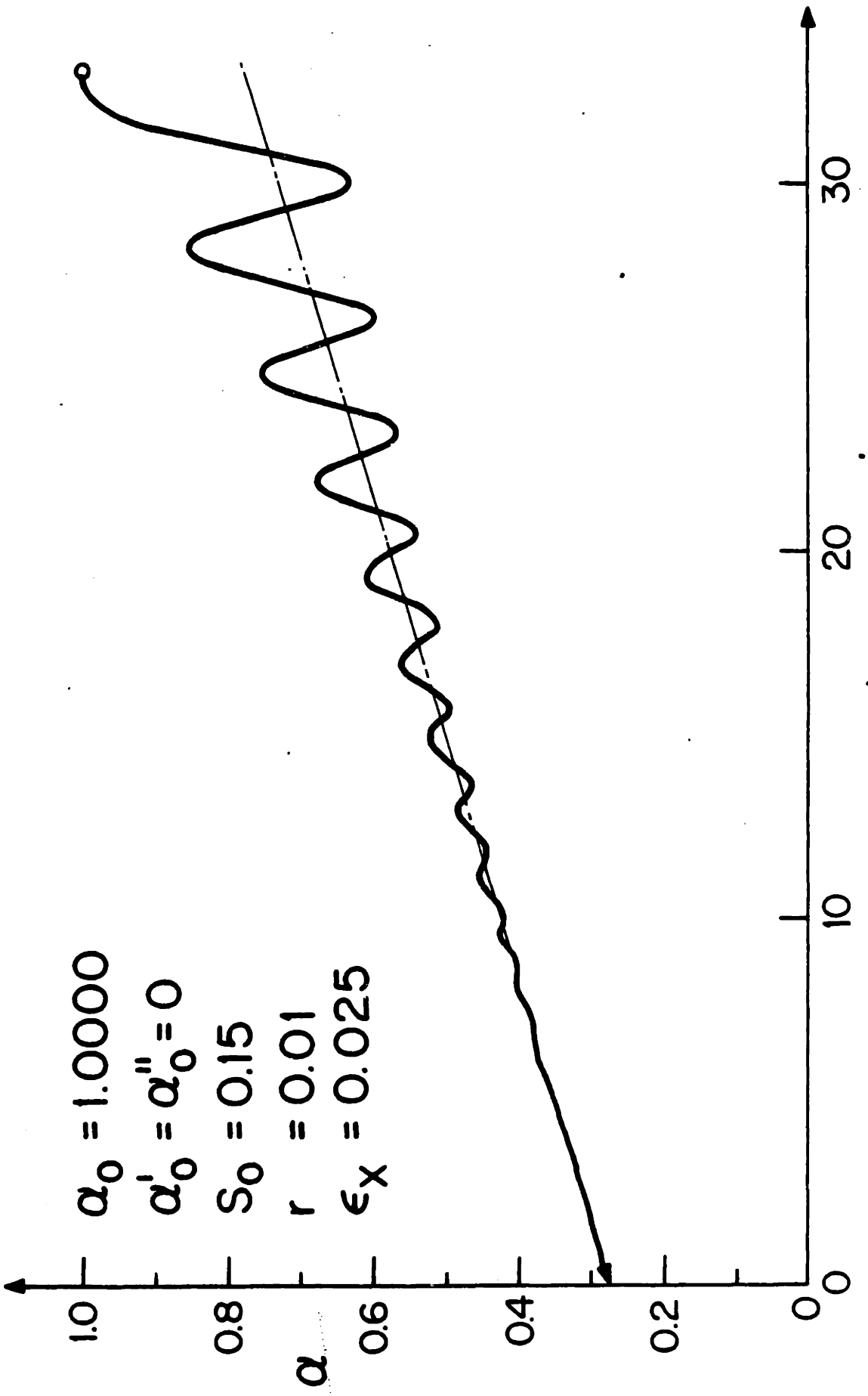
$\alpha_0 = 1.0000$
$\alpha_0' = \alpha_0'' = 0$
$S_0 = 0.15$
$r = 0.01$
$\epsilon_x = 0.025$
1.0
0.8
0.6
0.4
0.2
α
0
10
20
30
ξ

Figure 32

APPENDIX A

FORTRAN COMPUTER PROGRAM

```
//CLURKEN4 JOB CLURKEN,TIME=2                                          437
//  EXEC FIGICLG
//FORT.SYSIN DD *
C-----------------------------------------------------------------------
C-----------------------------------------------------------------------
      DIMENSION ALT(195),PRT(195),CWT(195)
  900 FORMAT(1H1)
  905 FORMAT(1H ,'_____
     1_____')
  910 FORMAT(1H ,3X,'STEADY FLOW IN COLLAPSIBLE TUBES: TENSION DOMINATED
     1')
  915 FORMAT(1H ,3X,'AC',5X,'DC',6X,'HC',4X,'XKPC',3X,'BPC',4X,'XST',2X,
     1'ALS',4X,'ETA')
  920 FORMAT(1H ,2F7.4,F8.4,2F7.1,F6.1,F5.2,F7.3)
  925 FORMAT(1H ,2X,'ALO',6X,'SIO',7X,'BO',10X,'CO',10X,'TO')
  930 FORMAT(1H ,F7.4,F9.4,3E12.4)
  935 FORMAT(1H ,5X,'UC',8X,'TS',10X,'RE',11X,'BOM',7X,'STR')
  940 FORMAT(1H ,E11.5,F9.5,E13.5,E15.7,F6.3)
  945 FORMAT(1H ,4X,'X',7X,'AL',6X,'SI',8X,'B',11X,'C',11X,'D',11X,'P')
  950 FORMAT(1H+,3X,'___',5X,'____',4X,'____',6X,'___',9X,'___',9X,'___'
     1,9X,'___')
  955 FORMAT(1H ,F8.3,2F8.4,4E12.4)
  960 FORMAT(1H )
  970 FORMAT(2F7.4,F6.4,2F6.1)
  975 FORMAT(F7.4,F8.3,F7.2)
  980 FORMAT(I2)
  985 FORMAT(F7.4,F8.4,3E13.6,F6.1,3F6.3)
      REAL K1,K2,K3,K4,M1,M2,M3,M4
C-----------------------------------------------------------------------
      READ(5,970) AC,DC,HC,XKPC,BPC
      READ(5,975)(ALT(I),PRT(I),CWT(I),I=1,195)
      READ(5,980) NC
      DO 450 MN=1,NC
      READ(5,985) AL,SI,B,C,T,XST,ALS,ETA,STR
C-----------------------------------------------------------------------
C-----------------------------------------------------------------------
      RHO=1.050
      XMEW=.012
      GR=980.0
      PI=3.141593
      MP=0
      MPS=4
      ZETAS=0.0
      EXFR=0.0
      EXVTEN=0.0
      XKPT=304.0
      X=0.0
      CALL XFUNCT(X,DOS,DDOS,DHOS,DPE,DZ,HOS,PE,Z)
      CALL TUBINT(AL,BPC,DOS,HOS,RHO,XKPC,XKPT,PR,CW,ALT,PRT,CWT)
      UC=SI*AL*CW*DOS*DOS
      CALL FRICT(AL,DC,DOS,PI,RHO,UC,XMEW,CF,PEW,RE)
      CF=CF+0.01*C
      CALL DCOEFF(AL,D1,DD1,D2,DD2)
      SI=UC/(AL*CW*DOS**2)
      DPT=-(D1*C+D2*B*B)*T/(16.*AC)
      TS=T/(16.*AC*RHO*UC*UC)
      BOM=(2.*CF*SI**2)/(SI**2-1.)
      P=PE+DPT+(PR*XKPC*HOS**3)/(DOS**3)
C-----------------------------------------------------------------------
```

```
      WRITE(6,900)
      WRITE(6,905)
      WRITE(6,910)
      WRITE(6,905)
      WRITE(6,915)
      WRITE(6,920) AC,DC,HC,XKPC,HPC,XST,ALS,ETA
      WRITE(6,905)
      WRITE(6,925)
      WRITE(6,930) AL,SI,B,C,T
      WRITE(6,905)
      WRITE(6,935)
      WRITE(6,940) UC,TS,PE,BOM,STR
      WRITE(6,905)
C-----------------------------------------------------------------------
C-----------------------------------------------------------------------
      DO 20 I=1,3000
      K=1
C-----------------------------------------------------------------------
   30 CONTINUE
      CALL XFUNCT(X,DOS,DDOS,DHOS,DPE,DZ,HOS,PE,Z)
      CALL FRICT(AL,DC,DOS,PI,RHO,UC,XME,CF,PEM,RE)
      CF=CF+0.01*C
      CALL TUBINT(AL,BPC,DOS,HOS,RHO,XKPC,XSPT,PR,CW,ALT,PRT,CWT)
      CALL DCOEFF(AL,D1,DD1,D2,DD2)
      SI=UC/(AL*CW*DOS**2)
      FR=UC/(1.0*SQRT(DC*GR*(DOS*AL)**3*DOS**2))
      VPE=16.*AC*DPE/(T*D1)
      VZ=16.*AC*RHO*GR*DZ/(T*D1)
      VKP=(48.*AC*PR*XKPC*HOS**3)*(DHOS/HOS-DDOS/DOS)/(T*D1*DOS**3)
      VDOS=-32.*AC*RHO*UC*UC*DDOS/(T*D1*AL*AL*DOS**5)
      VTEN=RHO*UC*UC*16.*AC*CF*(D1*C+D2*B*B)/(4.*T*D1*AL*AL*DOS**3)
      VDD=-((DD1+2.*D2)*B*C+DD2*B**3)/(D1)
      VWAVE=16.*RHO*UC*UC*AC*((1./SI**2*EXP(-1./FR**2-1.)*B+2.*CF/DOS+ZETAS
     1*B*B/(2.*AL))/(T*D1*DOS*(AL*DOS)**3)
      DPT=-(D1*C+D2*B*B)*T/(16.*AC)
      P=PE+DPT+(PR*XKP/HOS**3)/(DOS**3)
C-----------------------------------------------------------------------
      IF(ETA.LT.0.) GO TO 600
      IF(X.LT..001) GO TO 21
      GO TO 25
  600 IF(X.GT.-.001) GO TO 21
      GO TO 25
   21 D=VPE+VZ+VKP+VDOS+VTEN+EAVTEN+VDD+VWAVE
      WRITE(6,960)
      WRITE(6,945)
      WRITE(6,950)
      WRITE(6,955) X,AL,SI,B,C,D,P
   25 CONTINUE
C-----------------------------------------------------------------------
C-----------------------------------------------------------------------
      GO TO (40,50,60,70),K
   40 K1=B
      M1=C
      R1=VPE+VZ+VKP+VDOS+VTEN+EAVTEN+VDD+VWAVE
      X=X+.5*ETA
      AL=AL+.5*ETA*K1
      B=B+.5*ETA*M1
      C=C+.5*ETA*R1
      K=2
      GO TO 30
C-----------------------------------------------------------------------
```

```
   50 K2=B
      M2=C
      R2=VPE+VZ+VKP+VDDS+VTEN*EXVTEN+VDD+VWAVE
      AL=AL+.5*ETA*(K2-K1)
      B=B+.5*ETA*(M2-M1)
      C=C+.5*ETA*(R2-R1)
      K=3
      GO TO 30
C-----------------------------------------------------------------------
   60 K3=B
      M3=C
      R3=VPE+VZ+VKP+VDDS+VTEN*EXVTEN+VDD+VWAVE
      X=X+.5*ETA
      AL=AL+.5*ETA*(K3-K2)+.5*ETA*K3
      B=B+.5*ETA*(M3-M2)+.5*ETA*M3
      C=C+.5*ETA*(R3-R2)+.5*ETA*R3
      K=4
      GO TO 30
C-----------------------------------------------------------------------
   70 K4=B
      M4=C
      R4=VPE+VZ+VKP+VDDS+VTEN*EXVTEN+VDD+VWAVE
      AL=AL-K3*ETA
      B=B-M3*ETA
      C=C-R3*ETA
C-----------------------------------------------------------------------
      AL=AL+(K1+2.*K2+2.*K3+K4)*(ETA/6.0)
      B=B+(M1+2.*M2+2.*M3+M4)*(ETA/6.0)
      C=C+(R1+2.*R2+2.*R3+R4)*(ETA/6.0)
C-----------------------------------------------------------------------
      CALL XFUNCT(X,DDS,DDDS,DHDS,DPE,DZ,HDS,PE,Z)
      CALL FRICT(AL,DC,DDS,PI,RHO,UC,XMEW,CF,PER,RE)
      CF=CF+0.01*C
      CALL TURBINT(AL,BPC,DDS,HDS,RHO,XKPC,AKPT,PR,CW,ALT,PRT,CWT)
      CALL DCOEFF(AL,D1,DD1,D2,DD2)
      SI=UC/(AL*CW*DDS**2)
      FR=UC/(1.0*SQRT(DC*GR*(DDS*AL)**3*DDS**2))
      T=T-EXVTEN*(RHO*UC*UC*CF*PI*DC*DC*ETA)/(2.*AL*AL*DDS**3)
      DPT=-(D1*C+D2*C*C)*T/(16.*AC)
      P=PE+DPT+(PR*XKPC*HDS**3)/(DDS**3)
      VPE=16.*AC*DPE/(T*D1)
      VZ=16.*AC*RHO*GR*DZ/(T*D1)
      VKP=(48.*AC*PR*XKPC*HDS**3)*(DHDS/HDS-DDDS/DDS)/(T*D1*DDS**3)
      VDDS=-32.*AC*RHO*UC*UC*DDDS/(T*D1*AL*AL*DDS**5)
      VTEN=RHO*UC*UC*16.*AC*CF*(D1*C+D2*3*C)/(3.*T*D1*AL*AL*DDS**3)
      VDD=-((DD1+2.*D2)*B*C+DD2*C**3)/(D1)
      VWAVE=16.*RHO*UC*UC*AC*((1./SI**2*EXP(-R/FR**2-1.)*H+2.*CF/DDS+ZETAS
     1*B*B/(2.*AL))/(T*D1*DDS*(AL*DDS)**3)
      D=VPE+VZ+VKP+VDDS+VTEN*EXVTEN+VDD+VWAVE
C-----------------------------------------------------------------------
      MP=MP+1
      IF(MP.EQ.MPS) GO TO 18
      GO TO 19
   18 WRITE(6,955) X,AL,SI,B,C,D,P
      MP=0
   19 IF(ETA.LT.0.) GO TO 400
      IF(AL.GT.ALS) GO TO 450
      IF(X.GT.XST) GO TO 450
      GO TO 20
  400 IF(AL.LT.ALS) GO TO 450
```

```
      IF(X.LT.XST) GO TO 450
   20 CONTINUE
  450 CONTINUE
      WRITE(6,900)
  500 STOP
      END
C-----------------------------------------------------------------------
      SUBROUTINE TURINT(AL,APC,DOS,HOS,RHO,XKPC,XKPT,PR,CW,ALT,PRT,CWT)
      DIMENSION ALT(195),PRT(195),CWT(195)
      IF(AL.GT..2000) GO TO 1
      PR=-1./AL**1.5
      CW=1.0*SQRT((1.5*XKPC*HOS**3)/(DOS**3*RHO*AL**1.5))
      GO TO 5
    1 IF(AL.GE.1.012) GO TO 4
      DO 2 M=1,195
      IF(AL.LE.ALT(M)) GO TO 3
    2 CONTINUE
    3 J=M-1
      CW=CWT(J)+(CWT(J+1)-CWT(J))*(AL-ALT(J))/(ALT(J+1)-ALT(J))
      CW=CW*1.0*SQRT((XKPC*HOS**3)/(XKPT*DOS**3*RHO))
      PR=PRT(J)+(PRT(J+1)-PRT(J))*(AL-ALT(J))/(ALT(J+1)-ALT(J))
      GO TO 5
    4 CW=1.0*SQRT((APC*XKPC*HOS**2.)/(DOS*RHO))/AL
      PR=((APC*DOS**2)/(HOS**2))*(1.-1./AL**2)-5.0
    5 CONTINUE
      RETURN
      END
      SUBROUTINE FRICT(AL,DC,DOS,PI,RHO,UC,XMEW,CF,PER,RE)
      IF(AL.LT.1.0) PER=PI*DC*DOS
      IF(AL.GE.1.0) PER=PI*DC*DOS*1.0*SQRT(AL)
      RE=(RHO*UC*DC)/(XMEW*DOS)
      IF(RE.GT.2200.) GO TO 2
      IF(AL.LT..360) GO TO 1
      CF=16.0/RE
      GO TO 3
    1 CF=(140.*XMEW*AL*DOS*DOS)/(PER*RHO*UC)
      GO TO 3
    2 CF=.0791/(RE**.25)
    3 CONTINUE
      RETURN
      END
      SUBROUTINE DCOEFF(AL,D1,DD1,D2,DD2)
      D1=1.0
      DD1=0.0
      IF(AL.LT..50) GO TO 1
      IF(AL.GE..50.AND.AL.LT..90) GO TO 2
      IF(AL.GE..90.AND.AL.LT.1.0) GO TO 3
      IF(AL.GE.1.0.AND.AL.LT.1.012) GO TO 4
      IF(AL.GE.1.012) GO TO 5
    1 D2=0.0
      DD2=0.0
      GO TO 7
    2 D2=1./(1.0-AL)-2.5
      DD2=1./(1.0-AL)**2
      GO TO 7
    3 D2=7.5
      DD2=0.0
      GO TO 7
    4 D2=-666.67*AL+674.167
```

```
      DDZ=-666.67
      GO TO 7
    5 DZ=-.50
      DDZ=0.0
    7 CONTINUE
      DZ=0.0
      DDZ=0.0
      RETURN
      END
      SUBROUTINE XFUNCT(X,DOS,DDOS,DHOS,DPE,DZ,HOS,PE,Z)
      DOS=1.0
      DDOS=0.0
      HOS=1.0
      DHOS=0.0
      Z=0.0
      DZ=0.0
      DZ=-.9209694
      PE=0.0
      DPE=0.0
      RETURN
      END
/*
//GO.SYSIN DD *
```